https://lib.uliege.be https://matheo.uliege.be

Master thesis and internship[BR]- Master's thesis : Computational method for whirl-flutter instability analysis for flexible propellers[BR]- Integration internship

Auteur : Denoël, Camille
Promoteur(s) : Salles, Loïc
Faculté : Faculté des Sciences appliquées
Diplôme : Master en ingénieur civil en aérospatiale, à finalité spécialisée en "aerospace engineering"
Année académique : 2024-2025
URI/URL : http://hdl.handle.net/2268.2/23267

Avertissement à l'attention des usagers :

Tous les documents placés en accès ouvert sur le site le site MatheO sont protégés par le droit d'auteur. Conformément aux principes énoncés par la "Budapest Open Access Initiative"(BOAI, 2002), l'utilisateur du site peut lire, télécharger, copier, transmettre, imprimer, chercher ou faire un lien vers le texte intégral de ces documents, les disséquer pour les indexer, s'en servir de données pour un logiciel, ou s'en servir à toute autre fin légale (ou prévue par la réglementation relative au droit d'auteur). Toute utilisation du document à des fins commerciales est strictement interdite.

Par ailleurs, l'utilisateur s'engage à respecter les droits moraux de l'auteur, principalement le droit à l'intégrité de l'oeuvre et le droit de paternité et ce dans toute utilisation que l'utilisateur entreprend. Ainsi, à titre d'exemple, lorsqu'il reproduira un document par extrait ou dans son intégralité, l'utilisateur citera de manière complète les sources telles que mentionnées ci-dessus. Toute utilisation non explicitement autorisée ci-avant (telle que par exemple, la modification du document ou son résumé) nécessite l'autorisation préalable et expresse des auteurs ou de leurs ayants droit.

Computational method for whirl-flutter instability analysis for flexible propellers

Travail de fin d'études réalisé en vue de l'obtention du grade de master Ingénieur civil en aérospatiale par **Camille Denoël**

Superviseur: **Loïc Salles**

Université de Liège - Faculté des Sciences appliquées

Année académique : 2024 - 2025

Contents

List of Figures

List of Tables

Abstract

This thesis aims at developing a finite-element framework to investigate the *whirl-flutter* phenomenon for propeller mounted on flexible wings. The problem is tackled in a modern fashion by first modeling the whole structure, including the blades, as finite-element entities expressed either in the fixed frame for the stator part or in the rotating frame for the rotating parts. Equations of motion in those 2 frames were coupled together using an innovative and adapted to the context of final element coupling algorithm. Resulting equations of motion displaying an explicit, but periodic, dependence to time. Practically, the *FerBeam* python framework was developed from scratch to be able to handle arbitrarily user-inputted beam structures with stator and rotor parts and applying the coupling procedure.

Studying stability of periodic equations of motion revealed to be a challenge as such systems can't be investigated using traditional tools for linear systems. In this thesis, the Floquet analysis was used but as it requires an extensive numerical integration additional studies were made to select the best time integration procedure. They revealed a particularly stiff nature of the problem from a numerical point of view which was handled using *BDF* formulas and greatly sped up by parallelizing the problem and by expression equations of motion as tensors.

Analysis of the stability revealed multiple possible instability regions of different nature, namely *whirl flutter* or *divergence* with stability that is sometimes, but not always, retrieved in between them. It remained, in almost all test cases, that the first instability always is a *whirl flutter*, stability is retrieved over a small Ω bandwidth after which a *divergence* instability imposes the absolute critical speed Ω above which the structure cannot be operated. For high speed instabilities it was found out that taking into account blade dynamics allowed for up to 15% of the flapping motion to come from blade vibrations outside of rotation plane.

Presence of a flexible was investigated and, while providing a slightly positive outcome on the stability for sturdy wings, it can also greatly deteriorate stability if a very flexible wing is considered as it provides an extra arms lever to the system. Large exchanges of energy between the rotor and the wing were highlighted for flexible wings and higher speed instabilities proving the necessity of taking into account the presence of a wing.

Requirements on pylon stiffness were investigated by constructing the *stability diagrams* and revealed 2 unstable region one corresponding to the first whirl flutter instability and the other corresponding to the divergence instability and those occurring at larger rotation speeds Ω. They also revealed the necessity of the coupling procedure as otherwise one of the unstable region isn't predicted at all.

Acknowledgments

I'd first like to thank my supervisor, professor Loïc Salles, who gave me the opportunity to do this master thesis on my own while providing extremely useful feedback and help throughout my whole internship at the University of Liège. Computational resources have been provided by the Consortium des Équipements de Calcul Intensif (CÉCI), funded by the Fonds de la Recherche Scientifique de Belgique (F.R.S.-FNRS) under Grant No. 2.5020.11 and by the Walloon Region.

I'd also like to thank my office colleagues, namely Mathis, Axelle, Émile, Victor, Ghislain and Joey who made every day in the office much more interesting and fun.

I also want to thank all of the friends and wonderful people I met during my academic journey. I'm especially thinking about Jarod, Alejandro, Thomas, Sonny, Éthan, Emma, Louise, Luca and my lovely girlfriend Lena. I'm so glad I've had the chance to cross your path. Your unending support and inexhaustible amount of interesting discussions make all of this possible.

I would also like to thank my family that I love with all of my heart.

Finally, I'd like to thank all of my sisters, bound together by the share of a common fate, that gave me the strength to live a life I had previously only ever dreamed of.

Chapter 1

Introduction

1.1 Context

Whirl flutter is the association of the terms *whirl* depicting a rotation and *flutter* depicting an instability in aero-elasticity jargon; In other words whirl flutter depicts an aero-elastic instability due to gyroscopic effects of a propeller.

Physically, the propeller is mounted on a wing structure such that the precession motion of the rotor influences the overall structure dynamic thereby influencing its vibration modes such that it could yield to one of them becoming unstable. From this results *flutter* or more specifically *whirl flutter* making the overall system unstable as the contribution of the unstable vibrations modes to the structure response are ever growing with time.

In 1938, Taylor and Browne[33] analytically discovered the whirl flutter phenomena and proposed a stability criteria. The phenomena however was found to be of no significance for airplanes of that time.

In 1959 & 1960, 2 *Lockheed L-188 C Electra II* (Figure 1.1a) crashes marked the first incidents that could directly be attributed to *whirl flutter*(Čečrdle (2015,[35])). These 2 incidents sparked the beginning of an extensive experimental research campaigns conducted in the NASA's Transonic Dynamic Tunnel (TDT) where a reduced model of the Lockheed L-188 was tested (Figure 1.1b). The campaign showed that the engine mounts had suffered damage that reduced their stiffness and allowed for propagation of the propeller precession motion to the wing structure until failure (H. Reed (1965,[21])). This tragic incident showed that whirl-flutter had to be taken into account at design stage.

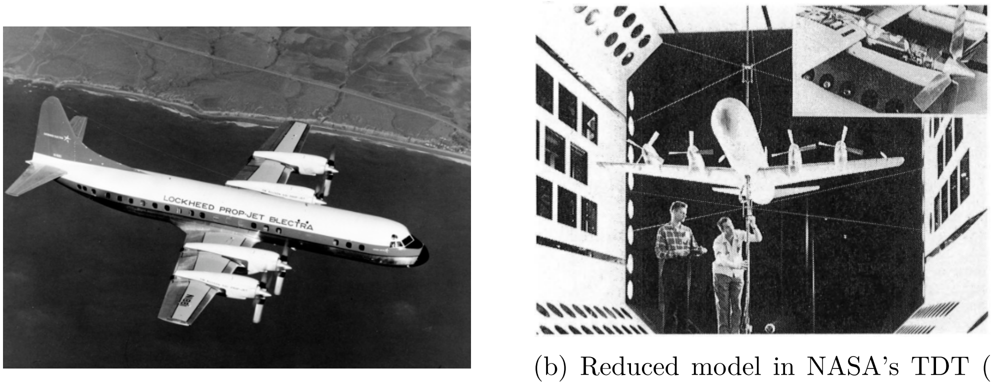

(a) Prototype flight

(b) Reduced model in NASA's TDT (From [21])

Figure 1.1: Lockheed L-188 C Electra II

As time went on more exotic configurations were investigated for whirl flutter and motivated the development of more complex analytical models that take into account blade flapping/lagging for helicopters (Richardson, Naylor (1962,[20])), blade flexibility (Richardson (1962,[10]) or wing elasticity (Bennet, Bland, (1964,[19]) all of which tend to make the model less conservative allowing to reduce the stiffness requirements on the engine mounts and on the wing.

Figure 1.2: Archer's E-VTOL Midnight tilt-rotor(2023, [2])

Recent developments, especially in the context of ultra light-weight tilt-rotor configurations with extremely light and flexible wings are more prone than ever to whirl flutter. One example of such configurations is given in Fig 1.2. These type of systems showed the necessity to go further than the analytical models and consider more complex approaches to hopefully obtain less conservative and more accurate prediction of the whirl-flutter instabilities.

Rose & Roden (1989, [24]) proposed a numerical approach using MSC/Nastran allowing to consider additionnal effects such as wing downwash or the propeller wake.

Koch & Koert(2023[10]) considered a finite-element model of the blades of a clamped propeller configuration and showed that it has a great impact on whirl flutter stability, typically being even conservative than the analytical models (Experimentally observed by Donham in 2007[14]).

Böhnisch Et al. (2022[5], 2024[3]) considered the coupling between a wing structure expressed as finite-element entity and a simple 2 degree of freedom rotor with rigid blades. It showed that even though most instabilities occured due to either a forward or backward whirl mode becoming instable there also exist configurations where a wing mode becomes unstable thereby capturing richer dynamics thanks to the addition of coupling.

1.2 Aim of this work

This thesis can be seen as a fusion and an extension between the work of Koch & Koert(2023[10]) that considered elastic blades but without any stator part and Böhnisch (2022[5], 2024[3]) that considered a coupling between the stator and rotor parts but with only 2 degrees of freedom to model the rotor part.

The goal is to develop an innovative method of whirl flutter stability analysis by considering a full finite-element model of the stator *and* the rotor part allowing the fully describe their dynamics through 2 sets of equations of motions. These equations will then be coupled together using a time-dependent but periodic change of variable following a coupling algorithm that will be described. Finally, the stability of the system shall be assessed using Floquet's theory.

1.3 Thesis outline

Chapter 1 gives an introduction and presents the state of the art of whirl-flutter analysis with different analytical models augmented by more recent developments.

Chapter 2 describes the finite element approach used in the whole thesis. It starts with how to model the problem, reminds the basis of the finite element method and then provides an implementation of it which is verified using a commercial software with the stator and the rotor part of the equations of motion.

Chapter 3 describes the motion of a rotating particle as seen from an inertial frame. These results are then generalized to a finite-element formulation and yield to the establishment of a coupling algorithm between the stator and the rotor equations of motion.

Chapter 4 describes Floquet's theory for the stability of periodic systems. Theoretical reminders on the numerical integrations of stiff systems are then given yielding to discussions on the choice of the most suitable integration schemes for the problem. Stability of the system itself is finally studied and the results are compared the ground-resonance analytical models as a verification, the addition of a flexible wing is also investigated and the stability diagrams with and without coupling are investigated.

1.4 Introduction to FerBeam

A major challenge of this thesis was to build a software capable of modeling the dynamics of user-imputed beam structures with a stator and a rotor part. At this aim, at Python framework, finite-element of rotating beams or *FerBeam* was developped from scratch. All the relevant equations will be thoroughly reviewed in Chapter 2 & 3, this subsection only aims at giving a small introductory summary of the capabilities of FerBeam.

The flow chart of the code is given in Figure 1.3. User inputs consist off the geometry of the rotor and stator beams as well as their materials, their boundary conditions ("Clamped", "Free" or "Attached" to another beam) and exterior loads. The user is free to define a structure that has no rotating part, only rotating parts or a combination of both. The hearth of the code consist of the *FE_Structure.py* file that takes user inputs, build the appropriate mesh, computes the elemental matrices using *Shape_functions.py* and finally computes the structural uncoupled matrices through assembly. One may finally create a *Coupled_Structure* object from the *Coupling.py* using the previously constructed *FE_Structure* object to apply the coupling procedure between the stator and rotor parts to obtain the coupled equations of motion. It's possible onwards to either do a time simulation of the structure response or to compute the monodromy matrix and assess the stability of the structure.

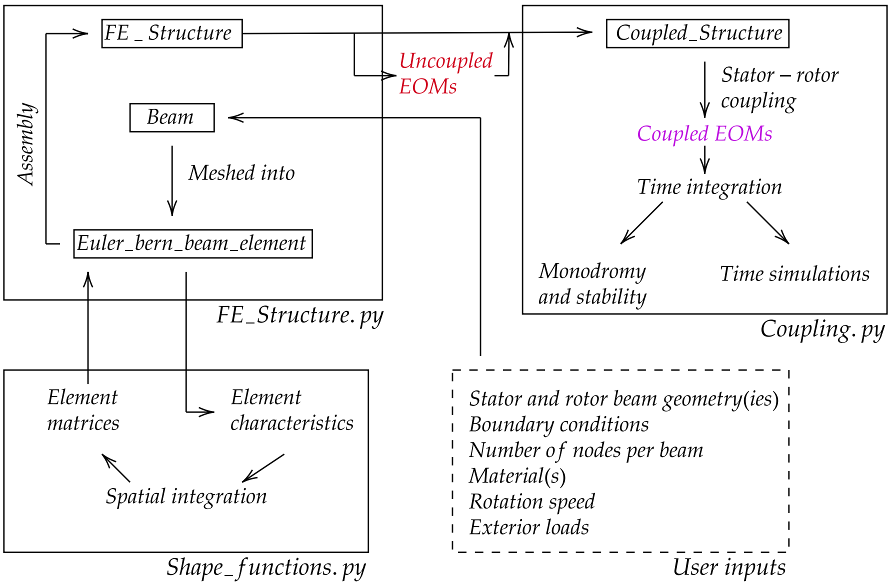

Figure 1.3: Flow chart of the Python framework. Boxed elements are either classes or python files.

A typical utilization of FerBeam could be for example to build a wing-propeller structure. If one wishes to do so here is how it can be done.

```python
from FE_structure import FE_structure,Beam
from Coupling import Coupled_structure
    #Wing-propeller structure

    #Stator part
    wing=Beam(A,E,rho,nu,b,h,start=[0,0,0],end=[3,0,0],nbr_elem=2)

    #Rotor part
    shaft=Beam(A,E,rho,nu,b,h,start=[3,0,0],end=[3,1,0],nbr_elem=2,Omega,P_pivot)
    blade1=Beam(A,E,rho,nu,b,h,start=[3,1,0],end=[3,1,2],nbr_elem=2,Omega,P_pivot)
    blade2=Beam(A,E,rho,nu,b,h,start=[3,1,0],end=[3,1,-2],nbr_elem=2,Omega,P_pivot)
    blade3=Beam(A,E,rho,nu,b,h,start=[3,1,0],end=[3,3,0],nbr_elem=2,Omega,P_pivot)
    blade4=Beam(A,E,rho,nu,b,h,start=[3,1,0],end=[3,-1,0],nbr_elem=2,Omega,P_pivot)
```

Where P_pivot is the pivot point around which the beam rotates (which is the hub in this case) and Omega the rotation matrix. Once the beams are defined the structure can be constructed following

```python
    #Creation of the FE_structure
    Structure=FE_structure()
    Structure.add_beam(wing,start_condition="Clamped",end_condition="Attached",
   attachments=[shaft])
```

```
    Structure.add_beam(shaft,start_condition="Attached",end_condition="Attached",attachments=[blade1,blade2,blade3,blade4])
    Structure.add_beam(blade1,start_condition="Attached",end_conditios="Free")
    Structure.add_beam(blade2,start_condition="Attached",end_condition="Free")
    Structure.add_beam(blade3,start_condition="Attached",end_condition="Free")
    Structure.add_beam(blade4,start_condition="Attached",end_condition="Free")
    Structure.discretization #Meshes
    Structure.assembly()
```

At this point computations on the uncoupled structure can already be done if one wishes to do so

```
    #Computes the response of the uncoupled structure
    res=Structure.simulate_response(y0,tspan)

    #Plots the time response at dofs of interest
    Structure.Plot_trajectory(dofs_of_interest)

    #Makes a gif of the structure response overtime
    Structure.makegif()

    #Eigenvalues of the uncoupled structure
    eigvals,eigvects=Structure.eig_vals_state_space()
```

Finally, the rotor and stator parts are coupled and multiple computations on the coupled system can be done

```
    #Coupling of the structure

    #Requires the dofs of the hub
    dofs_hub=Structure.pick_nodes_poses([[3,1,0]])
    Coupling=Coupled_structure(Structure,dofs_hub)
    Coupling.coupling_tensorial(t_interpolation)
    #Monodromy matrix
    Coupling.Monodromy_matrix_parallel(number_of_threads)

    #Response of the coupled system, stored in Structure object
    res=Structure.simulate_response_time_coupling(y0,tspan,Coupling)

    #Makegif and plot response methods from FE_structure object can still be used with the results of the coupled system.
```

1.5 State of the art

1.5.1 Analytical models of whirl flutter

1.5.1.1 2 dof model (Taylor & Brown, 1938)

The simplest model is the *2 degree of freedom model* initially discovered in 1938. The whole wing-propeller structure is simplified by assuming the wing to be perfectly rigid. The structure therefore only consists on a clamped shaft with a rigid propeller at its tip. Furthermore, only the 2 first bending modes of the shaft are considered only allowing for a yaw ψ and pitch θ deformation of the shaft (Figure 1.4).

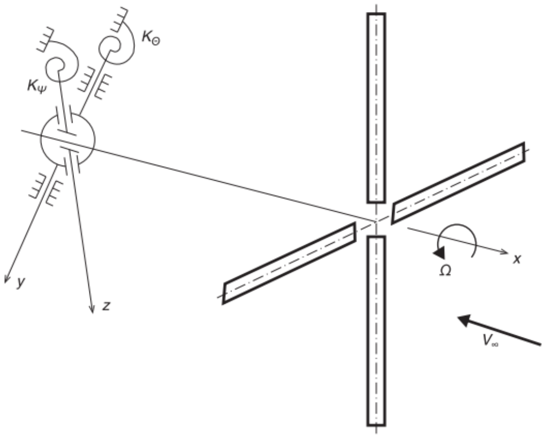

Figure 1.4: 2 degree of freedom model (Taken from Čečrdle (2015,[35])

Deriving the structural part of the equations of motions of such a model is easily done using an energetic approach with the Lagrange equation. However, one could also simply notice that this system reduces to a spinning top with additional stiffness's K_ψ, K_θ and associated structural dampings C_ψ, C_θ that shall be added to the Euler's equations of axisymmetric bodies in rotation:

$$\begin{aligned} J_y\ddot{\theta} + \frac{K_\theta \gamma_\theta}{\omega}\dot{\theta} + J_x\Omega\dot{\psi} + K_\theta\theta = Q_1 \\ J_z\ddot{\psi} + \frac{K_\psi \gamma_\psi}{\omega}\dot{\psi} - J_x\Omega\dot{\theta} + K_\psi\psi = Q_2 \end{aligned} \tag{1.1}$$

where Ω is the rotation speed of the propeller and translates the gyroscopic effects of propeller rotation. Those gyroscopic effects will turn the 2 main bending mode of the shaft turn into 2 whirl modes with the *backward* and *forward whirl modes* with the natural frequency of the first decreasing with Ω while the second one increases with Ω, as shown in Fig 1.5.

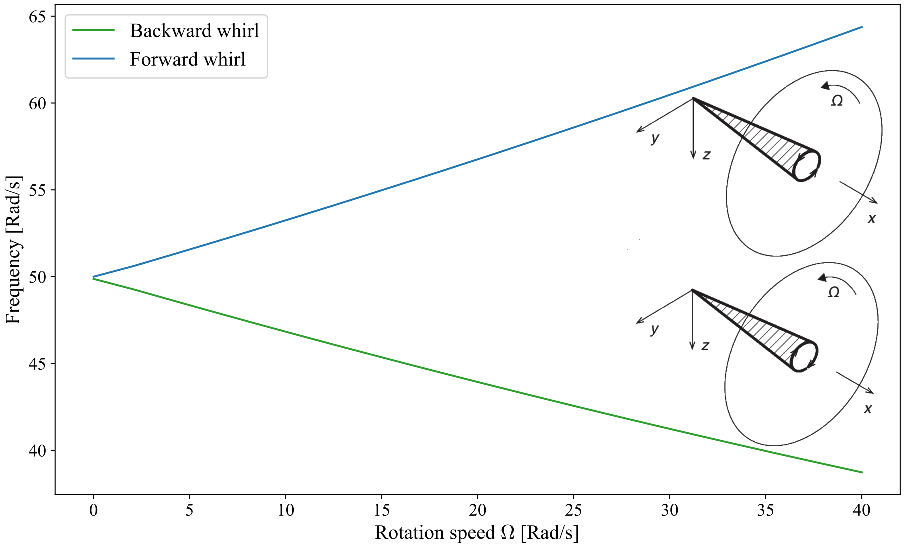

Figure 1.5: Backward and forward whirl modes of the 2-dofs model

Q_1 and Q_2 are the exterior loads which in this case only are aerodynamical loads from the incident flow at V_{inf}. Aerodynamical modeling of problems that are unsteady by nature is often the main source of approximations and the most challenging part of the problem. Even with such a simple model the quasi-steady assumption will be made and inertial aerodynamical effects will be neglected (such that terms in $\ddot{\theta}$ and $\ddot{\psi}$ are only structural. Finally exterior loads are expressed such as

$$\begin{aligned} Q_1 = M_{Y,P} - aP_Z \\ Q2 = M_{Z,P} + aP_Y, \end{aligned} \tag{1.2}$$

where $M_{Y,P}, M_{Z,P}, P_Z, P_Y$ are computed by linearization of the aerodynamical loads around small angles of attack and using aerodynamical derivatives, complete expression can be found in literature (Čečrdle (2015,[35])). The value of aerodynamical derivates usually requires experimental insights and can be experimentally retrieved in many different sources (ex: Rose, Rodden (1989,[24])). Since the aerodynamical loads are functions of the degrees of freedom θ,ψ and their first derivatives, they create an aerodynamical stiffness and damping that is added to the structural stiffness and damping. If the overall stiffness reaches 0 the system enters *Divergence* and if the overall damping reaches 0 the system enters *Flutter*, *Whirl flutter* in this case. For not too exotic geometries divergence would typically occur at much higher flow speed than flutter and therefore isn't often of great concern but remains a possible source of instability nonetheless.

This simple model allows the get a first qualitative understanding of the whirl-flutter phenomenon. As shown in Fig 1.6, 3 possible outcomes are possible as a function of the flow speed V_∞ compared to the critical speed V_r rendering the response either damped, neutrally stable or instable with the latter inducing an ever growing precession motion of the hub.

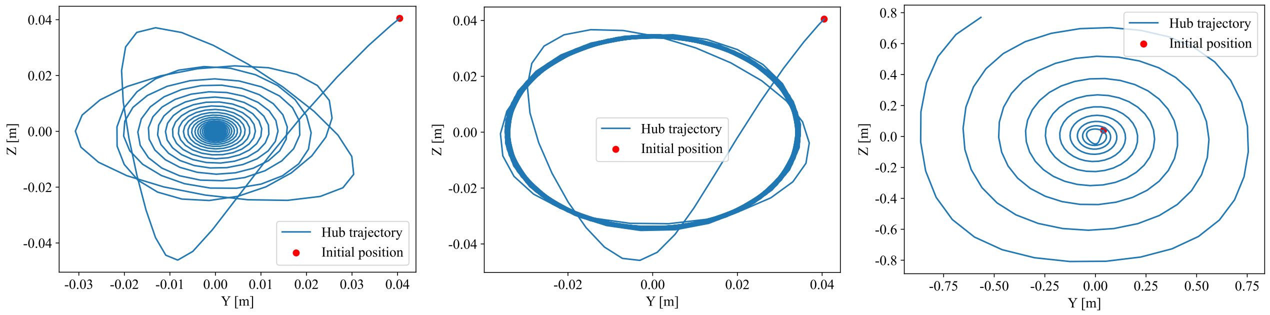

(a) $V_\infty < V_r$ (b) $V_\infty \approx V_r$ (c) $V_\infty > V_r$

Figure 1.6: Hub trajectory

If more exotic configurations are considered, for example if one of the stiffness's K_θ or K_ψ has an extremely low value then it could happen that the aerodynamical stiffness provides a softening effect large enough so as make one of the springs act like a negative spring quickly sending the system into instability as the system undergoes divergence. Fig 1.7 provides a typical response for this kind of scenarios.

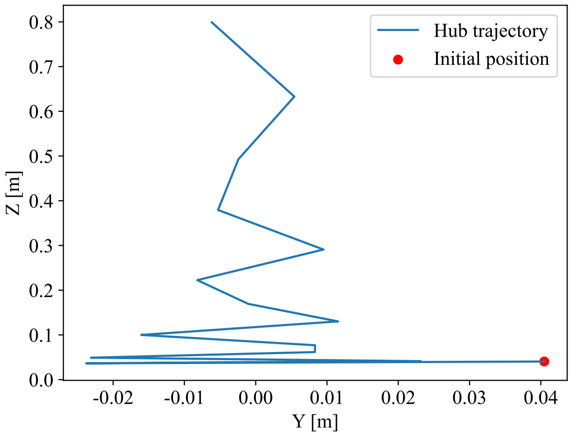

Figure 1.7: Static divergence

Finally, a stability diagram of the problem can be constructed by considering different couples of K_θ, K_ψ configurations and assessing system stability in each case, results are given in Fig 1.8. Instabilities depict a symmetric pattern around the K_θ, K_ψ line as the system is perfectly symmetric with $K_\theta = K_\psi$ being the most critical configuration.

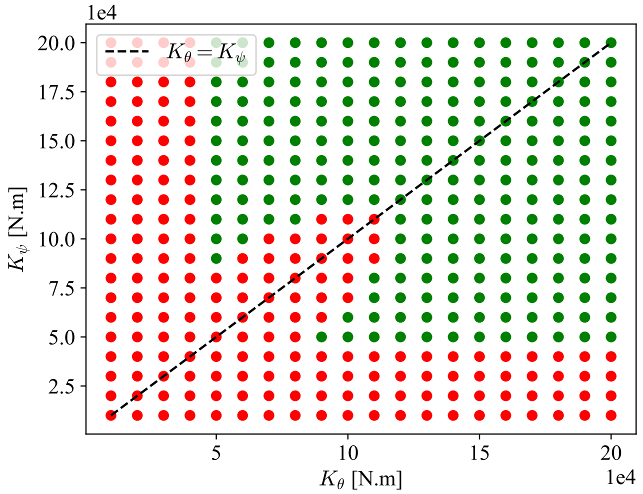

Figure 1.8: Stability diagram for the 2-dofs propeller model giving the stable and unstable configurations.

1.5.1.2 Hinged blade model (Richardson & Naylor, 1962)

The 2-dofs model assumes rigid propeller blades mountings, this assumption is perfectly acceptable for usual propeller configurations and tends to greatly simplify the problem. That being said in applications were the blades are used to generate lift (this is the case for example for helicopter applications) then blades are often hinged as to avoid unwanted large unwanted aerodynamical loads then assuming rigidly mounted blades is neglecting an important part of the dynamics of the structure.

The most classical way to handle hinged blades is to consider the Richardson & Naylor hinged blade model (1962,[20]). In addition to the 2-dofs of the shaft in yaw ψ and pitch θ the blades are mounted on the hub through rotational springs allowing them to flap and lead/lag with the blade flapping angle β_n and azimuthal angle ϕ_n totaling for 2 additional degrees of freedom. Additionally different hinge offsets e ($i.e$ how far from the hub the hinge is placed) can be considered. Figure 1.9 depicts the hinged blade model.

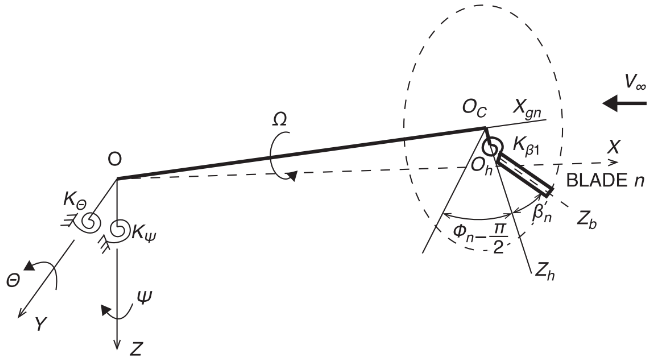

Figure 1.9: Hinged blade model (From [35]).

This model proved to give acceptable results for the backward whirl instability (Figure 1.10) but doesn't predict the existence of a forward whirl instability at all even though it is observed in practice for low hinge offsets (e/R values). Arbitrarily introducing a phase lag into the aerodynamical loads allows to artificially get a forward whirl instability prediction in some particular configurations but with inconsistent results(Reed, 1965[22]). This shows that this simple hinged blade model is lacking and cannot reliably predict the forward whirl mode instability observed in practice.

Also, the experimental results of Figure 1.10 interestingly show that the stiffness requirements to avoid backward whirl instability are greatly reduced when considered hinged blades with a large hinge offset. Yet, if a small hinge offset is considered then forward whirl instability becomes possible and strengthens the stiffness requirements to be avoided compared to the fixed blades configuration.

Finally, the hinged blade model uses one inertial coordinate system X, Y, Z fixed on the nacelle to describe the degrees of freedom θ, ψ while a rotating frame X_b, Y_b, Z_b fixed to a given blade is necessary to describe β_n, ϕ_n. As it is often the case for these kind of problems it results in the equations of motion having an explicit time dependence through the rotation matrices necessary to describe the rotating frame quantities into the fixed frame. This doesn't represent much of an issue in this case but later, for more complex non-analytical model will be a challenge to reckon with.

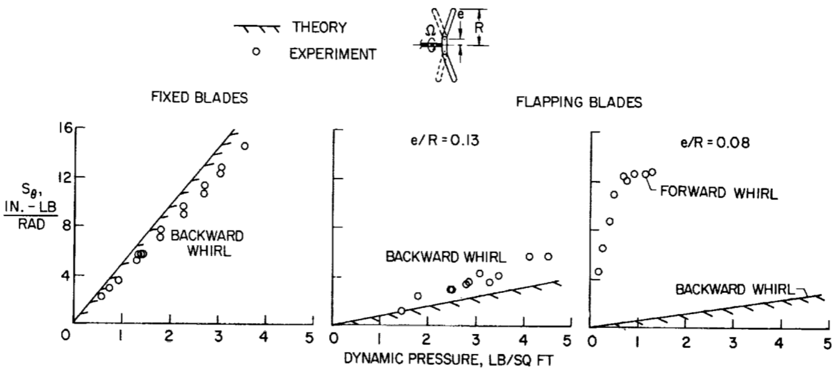

Figure 1.10: Whirl flutter stability comparison between the theoretical predictions and experimental results for the fixed (2-dofs) model and the hinged blade model using 3 different hinge offset e/R values. $S_\theta = K_\theta$ is the pitch shaft stiffness. (Reed, 1965[22]).

1.5.1.3 Flexible twisted blade model (Richardson, 1962)

In most propeller applications where the rigid blades assumptions cannot reasonably be made, the blades would typically be hinged (*e.g* helicopters) but in some applications the blades might not be hinged or/and might still undergo non-negligible elastic deformations under operation, this would for example be the case for vertical take-off off tilt-rotors or applications of propellers with an unusually large radius.

The flexible twisted blade model allows to consider the vibration modes of the elastic blade, meaning that the blades can a priori deform normal (like in the flapping blade model) or in plane of the propeller plane. Flexible modes of interest, those who can couple with whirl flutter, are the cyclic leading/lagging and flapping modes. Coning motions of the blades are negligible as they don't couple with whirl flutter (Reed, 1965[22]).

If the model is used in the vacuum then in-plane deformations of the blades can induce a forward mode instability resulting for a purely mechanical instability. This instability is characterized by a coalescence in the imaginary part of the 2 modes with one being damped and the other being unstable. This phenomena is extremely similar to the ground-resonance phenomena well known in helicopters applications. self-excited blades deformations can shift the mass center of the rotor away from its axis of rotation and induce an oscillating motion of the whole structure. When taking into account aerodynamical effects then an additional backward instability resulting from backward whirl flutter is introduced (Fig. 1.11).

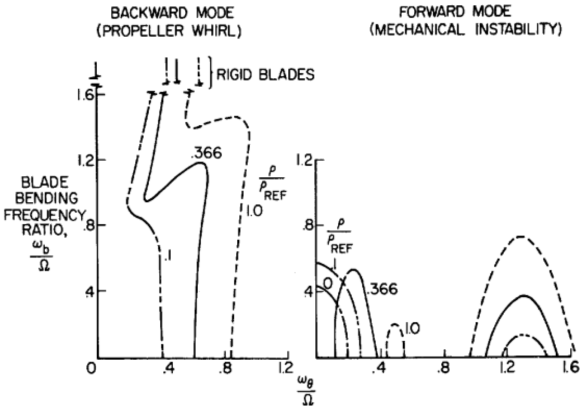

Figure 1.11: Ground-resonance instability. ω_b is a bending resonance of the blade at GVT conditions.

1.5.1.4 4-dofs model (Bennet & Bland, 1964)

In practice the propeller is mounted on a wing structure that isn't rigid. One amelioration to the model would be to consider the Bennet & Bland 4-dofs elastic wing model (1964,[19]). In addition to the 2-dofs model (θ, ψ), the wing can also admit torsion along φ and bending along h (Figure 1.12).

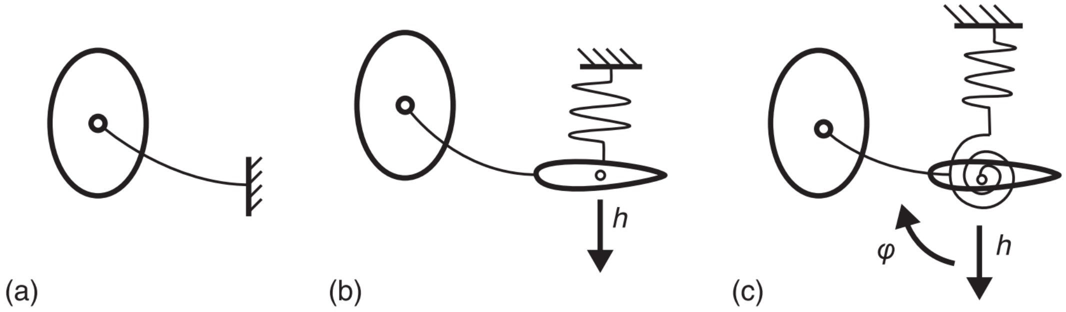

Figure 1.12: Different wing model: a) rigid, b) bending, c) bending & torsion. (Image taken from Čečrdle[35], inspired from Reed[22])

Allowing the wing to deform essentially has a stabilizing effect and reduces the stiffness requirements to avoid undergoing whirl flutter. This effect is even more visible for the bending & torsion wing. Physically, allowing the wing to deform introduces extra structural damping from the wing and allows it to alleviate energy from the propeller. The stabilizing effect is optimal at the $B1$ and $B2$ points when the whirl frequency ω_θ or ω_ψ coincides with the bending frequency of the wing ω_h *i.e* when energy extraction from propeller to wing is at its peak.

The only exception is the point C where the frequency of a coupled wing torsion-bending mode ω_1 coincides with the propeller yaw ω_ψ mode inducing a destabilizing effect.

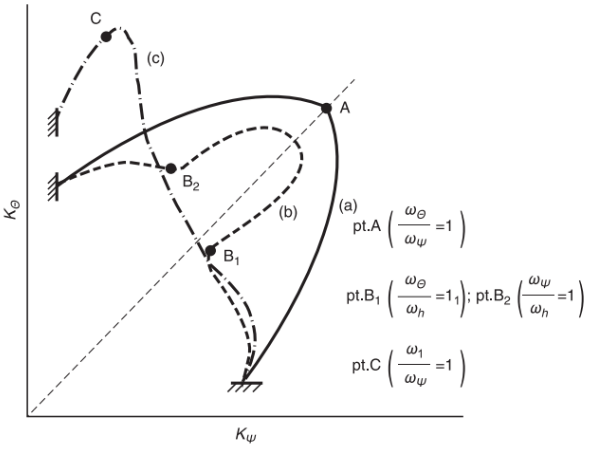

Figure 1.13: Influence of wing flexibility on whirl flutter with a) rigid, b) bending, c) bending & torsion. Advance ratio J is fixed (Image taken from Čečrdle (2015,[35]), inspired from Reed (1964,[22]))

Derivation of the equations of motion of such a model is straightforward for the structural part using an energetic approach with the Lagrangian equation. As for the aerodynamical loads they are separated between the loads from the wing and those from the propeller and are linearized around small angles of attack. Wake effects can be approximated using the Theodorsen function, doing such allows to take into account lift-lag effects due to propeller precession. Full details can be found in chapter 5 of reference [35].

1.5.2 Recent developments

Using the previously described simple analytical models proved to be sufficient until recently. Research on whirl flutter slowed greatly after the mid 1960's as satisfactory model for propeller configurations at that time had already been developed. Recently development of lighter, larger and more elastic propellers sparked interest interest in further modeling of whirl flutter instabilities.

Recent development on the whirl flutter prediction often resort to a finite element approach to allow more degrees of freedom in the system. Considering larger number of degrees of freedom opens the way to numerical methods to compute the aerodynamical parts of the equations of motion; Such as the *p-k method*,*strip theory*, panel methods (*DLM* or *VLM*) or *BEMT*.

1.5.2.1 Wing-propeller coupling

The 4-dofs analytical model in section 1.5.1.4 provides a first analytical insight on the importance of wing dynamics on whirl flutter stability.

Böhnisch Et al. (2022[5], 2024[3]) considered a coupling between the finite element discretization of a wing structure and a simple 2-dofs propeller with rigid blades, identical to what was described in section 1.5.1.1. Since the propeller blades were assumed to be rigid everything could be described in a fixed frame.

1.5.2.2 Finite element formulation of the blades

As shown using the flexible twisted blade analytical model in section 1.5.1.3 considering blade elasticity allows to capture more instability sources such as the ground resonance effect.

Experimental works (Donham, 2007[14]) also showed blade elasticity to have large effects on the whirl flutter margin especially for short pylon configurations. They observed that flutter speed associated to the whirl instabilities were largely underestimated by the rigid propeller theory. Further numerical work (Koch & Koert, 2023[10]) was also considered, with a perfectly rigid wing structure allowing all equations of motion to be written in a rotating frame of reference and obtained results comparable to experiments.

Considering blade elasticity requires to formulate equations of motion for them. Those must be expressed in a rotating frame to be time-independent. For classical rotor applications all of the structure can usually be described in a rotating frame, meaning that the problem can be solved just like in a fixed frame by simply adding non-inertial corrections through a gyroscopic matrices and non-inertial loads. This is for example what was done in reference [10].

That being said, in the context of whirl flutter we are interested in modeling the blade elasticity interaction within a blade/pylon/wing structure. The wing equations of motion shall be expressed in a fixed frame to avoid being time-dependent. This means that to express all of the quantities in one unique frame of reference will require some time-dependent change of variable for the quantities of the rotating frame. Such a procedure has already been carried out in the analytical model of the hinged blade as discussed in section 1.5.1.2 but a generalization to a finite-element model is a challenge that will be tackled in this thesis.

Chapter 2

Finite element modeling

2.1 Problem geometry

As stated previously the goal of this thesis is to develop a finite element framework that shall be able to handle various stator-rotor configurations and especially wing-propeller configurations.

A typical wing-propeller setup is usually made of up of many different elements including the engine, a transmission, engine mounts, a nacelle, bearing, dampers etc. Usually sheer amounts of different and complex parts are needed to ensure that the mechanism works properly whether it is in for propellers (Fig 2.1a) or even for helicopters (Fig 2.1b).

(a) C-130 Hercules variable pitch propeller[12]

(b) IAR 330 Puma swash plate[13]

Figure 2.1: Variable pitch propeller & helicopter swash plate

As for the blades themselves they are usually of complex geometries with varying cord along and pitch the span to avoid flow separation.

Due to the amount of computational power required to numerically integrate the problem and assess its stability it is of best interest to reduce the number of degrees of freedom as much as possible. Moreover, since the aerodynamics effects aren't considered in this thesis simplification of the geometry can also be made as it's interactions with the air flow won't be taken into account.

These 2 considerations lead to great simplification of the problem. Fig 2.2 depicts a typical wing-propeller setup as it will be modeled in this thesis. The wing, the pylon as well as the blades will be assumed to be beams of rectangular sections. Doing such essentially reduces the problem to 1 dimension in the local frame of each element making computations much faster and allowing a large reduction of the required degrees of freedom for convergence of the model. As for the fuselage it is assumed to be rigid, giving a clamped boundary condition to the problem.

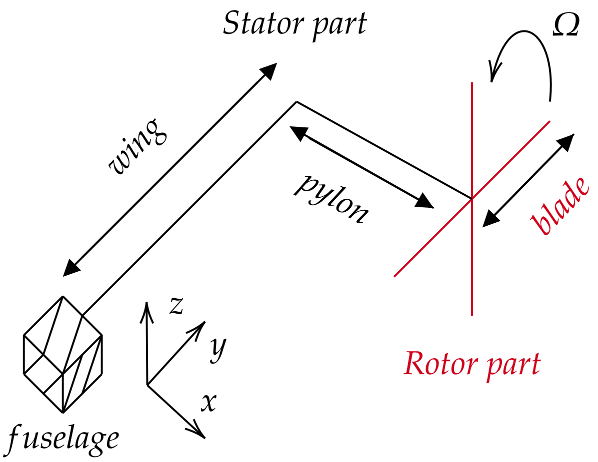

Figure 2.2: Simplified model of a wing-propeller configuration

As depicted by Fig 2.2 the model is clearly divided between the *Stator* and *Rotor* part. The former, consisting of the pylon, wing and fuselage gives the static part of the structure and thereby shall be described in a fixed frame of reference. The latter, made up of the blades of the propeller gives the rotor part of the structure and is best described in a rotating frame of reference fixed onto the blades. Note that the hub of the propeller is the only part of the structure that is simultaneously part of the rotor and the stator, this will be of great interest in latter chapters.

2.2 Stator finite element modeling

2.2.1 Finite element method

2.2.1.1 Philosophy

In the context of mechanical structures the finite element method aims at providing a spatial discretization of complex structures into smaller sub elements for which the shape of the displacement field can be assumed. This allows to transform the partial differential equations from the continuity principles ordinary differential equations.

2.2.1.2 Rayleigh-Ritz approximation

Let a very simple structure where the Rayleigh-Ritz approximation of the displacement field can be made on the whole structure such that

$$u_{i,}(x,y,z,t) = \sum_{j=1}^{n} \phi_{i,j}(x,y,z) q_j(t) \text{ for i=1, 2, 3} \tag{2.1}$$

where $\phi_{i,j}$ are kinematically admissible test functions (*i.e* they are continuous on the element and satisfy the problem boundary conditions) and $q_j(t)$ the amplitude of the degree of freedom j, they are the unknowns of the problem. The Rayleigh-Ritz approximation can be seen as an interpolation of the generalized displacements $q_j(t)$ to translate their impact on the displacement at element level $\boldsymbol{u}(\boldsymbol{x}, t)$. Following that interpretation the interpolation matrix $\boldsymbol{N}$ is introduced such that

$$\boldsymbol{u}(\boldsymbol{x}, t) = \boldsymbol{N}(\boldsymbol{x})\boldsymbol{q}(t). \tag{2.2}$$

Not only the displacements but also the strains can be interpolated from the generalized displacements using a strain interpolation matrix $\boldsymbol{B}$

$$\boldsymbol{\varepsilon}(\boldsymbol{x}, t) = \boldsymbol{B}(\boldsymbol{x})\boldsymbol{q}(t). \tag{2.3}$$

Expecting an energetic approach this allows to already compute the kinetic and potential energy of the structure and then inject the interpolation displacement field as it was defined above.

The kinetic energy is directly computed from

$$\begin{aligned} T =& \frac{1}{2}\int_{V_0} \rho_0 \; \dot{\boldsymbol{u}}^T \dot{\boldsymbol{u}} \; dV \\ =& \frac{1}{2}\dot{\boldsymbol{q}}^T \int_{V_0} \rho_0 \boldsymbol{N}^T \boldsymbol{N} \; dV \dot{\boldsymbol{q}} \\ =& \frac{1}{2}\dot{\boldsymbol{q}}^T \boldsymbol{M} \dot{\boldsymbol{q}} \end{aligned} \tag{2.4}$$

where $\boldsymbol{M}$ is the mass matrix of the structure.

The internal potential energy is expressed as

$$V_{int} = \frac{1}{2}\int_{V_0} \boldsymbol{\sigma}^T \boldsymbol{\varepsilon} \; dV. \tag{2.5}$$

Under the assumption of small deformations, the generalized Hooke's law allows the link the stress and strain tensors through the elasticity matrix $\boldsymbol{E}$

$$\boldsymbol{\sigma} = \boldsymbol{E} \otimes \boldsymbol{\varepsilon} \tag{2.6}$$

such that

$$\begin{aligned} V_{int} =& \frac{1}{2}\int_{V_0} \boldsymbol{\varepsilon}^T \boldsymbol{E} \boldsymbol{\varepsilon} \; dV \\ =& \frac{1}{2}\boldsymbol{q}^T \int_{V_0} \boldsymbol{B}^T \boldsymbol{E} \boldsymbol{B} \; dV \boldsymbol{q} \\ =& \frac{1}{2}\boldsymbol{q}^T \boldsymbol{K} \boldsymbol{q} \end{aligned} \tag{2.7}$$

with $\boldsymbol{K}$ the stiffness matrix of the structure.

Finally, the potential energy due to exterior loads is computed through

$$V_{ext} = -\int_{V_0} \boldsymbol{u}^T \bar{\boldsymbol{X}} \; dV - \int_{S_\sigma} \boldsymbol{u}^T \bar{\boldsymbol{t}} \; dS = -\boldsymbol{q}^T \boldsymbol{g} \tag{2.8}$$

with $\boldsymbol{g}$ the external load vector and $\bar{\boldsymbol{X}}$, $\bar{\boldsymbol{t}}$ respectively the body forces and the surface forces applied on the structure.

2.2.1.3 Hamilton principle

The Hamilton principle states that the integral of the Lagrangian between 2 different instants t_1, t_2 for an holonomic system remains stationary *i.e*

$$\delta \int_{t_1}^{t_2} \mathcal{L} \; dt = \delta \int_{t_1}^{t_2} (T - (V_{ext} + V_{int})) \; dt = 0. \tag{2.9}$$

Using the previously obtained results of section 2.2.1.2 into the Hamilton principle yields

$$\boldsymbol{M}\ddot{\boldsymbol{q}} + \boldsymbol{K}\dot{\boldsymbol{q}} = \boldsymbol{g}(t) \tag{2.10}$$

depicting a linear system of ordinary different equations or in other words the equations of motion of the structure.

2.2.1.4 Finite element approach

The 2 previous sections showed how the equations of motion can be computed by doing a Rayleigh-Ritz approximation on the whole structure. This approach has the issue that the quality of the approximation is greatly dependent on the choice of the test functions ϕ. Such a choice is easy for simple geometries but becomes extremely hazardous for more complex cases.

The finite element approach suggests to instead subdivide the structure into smaller and simpler elements on which a Rayleigh-Ritz approximation can be done but at the element level. This yields to computation of various mass and stiffness matrices $\boldsymbol{M_e}, \boldsymbol{K_e}$ at the element level, expressed in the element frame which can be then be expressed in the structural frame using a transformation matrix $\boldsymbol{T}$ such that

$$\boldsymbol{M}_{e,S} = \boldsymbol{T}^T \boldsymbol{M_e} \boldsymbol{T} \text{ and } \boldsymbol{K}_{e,S} = \boldsymbol{T}^T \boldsymbol{K_e} \boldsymbol{T} \tag{2.11}$$

with $\boldsymbol{M}_{e,S}$ and $\boldsymbol{K_{e,S}}$ the elemental structural matrices in the structural frame. These matrices can finally be assembled into the structural matrices $\boldsymbol{M}, \boldsymbol{K}$ of the whole structure according to the degrees of freedom influenced by each element of the structure.

2.2.2 Structural matrices in the fixed frame

With the adding of damping, equations of motion in a fixed frame of reference can be written as

$$\boldsymbol{M}\ddot{\boldsymbol{q}}(t) + \boldsymbol{C}\dot{\boldsymbol{q}}(t) + \boldsymbol{K}\boldsymbol{q}(t) = \boldsymbol{g}(t) \tag{2.12}$$

where $\boldsymbol{M}, \boldsymbol{K}, \boldsymbol{C}$ respectively are the structural mass, stiffness and damping matrices. Their computation is done using the finite element method and as such requires the choice of the type of elements to be used in the thesis.

As discussed at the beginning of this chapter all the structure is modeled using beam thereby offering beams elements as an obvious choice. The chosen beam elements are 3*D* *Euler-Bernoulli* beam elements (Fig 2.3) as it is desirable that compression, bending and torsion are taken into account with the model.

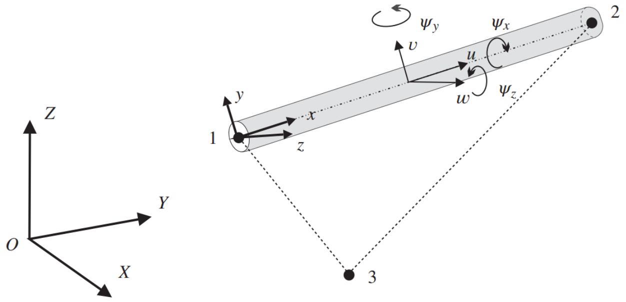

Figure 2.3: 3*D* Euler-Bernoulli beam element. x, y, z depict the element frame while X, Y, Z give the structural frame. Illustration taken from Géradin *et al.* (2015, p386[9])

This mean that 6 degrees of freedom per node; or 12 degrees of freedom per beam element are to be considered such that for a given beam element reading

$$\boldsymbol{q}^{eT} = \begin{bmatrix} u_1 & v_1 & w_1 & \psi_{x1} & \psi_{y1} & \psi_{z1} & u_2 & v_2 & w_2 & \psi_{x2} & \psi_{y2} & \psi_{z2} \end{bmatrix} \tag{2.13}$$

The structural matrices at the element level are then directly derived from the choice of the shape functions written in the element frame. Those shape functions and the symbolic formulation of the $\boldsymbol{M}_e$ and $\boldsymbol{K}_e$ matrices are given in the Appendix A.

Moreover, as the Euler-Bernoulli elements cannot model shearing *Timoshenko* beam elements were considered as well to improve the quality of the model. This approach is recommended by Géradin *et. al*([9]) and tends to make the results significantly better if the beam isn't slender. Essentially the Timoshenko beam elements are an extension the Euler-Bernoulli element where a correction factor is applied on some elements of the structural matrices. Correction is made on the stiffness matrix through the Φ_y and Φ_z shearing coefficients coefficients (Przemieniecki, (1968, [17])

$$\Phi_y = \frac{12EI_z}{kGAL^2} \text{ and } \Phi_z = \frac{12EI_y}{kGAL^2}, \tag{2.14}$$

where L is the beam length and k is a geometrical coefficient depending on section geometry (Tables are often found in the literature e.g Cowper (1966,[1])). An inertial correction is also applied for $\boldsymbol{M}_{el}$ but with a much lower impact since eigensolutions are much more sensible to stiffness modifications.

2.2.2.1 Damping matrix

The damping matrix $\boldsymbol{C}$ will be computed using the very simple model of proportional damping. This assumptions assures diagonal damping and therefore the formation of uncoupled normal equations. The damping matrix therefore reads

$$\boldsymbol{C} = \alpha\boldsymbol{K} + \beta\boldsymbol{M}, \tag{2.15}$$

with α, β real constants.

Moreover, using this model allows to rewrite the modal damping of each mode as

$$\zeta_i = \frac{1}{2}(\alpha\omega_i + \frac{\beta}{\omega_i}), \tag{2.16}$$

where ζ_i is the modal damping of the mode i and ω_i its undamped natural frequency. Values of α and β are therefore found by assuming a value of modal damping for 2 modes and solving the following system of equations

$$\begin{cases} \zeta_1 = \frac{1}{2}(\alpha\omega_1 + \frac{\beta}{\omega_1}) \\ \zeta_2 = \frac{1}{2}(\alpha\omega_2 + \frac{\beta}{\omega_2}). \end{cases} \tag{2.17}$$

There naturally exist much more refined models of damping but these won't be investigated in this thesis as developing an accurate and non arbitrary model of damping requires experimental testing. Furthermore, the amount of structural damping, as long as it remains under the assumptions of weak damping, isn't expected to change the nature of the *whirl-flutter* instabilities this thesis aims at studying. Damping will nonetheless remain an important parameter but mostly for numerical integration concerns, as it will be extensively discussed in the section 4.3.2.

2.2.3 Finite element code verification

Verification of the implemented finite element code was done by computing the eigenfrequencies and modes of the structure and compare these results to a commercial software, in this thesis the *Samcef* module from Siemens *NX* was used.

To test the implemented software capabilities, a mildly complex configuration was considered to mimic a wing/propeller configuration at ground conditions ($\Omega = 0$ RPM) using square section beams (Fig 2.4). For the proposed geometry, the eigenfrequencies of the undamped structure were computed using *Euler* or *Timoshenko* elements with the in-house software and compared to *NX* in Table 2.2. Most computed eigenfrequencies are extremely close to those of *NX* except the third and seventh modes that show the largest deviation from the commercial software, these differences could be attributed to the fact that these 2 modes are essentially in terms of torsion and that Timoshenko elements do not take warping into account which is deemed to occur on non-circular sections.

Nonetheless, results clearly validate the in-house implementation of the FE method with most modes being extremely close to those of *NX*. It is to be noted that using *Timoshenko* elements tends to indeed consistently improve the quality of the results even if it is by a small margin.

Parameters	**Value**	**Units**
Young modulus E	210	GPa
Poisson ratio ν	0.3	-
Density ρ	7800	kg/m^3
Height h	0.05	m
Width b	0.05	m

Table 2.1: Material properties and section geometry.

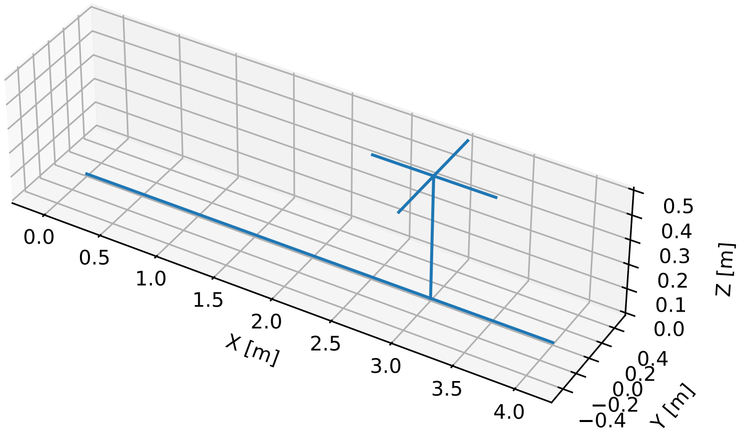

Figure 2.4: Simple wing-propeller configuration mimicry. All beams have the same material and section properties stated in Table 2.1. The main beam is clamped in frame origin to mimic a wing and is 4m long while the pylon and each blade are 0.5m long.

	ω_{Euler} [Hz]	$\Delta\omega_{Euler}$ [%]	$\omega_{Timoshenko}$ [Hz]	$\Delta\omega_{Timoshenko}$ [%]	ω_{NX} [Hz]
Mode 1	1.78	0.28	1.78	0.11	1.78
Mode 2	1.78	0.12	1.78	0.02	1.78
Mode 3	9.68	7.80	9.67	7.71	8.98
Mode 4	12.14	0.16	12.14	0.08	12.14
Mode 5	15.03	0.60	15.02	0.53	14.94
Mode 6	31.93	0.23	31.92	0.19	31.86
Mode 7	34.32	5.75	34.28	5.58	32.46
Mode 8	42.02	0.21	41.97	0.09	41.93
Mode 9	44.64	1.36	44.60	1.27	44.04
Mode 10	79.80	0.38	79.73	0.29	79.50
Mode 11	80.74	0.55	80.62	0.41	80.30
Mode 12	99.96	0.86	99.69	0.58	99.11
Mode 13	111.94	0.72	111.68	0.49	111.14
Mode 14	152.51	0.86	152.29	0.72	151.21
Mode 15	153.48	0.76	153.19	0.58	152.34

Table 2.2: Eigenfrequencies for the simple structure; Frequencies obtained with Euler and Timoshenko are compared to those obtained with the commercial software using their relative difference $\Delta\omega$ with NX taken as a reference. For both the in-house and commercial software 20 elements per beam were considered.

2.2.4 FE code convergence

In order to select an appropriate number of element per beam convergence is studied for the simple structure of Fig. 2.4. Results are given in Figure 2.5 and clearly shows that taking into account only few elements per beam is enough for most of the modes. That being said some higher order modes seems to be requiring more degrees of freedom to converge. As a conclusion it appears wise to use at least 4 elements per beam.

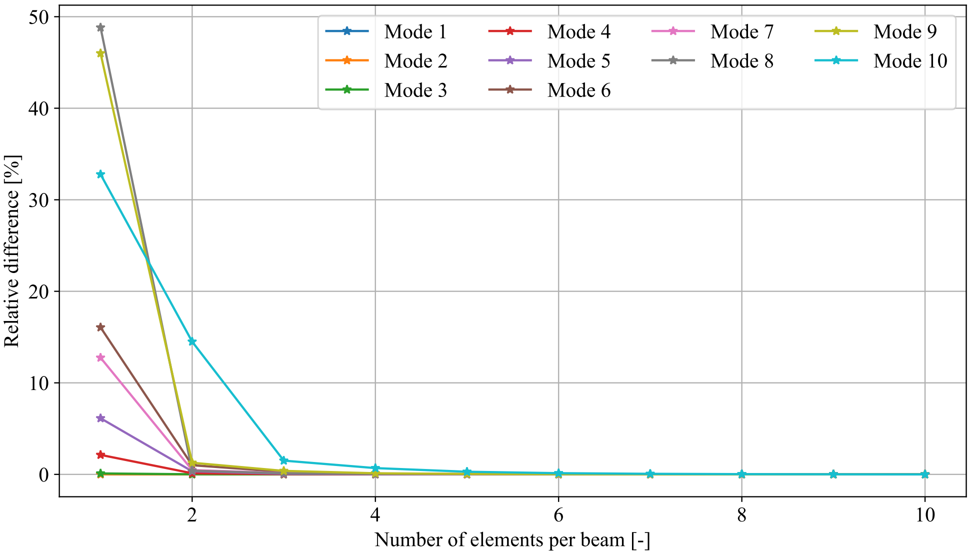

Figure 2.5: Convergence of the eigenfrequencies for the stator. The relative difference is computed using the results for 10 elements per beam as a reference.

2.3 Rotor finite element modeling

2.3.1 Finite element formulation of elastic solids in rotation (From [26])

Let an inertial frame x, y, z and a non-inertial frame x', y', z' attached to an elastic body rotating along $\boldsymbol{\omega}$ such as described by Figure 2.6.

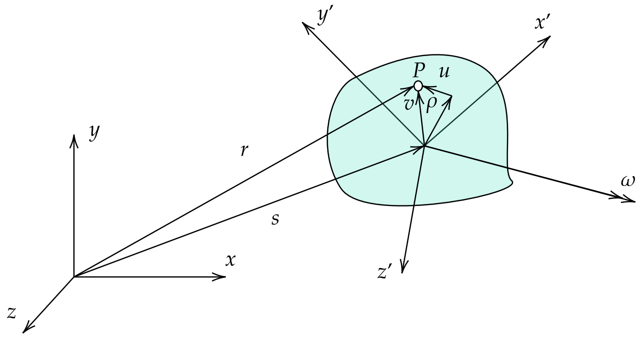

Figure 2.6: Elastic solid in rotation

The position of a point P on the rotating body as seen the frame in x', y', z' reads:

$$\boldsymbol{v}(\boldsymbol{x}, t) = \boldsymbol{x} + \boldsymbol{u}(\boldsymbol{x}, t), \tag{2.18}$$

where is the initial position of point P and $\boldsymbol{u}$ its displacement due to solid deformation. When described in the inertial frame x, y, z the position of a point P reads:

$$\boldsymbol{r}(\boldsymbol{x}, t) = \boldsymbol{s} + \boldsymbol{\Theta}\boldsymbol{v}, \tag{2.19}$$

i.e with a translation $\boldsymbol{s}$ and a rotation $\boldsymbol{\Theta}$ of the inertial frame.
Defining the components of the rotation vector $\boldsymbol{\omega} = [\omega_1, \omega_2, \omega_3]$ induces that the rotation speed matrix $\boldsymbol{\Omega}$ is such that:

$$\boldsymbol{\Omega} = \begin{bmatrix} 0 & -\omega_3 & \omega_2 \\ \omega_3 & 0 & -\omega_1 \\ -\omega_2 & \omega_1 & 0 \end{bmatrix}, \boldsymbol{\Theta}^T\boldsymbol{\Theta} = \mathbb{I} \tag{2.20}$$

Finally, in the context of the finite element method the displacement field at the element level $\boldsymbol{u}$ is expressed through the shape functions matrix $\boldsymbol{N}$ and the nodal degrees of freedom $\boldsymbol{q}$ reading:

$$\boldsymbol{u}(x_i, t) = \boldsymbol{N}(x_i)\boldsymbol{q}(t). \tag{2.21}$$

2.3.1.1 Kinetic energy

The kinetic energy of the whole solid is obtained by volume integration such that:

$$T = \frac{1}{2}\int_V \rho \dot{\boldsymbol{r}}^T \dot{\boldsymbol{r}} dV. \tag{2.22}$$

Using eq 2.21 and assuming no translation *i.e* $\boldsymbol{s} = \boldsymbol{0}$ into the definition of the kinetic energy yields:

$$\begin{aligned} T = &\frac{1}{2}\int_V \rho \dot{\boldsymbol{q}}^T \boldsymbol{N}^T \boldsymbol{N} \dot{\boldsymbol{q}}\, dV + \int_V \rho \dot{\boldsymbol{q}}^T \boldsymbol{N}^T \boldsymbol{\Omega} \boldsymbol{N} \boldsymbol{q}\, dV - \frac{1}{2}\int_V \rho \boldsymbol{q}^T \boldsymbol{N}^T \boldsymbol{\Omega}^2 \boldsymbol{N} \boldsymbol{q}\, dV \\ &- \int_V \rho \boldsymbol{q}^T \boldsymbol{N}^T \boldsymbol{\Omega}^2 \boldsymbol{x}\, dV - \frac{1}{2}\int_V \rho \boldsymbol{x}^T \boldsymbol{\Omega}^2 \boldsymbol{x}\, dV + \int_V \rho \dot{\boldsymbol{q}}^T \boldsymbol{N}^T \boldsymbol{\Omega} \boldsymbol{x}\, dV, \end{aligned} \tag{2.23}$$

where $\boldsymbol{\Omega}^2 = -\boldsymbol{\Omega}\boldsymbol{\Omega}^T$.

2.3.1.2 Strain energy

Assuming small deformations such that the solid remains in the elastic domain allows to link the stress and strain tensors by the generalized Hooke's law reading:

$$\boldsymbol{\sigma} = \boldsymbol{E} : \varepsilon, \tag{2.24}$$

where $\boldsymbol{E}$ is the elasticity matrix, $\boldsymbol{\sigma} = \begin{bmatrix}\sigma_{11} & \sigma_{22} & \sigma_{33} & \sigma_{23} & \sigma_{31} & \sigma_{12}\end{bmatrix}$ the stress vector and $\boldsymbol{\varepsilon} = \begin{bmatrix}\varepsilon_{11} & \varepsilon_{22} & \varepsilon_{33} & 2\varepsilon_{23} & 2\varepsilon_{31} & 2\varepsilon_{12}\end{bmatrix}$ the strain vector. The strain energy over the whole solid therefore reads

$$\mathcal{U} = \frac{1}{2}\int_V \boldsymbol{\varepsilon}^T \boldsymbol{E}\boldsymbol{\varepsilon} dV. \tag{2.25}$$

Once again in the context of the finite element method, the strain interpolation matrix $\boldsymbol{B}$ is introduced to link the strain $\boldsymbol{\varepsilon}$ to nodal displacements $\boldsymbol{q}$

$$\boldsymbol{\varepsilon}(x_i, t) = \boldsymbol{B}(x_i)\boldsymbol{q}(t), \tag{2.26}$$

with $\boldsymbol{B}$ being directly derived by derivation of the shape functions $\boldsymbol{N}$. Strain energy therefore becomes

$$\mathcal{U} = \frac{1}{2}\int_V \boldsymbol{q}^T \boldsymbol{B}^T \boldsymbol{E}\boldsymbol{B}\boldsymbol{q} dV. \tag{2.27}$$

Finally, since the influence of gravity is neglected the potential energy V is only in terms of strain energy $\mathcal{U}$ such that $V = \mathcal{U}$.

2.3.1.3 Lagrange equations

The equations of motion are obtained through the principle of least action as it holds true even in a non-inertial frame. The Lagrange equations read:

$$-\frac{d}{dt}(\frac{\partial T}{\partial \dot{\boldsymbol{q}}}) + \frac{\partial T}{\partial \boldsymbol{q}} - \frac{\partial V}{\partial \boldsymbol{q}} - \boldsymbol{Q}_D = \boldsymbol{Q}_E, \tag{2.28}$$

where T is the kinetic energy, V the potential energy of deformation of the solid and finally Q_D,Q_E respectively represent the generalized damping and exterior forces. Assuming Rayleigh damping *i.e* that damping forces are proportional to nodal velocities, $\dot{\boldsymbol{q}}$, allows to rewrite these equations as:

$$-\frac{d}{dt}(\frac{\partial T}{\partial \dot{\boldsymbol{q}}}) + \frac{\partial T}{\partial \boldsymbol{q}} - \frac{\partial V}{\partial \boldsymbol{q}} + \frac{\partial D}{\partial \dot{\boldsymbol{q}}} = \boldsymbol{Q}_E, \tag{2.29}$$

2.3.1.4 Equations of motion in the rotating frame

From the expressions of the kinetic and potential energy previously obtained and the Lagrange principle as written in equation 2.29, the matrix form of the equations of motion of a rotating solid take the following expression

$$\boldsymbol{M}\ddot{\boldsymbol{q}} + (\boldsymbol{C} + \boldsymbol{G})\dot{\boldsymbol{q}} + (\boldsymbol{K} + \boldsymbol{K_\Omega} + \boldsymbol{K_g})\boldsymbol{q} = \boldsymbol{F_\Omega} + \boldsymbol{Q_E}. \tag{2.30}$$

The following elemental structural matrices are identified:

$$\boldsymbol{M} = \int_V \rho \mathbf{N}^T \mathbf{N}\ dV, \tag{2.31}$$

with $\boldsymbol{M}$ the mass matrix.

$$\boldsymbol{K} = \int_V \mathbf{B}^T \mathbf{E} \mathbf{B}\ dV, \tag{2.32}$$

with $\boldsymbol{K}$ the stiffness matrix.

$$\boldsymbol{G} = \int_V 2\rho \mathbf{N}^T \boldsymbol{\Omega} \mathbf{N}\ dV, \tag{2.33}$$

with $\boldsymbol{G}$ the gyroscopic or Coriolis effect matrix.

$$\boldsymbol{K}_\Omega = \int_V \rho \mathbf{N}^T \boldsymbol{\Omega}^2 \mathbf{N}\ dV, \tag{2.34}$$

with $\boldsymbol{K_\Omega}$ the centrifugal softening stiffness matrix. This matrix is a translation of the effects of the centrifugal force that tends to soften the overall stiffness of the structure.

$$\boldsymbol{K}_g = \int_V \boldsymbol{N}'^T \boldsymbol{\sigma}_0 \boldsymbol{N}'\ dV, \tag{2.35}$$

with $\boldsymbol{K}_g$ the centrifugal stiffening matrix. This matrix translates the stiffening of the beams due to press-stress induced by the displacements $\boldsymbol{q}_0$ due the centrifugal loads for the static problem $(\boldsymbol{K}+\boldsymbol{K}_\Omega)\boldsymbol{q}_0 = \boldsymbol{F}_{\boldsymbol{\Omega}}$.

$$\boldsymbol{F}_\Omega = -\int_V \rho \boldsymbol{N}^T \boldsymbol{\Omega}^2 \boldsymbol{r} \; dV, \tag{2.36}$$

with $\boldsymbol{F}_\Omega$ the centrifugal loads and $\boldsymbol{r}$ the location vector from the axis of rotation of the structure to the center of the element.

Finally, $\boldsymbol{Q}_{\boldsymbol{E}}$ represents generalized exterior loads *e.g* the aerodynamic loads in the case. Since no aerodynamical effects are considered in this thesis, $\boldsymbol{Q}_{\boldsymbol{E}} = \boldsymbol{0}$.

2.3.2 Gauss quadrature

As seen in the section 2.3.1.4, computation of the matrices of the equations of motion shall be done using volume integrals of polynomials (since the shape functions $\boldsymbol{N}$ are polynomials). Such an application calls for a Gauss quadrature for a fast numerical computation of the integrals.

2.3.2.1 General procedure

Starting from a simple one dimension integral such as:

$$\int_a^b f(x)dx, \tag{2.37}$$

it's expression will be approximated by a sum of weights w_i and evaluation of f at given nodes x_i, $f(x_i)$, yielding:

$$\int_a^b f(x)dx \approx \sum_i^n w_i f(x_i), \tag{2.38}$$

where n is such that if $f(x)$ is a polynomial of degree less than $2n-1$ integration is exact.
Quality of the approximation in all other cases depends on how close to a polynomial f behaves and if n was chosen sufficiently large.

Extension to multiple dimensions cases is immediate since the integration can be carried out dimension by dimension according to the *Fubini's* theorem (1907,[8]), with a gauss quadrature that can be applied for each dimension. *E.g* in the 3 dimensions case:

$$\int_{a_1}^{b_1}\int_{a_2}^{b_2}\int_{a_3}^{b_3} f(x,y,z)\, dxdydz \approx \sum_i^{n_1}\sum_j^{n_2}\sum_k^{n_3} w_i w_j w_k\, f(x_i, y_j, z_k) \tag{2.39}$$

2.3.2.2 Gauss-Legendre quadrature

There exist multiple methods to obtain the weights w_i and quadrature nodes x_i to perform the Gauss-quadrature. The most commonly used in the context of finite element method is the *Gauss-Legendre* quadrature.

Weights w_i with Gauss-Legendre are computed using:

$$w_i = \frac{2}{(1-x_i^2)[\frac{dP_n}{dx}]_{x_i}}, \tag{2.40}$$

where $P_n(x)$ are the Legendre polynomials and the quadrature nodes x_i are their roots.

Legendre polynomials are conveniently generated numerically by expression them as a power series and using a recurrence formula for the coefficients:

$$P_n(x) = \sum_k a_k x^k \text{ with } a_k = -\frac{(n-k)(n+k+1)}{(k+2)(k+1)} a_k, \tag{2.41}$$

where $(a_0, a_1) = (0, 1)$ if n is odd or $(a_0, a_1) = (1, 0)$ if n is even.

A Legendre polynomial $P_n(x)$ as n real roots comprised between $[-1, 1]$. Different methods can be used to retrieve their roots numerically, one of them being to use *Chebyshev* polynomials series(Boyd, 2002[4]). To get the equations of motion of the rotating part of the structure the matrices shall be computed through an integral.

2.3.3 Numerical integration of the matrices in the rotating frame

As stated at the beginning of this chapter at the element frame level the problem reduces to only one dimension. This allows to greatly simplify the integrals as the shape functions $\boldsymbol{N}(\xi = \frac{x}{l}, \eta = \frac{y}{l}, \zeta = \frac{z}{l})$ are reduced to only be a function of $\xi = \frac{x}{l}$. A change of variable on the limits of integration will also be required such as to be able to apply the Gauss-Legendre quadrature. Starting with the mass matrix

$$\begin{aligned}
\boldsymbol{M} &= \int_V \rho \boldsymbol{N}^T \boldsymbol{N} dV \\
&= \int_0^h \int_0^b \int_0^l \rho \boldsymbol{N}^T \boldsymbol{N} \, dx \, dy \, dz \\
&= \rho A \int_0^l \boldsymbol{N}^T \boldsymbol{N} \, dx, \text{ Let } \xi = \frac{x}{l} \\
&= \rho A l \int_0^1 \boldsymbol{N}^T \boldsymbol{N} d\tilde{\xi}, \text{ Let } \tilde{\xi} = 2\xi - 1 \\
&= \frac{\rho A l}{2} \int_{-1}^1 \boldsymbol{N}^T(\tilde{\xi}) \boldsymbol{N}(\tilde{\xi}) d\tilde{\xi},
\end{aligned} \tag{2.42}$$

effectively reducing to a 1D integral. One must be cautious that the shape-functions, at least as they are defined in appendix A, require $\xi = \frac{x}{l}$ as argument while it is $\tilde{\xi}$ that is used for the integral. The same process is applied to the other matrices reading

$$\begin{aligned}
\boldsymbol{G} &= \int_V 2\rho \boldsymbol{N}^T \boldsymbol{\Omega} \boldsymbol{N} dV \\
&= \frac{2\rho A l}{2} \int_{-1}^1 \boldsymbol{N}^T(\xi) \boldsymbol{\Omega} \boldsymbol{N}(\xi) d\xi \\
\boldsymbol{K}_\Omega &= -\int_V \rho \boldsymbol{N}^T \boldsymbol{\Omega}^2 \boldsymbol{N} dV \\
&= -\frac{\rho A l}{2} \int_{-1}^1 \boldsymbol{N}^T(\xi) \boldsymbol{\Omega}^2 \boldsymbol{N}(\xi) d\xi \\
\boldsymbol{F}_\Omega &= -\int_V \rho \boldsymbol{N}^T \boldsymbol{\Omega}^2 \boldsymbol{r} dV \\
&= -\frac{\rho A l}{2} \int_{-1}^1 \boldsymbol{N}^T(\xi) \boldsymbol{\Omega}^2 \boldsymbol{r} d\xi
\end{aligned} \tag{2.43}$$

where $\boldsymbol{r}$ is the location vector from the axis of rotation of the structure to the center of the element. Finally, it only remains $\boldsymbol{K}_g$ that requires a special treatment. Indeed, the centrifugal stiffening matrix can be expressed such as

$$(\boldsymbol{K}_g)_{p,q} = \int_V \sigma^0_{i,j} \frac{\partial N_{k,p}}{\partial x_i} \frac{\partial N_{k,q}}{\partial x_j} \, dV, \tag{2.44}$$

using that fact that the shape-functions only depend on $\xi = \frac{x}{l}$ forces $i = j = 0$ such that

$$\begin{aligned}
(\boldsymbol{K}_g)_{p,q} =& A\sigma^0 \int_0^l \frac{\partial N_{k,p}}{\partial x} \frac{\partial N_{k,q}}{\partial x} \, dx, \text{ Let } \xi = \frac{x}{l} \\
=& \frac{A\sigma^0}{l} \int_0^1 \frac{\partial N_{k,p}}{\partial \xi} \frac{\partial N_{k,q}}{\partial \xi} \, d\xi, \text{ Let } \tilde{\xi} = 2\xi - 1 \\
=& \frac{2A\sigma^0 l}{4l^2} \int_{-1}^1 \frac{\partial N_{k,p}}{\partial \tilde{\xi}} \frac{\partial N_{k,q}}{\partial \tilde{\xi}} \, d\tilde{\xi}, \text{ Let } \tilde{\xi} = 2\xi - 1
\end{aligned} \tag{2.45}$$

which is conveniently rewritten in matrix form

$$\boldsymbol{K}_g = \frac{A\sigma^0}{2l} \int_{-1}^1 (\frac{\partial \boldsymbol{N}}{\partial \tilde{\xi}})^T \frac{\partial \boldsymbol{N}}{\partial \tilde{\xi}} \, d\tilde{\xi} \tag{2.46}$$

2.3.4 Verification of the centrifugal force

2.3.4.1 Rotating cantilever beam

Verification of the centrifugal force $\boldsymbol{F}_\Omega$ part of the equations of motion in the rotating frame will be done by considering a clamped-free beam in rotation as described by Figure 2.7.

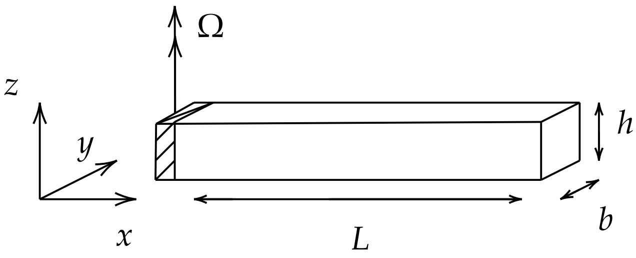

Figure 2.7: Schematic representation of the beam.

Parameters	Value	Units
Young modulus E	210	GPa
Poisson ratio ν	0.3	-
Density ρ	7800	kg/m^3
Height h	0.05	m
Width b	0.05	m
Length L	5.7	m
Rotation speed Ω	200	rad/s

Table 2.3: Material properties and section geometry.

For such a simple problem there exist an analytical solution (EDF, 2011[15]) for the axial deformation U_x at the element level reading

$$\frac{\partial U_x}{\partial x^2} + \frac{\rho}{E}\Omega^2 x = 0 \text{ with } U_x(0) = 0 \text{ and } \frac{\partial U_x}{\partial x}(L) = 0. \tag{2.47}$$

Integration of the differential equation along with the boundary conditions yields

$$U_x(x) = \frac{\rho\Omega^2}{2E}(xL^2 - \frac{x^3}{3}) \tag{2.48}$$

in the local frame of the clamped beam. This analytical solution will be compared to the results of the resolution of the static problem

$$\boldsymbol{Kq} = \boldsymbol{F}_\Omega \tag{2.49}$$

from the developed finite element implementation. Figure 2.8 confirms that the finite element implementation of the centrifugal force was done correctly as the results correspond almost perfectly to the analytical solution.

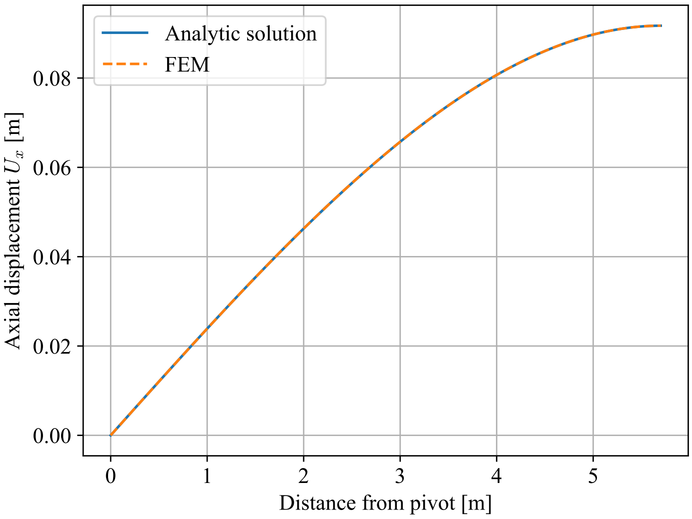

Figure 2.8: Axial displacement U_x for different distances from pivot on the clamped-free rotating beam. The analytical solution and FE solution are compared

2.3.5 Verification of the Campbell diagram

2.3.5.1 Generalized eigensolutions determination procedure

Let's consider the most complete equations of motion investigated in this thesis, i.e of a structure subjected to aerodynamic loads in a rotating frame

$$\boldsymbol{M\ddot{q}} + (\boldsymbol{G} + \boldsymbol{C})\boldsymbol{\dot{q}} + (\boldsymbol{K} + \boldsymbol{K}_\Omega + \boldsymbol{K}_g)\boldsymbol{q} = \boldsymbol{F}_{aero}(\boldsymbol{\ddot{q}}, \boldsymbol{\dot{q}}, \boldsymbol{q}) + \boldsymbol{F}_{ext}, \tag{2.50}$$

note that the aerodynamic forces $\boldsymbol{F}_{aero}$ have an explicit dependence to the generalized coordinates and their time derivatives due to the very nature of fluid-structure interactions.

In the following, $\boldsymbol{F}_{ext}$ will be conveniently put to zero as it doesn't influence the eigensolutions of the problem. As for the aerodynamical loads they shall be expressed as a matrix form to obtain the equivalent free response problem reading

$$\tilde{\boldsymbol{M}}\ddot{\boldsymbol{q}} + \tilde{\boldsymbol{C}}\dot{\boldsymbol{q}} + \tilde{\boldsymbol{K}}\boldsymbol{q} = \boldsymbol{0}. \tag{2.51}$$

Such problems can easily be rewritten by letting a state space vector $\boldsymbol{z} = \begin{bmatrix}\boldsymbol{q}\\ \dot{\boldsymbol{q}}\end{bmatrix}$, allowing to form a convenient state-space formulation of the problem reading

$$\dot{\boldsymbol{z}} = \begin{bmatrix}\dot{\boldsymbol{q}}\\ \ddot{\boldsymbol{q}}\end{bmatrix} = \begin{bmatrix}\boldsymbol{0} & \boldsymbol{I}\\ -\tilde{\boldsymbol{M}}^{-1}\tilde{\boldsymbol{K}} & -\tilde{\boldsymbol{M}}^{-1}\tilde{\boldsymbol{C}}\end{bmatrix}\begin{bmatrix}\boldsymbol{q}\\ \dot{\boldsymbol{q}}\end{bmatrix} = \boldsymbol{A}\boldsymbol{z}, \tag{2.52}$$

admitting an analytical solution in the form of a modal expansion of response such that

$$\boldsymbol{z}(t) = e^{\boldsymbol{A}t}\boldsymbol{z}(0) = \sum_{i=0}^{2n}\boldsymbol{X}_i e^{\lambda_i t}\boldsymbol{c_i}, \tag{2.53}$$

where $\boldsymbol{X}_i$ and λ_i are the associated eigenvectors and values of $\boldsymbol{A}$, c_i a modal constant and n the size of the original equations of motion. Eigenvalues of $\boldsymbol{A}$ are of the form

$$\lambda_i = \xi_i\omega_i \pm j\omega_i\sqrt{1-\xi_i^2}, \tag{2.54}$$

allowing the extraction of the eigenfrequencies ω_i as well as the modal damping ratios ξ_i. This process can be done at each rotating speed Ω considered to construct the Campbell diagram of the structure.

2.3.5.2 Verification with the Campbell diagram

Previously the implementation of the equations of motion of the stator part of the structure was verified and proved to have been well implemented. Once again a commercial software will be used but this time to verify the implementation of the equations of motion of the rotor. In particular the Campbell diagram of the pined-pined bladed rotor depicted in figure 2.9 will be computed using the Python implementation and results will be compared to those of the *Rotordynamics* module of *Siemens NX*.

Parameters	Value	Units
Young modulus E	200	GPa
Poisson ratio ν	0.3	-
Density ρ	7850	kg/m^3
Height h	0.1	m
Width b	0.08	m
Shaft Length L_s	1	m
Blade Length L_b	2	m

Table 2.4: Material properties and section geometry.

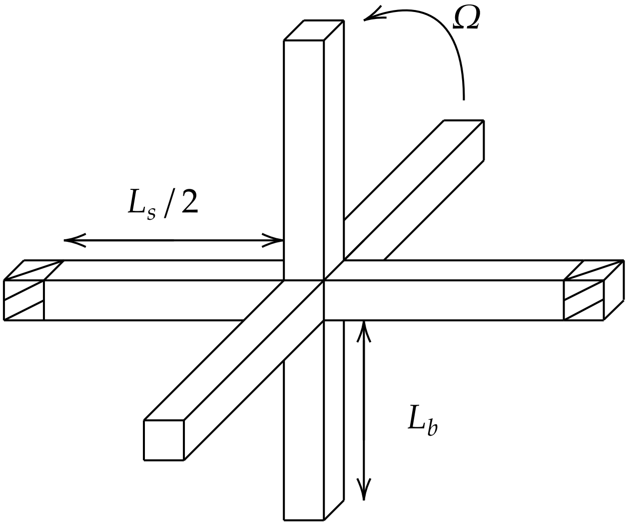

Figure 2.9: Schematic representation of the rotor.

Figure 2.10 shows excellent agreement between the Python implementation and the commercial software. The computation of some modes of *NX* sometimes stopped before the maximum rotation speed Ω if the mode became unstable which is a particularity of the solver used by *NX*. In conclusion, these results assures that the rotating part of the equations of motion has been well implemented.

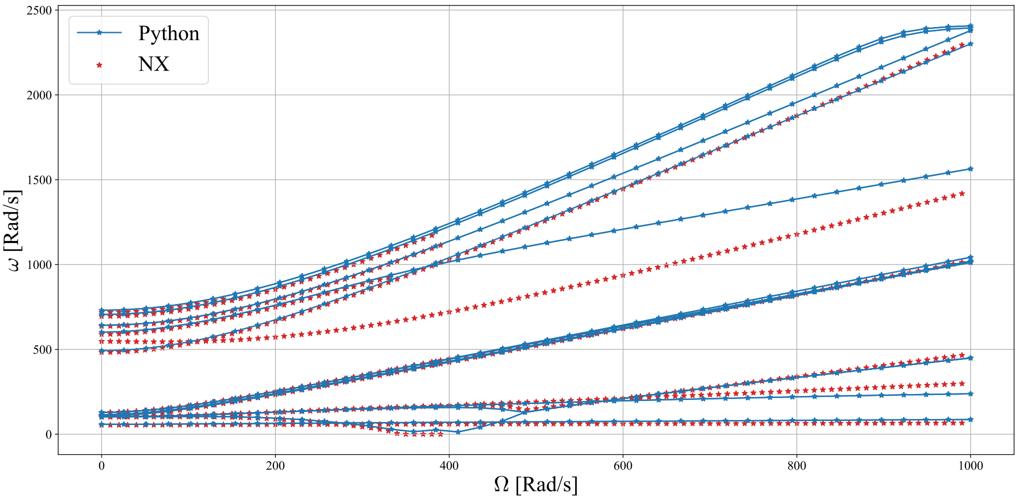

Figure 2.10: Campbell diagram of the pined-pined 4-bladed rotor. Results from Python are compared to those from the Rotordynamics module of *NX*, both results being expressed in the rotating frame. For both computations no structural damping was considered. Mode tracking was done using a *MAC* criterion.

Chapter 3

Stator-Rotor coupling

The structure admits stationary parts whose equations of motion are written in a fixed frame and rotating parts whose dynamic is described in a rotating frame of reference. The two previous chapter described how to construct the equations, this chapter aims at describing how they can be coupled together.

To do so the equations of motion of rotating particle will be established in a simplified case suited for the finite element approach. These equations will be adapted for 3D Bernoulli-Euler beam elements. The coupling sub matrices will then finally be derived yielding to the establishment of a coupling algorithm.

3.1 Description of a rotating particle in an inertial frame

3.1.1 Inertial description of rotating frame quantities

Consider a structure that is an assembly of rotating and stationary parts. Let a particle P placed on a rotating part of the structure whose position is therefore described in a non inertial rotating frame of reference x, y, z as described in Fig 3.1. It is desired to be able to express the position of P through an inertial frame of reference $\bar{x}, \bar{y}, \bar{z}$.

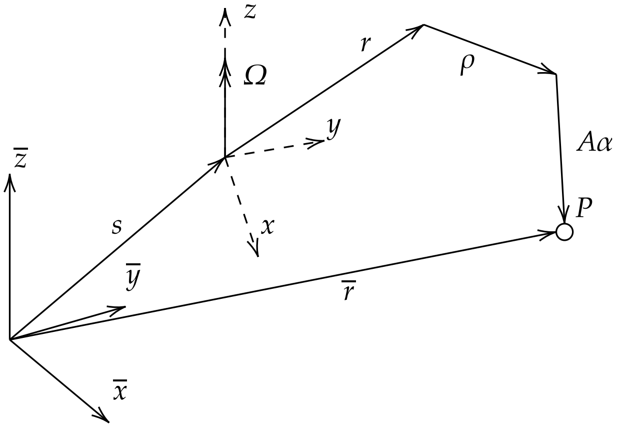

Figure 3.1: Description of a particle P from a rotating frame x, y, z and a fixed inertial frame $\bar{x}, \bar{y}, \bar{z}$. (Adapted from Vollan & Komzsik (2012,[34])).

As it is extremely often the case in the context of turbomachinery applications it will be assumed that the rotation speed vector is essentially along one axis of rotation. Under this assumption the rotation speed vector $\mathbf{\Omega}$ is of the form

$$\mathbf{\Omega} = \Omega z, \tag{3.1}$$

meaning that between the fixed and rotating frame there exist a link expressed such as

$$\begin{cases} \bar{x} = cos(\Omega t)x - sin(\Omega t)y \\ \bar{y} = sin(\Omega t)x + cos(\Omega t)y \\ \bar{z} = z. \end{cases} \tag{3.2}$$

Hereby, the transformation or rotation matrix

$$\boldsymbol{H} = \begin{bmatrix} cos(\Omega t) & -sin(\Omega t) & 0 \\ sin(\Omega t) & cos(\Omega t) & 0 \\ 0 & 0 & 1 \end{bmatrix} \tag{3.3}$$

links the rotating and fixed frame of reference. Moreover, in industrial applications the rotating frame fixed on the rotating part of the structure could a priori undergo small rotations that are not due to the rotation speed Ω. These rotations would be due to the nodal translations of the stationary structure that end up influencing the rotation structure. These additional rotations of the rotating frame are taken into account by yet another transformation matrix

$$\boldsymbol{B} = \begin{bmatrix} 0 & -\bar{\theta} & \bar{\psi} \\ \bar{\theta} & 0 & -\bar{\varphi} \\ -\bar{\psi} & \bar{\varphi} & 0 \end{bmatrix}. \tag{3.4}$$

In the rotating frame is described the initial position of the particle $\boldsymbol{r}$ as well as its displacement due to translation $\boldsymbol{\rho}$, and rotation $\boldsymbol{A\alpha}$. This means that in the rotating frame the position of the particle is described by $\boldsymbol{r} + \boldsymbol{\rho} + \boldsymbol{A\alpha}$.

Now in the fixed inertial frame these quantities are expressed through the rotation matrices $\boldsymbol{H}$ and $\boldsymbol{B}$. Neglecting quadratic terms in terms of nodal displacements finally yields to the description of the position of the particle P in the inertial frame reading

$$\bar{\boldsymbol{r}} = \boldsymbol{s} + \boldsymbol{BHr} + \boldsymbol{H\rho} + \boldsymbol{HA\alpha} + \boldsymbol{Hr}. \tag{3.5}$$

The term $\boldsymbol{BHr}$ can be conveniently rewritten as[34]

$$\begin{aligned} \boldsymbol{BHr} &= \begin{bmatrix} 0 & -\bar{\theta} & \bar{\psi} \\ \bar{\theta} & 0 & -\bar{\varphi} \\ -\bar{\psi} & \bar{\varphi} & 0 \end{bmatrix} \begin{bmatrix} \cos\Omega t & -\sin\Omega t & 0 \\ \sin\Omega t & \cos\Omega t & 0 \\ 0 & 0 & 1 \end{bmatrix} \begin{bmatrix} x \\ y \\ z \end{bmatrix} \\ &= \begin{bmatrix} 0 & -\bar{\theta} & \bar{\psi} \\ \bar{\theta} & 0 & -\bar{\varphi} \\ -\bar{\psi} & \bar{\varphi} & 0 \end{bmatrix} \begin{bmatrix} x\cos\Omega t + y\sin\Omega t \\ x\sin\Omega t + y\cos\Omega t \\ z \end{bmatrix} \\ &= \begin{bmatrix} 0 & 0 & -x\sin\Omega t - y\cos\Omega t \\ 0 & 0 & x\cos\Omega t - y\sin\Omega t \\ x\sin\Omega t + y\cos\Omega t & -x\cos\Omega t + y\sin\Omega t & 0 \end{bmatrix} \begin{bmatrix} \bar{\varphi} \\ \bar{\psi} \\ \bar{\theta} \end{bmatrix} \\ &= \boldsymbol{B}_0\boldsymbol{\beta}. \end{aligned} \tag{3.6}$$

Finally the problem is conveniently rewritten as

$$\bar{\boldsymbol{r}} = \boldsymbol{Mg} \tag{3.7}$$

with $\boldsymbol{M} = \begin{bmatrix}\boldsymbol{I} & \boldsymbol{B}_0 & \boldsymbol{H} & \boldsymbol{HA} & \boldsymbol{H}\end{bmatrix}$ being the governing matrix and $\boldsymbol{g} = \begin{bmatrix}\boldsymbol{s} & \boldsymbol{\beta} & \boldsymbol{\rho} & \boldsymbol{\alpha} & \boldsymbol{r}\end{bmatrix}^T$ the augmented generalized coordinates. This reformulation highlights the fact that this can be seen as a time-dependent change of variable from the displacements in the fixed frame of reference $\bar{\boldsymbol{r}}$ and those of a rotating particle $\boldsymbol{g}$.

3.1.2 Matrix formulation of Lagrange's equations

For a single particle described in the fixed frame the kinetic energy reads

$$T = \frac{1}{2}m\dot{\bar{\boldsymbol{r}}}^T\dot{\bar{\boldsymbol{r}}}, \tag{3.8}$$

using the previous time dependent change of variable $\bar{\boldsymbol{r}} = \boldsymbol{Mg}$ yields to

$$\begin{aligned} T &= \frac{1}{2}m[(\boldsymbol{g}^T\dot{\boldsymbol{M}}^T + \dot{\boldsymbol{g}}^T\boldsymbol{M}^T)(\dot{\boldsymbol{M}}\boldsymbol{g} + \boldsymbol{M}\dot{\boldsymbol{g}})] \\ &= \frac{1}{2}m[\boldsymbol{g}^T\dot{\boldsymbol{M}}^T\dot{\boldsymbol{M}}\boldsymbol{g} + \boldsymbol{g}^T\dot{\boldsymbol{M}}^T\boldsymbol{M}\dot{\boldsymbol{g}} + \dot{\boldsymbol{g}}^T\boldsymbol{M}^T\dot{\boldsymbol{M}}\boldsymbol{g} + \dot{\boldsymbol{g}}^T\boldsymbol{M}^T\boldsymbol{M}\dot{\boldsymbol{g}}] \\ &= \frac{1}{2}m[\boldsymbol{g}^T\dot{\boldsymbol{M}}^T\dot{\boldsymbol{M}}\boldsymbol{g} + 2\boldsymbol{g}^T\dot{\boldsymbol{M}}^T\boldsymbol{M}\dot{\boldsymbol{g}} + \dot{\boldsymbol{g}}^T\boldsymbol{M}^T\boldsymbol{M}\dot{\boldsymbol{g}}]. \end{aligned} \tag{3.9}$$

Recalling the Lagrange principle as it was described in section 2.3.1.3 but applied for single a particle and only in terms of kinematics ($V = D = Q_D = 0$)

$$-\frac{d}{dt}\left(\frac{\partial T}{\partial \dot{\boldsymbol{g}}}\right) + \frac{\partial T}{\partial t} = \boldsymbol{Q_E}, \tag{3.10}$$

applied in the developed expression of the kinetic energy T reads

$$m(\boldsymbol{M}^T\boldsymbol{M})\ddot{\boldsymbol{g}} + 2m(\boldsymbol{M}^T\dot{\boldsymbol{M}})\dot{\boldsymbol{g}} + (\boldsymbol{M}^T\ddot{\boldsymbol{M}})\boldsymbol{g} = \boldsymbol{Q_E}, \tag{3.11}$$

finally giving an expression of the equations of motion linking the displacement in the fixed frame with the augmented generalized coordinates of a rotating particle $\boldsymbol{g}$.

3.2 Finite elements formulation

3.2.1 Application to Euler-Bernoulli 3D beam elements

The procedure described in all generality in section 3.1 will be adapted for a finite element formulation of the problem, in particular for application of Euler-Bernoulli 3D beam elements. As described above, in all generalities the generalized coordinates vector reads

$$\boldsymbol{g} = \begin{bmatrix}\boldsymbol{s} & \boldsymbol{\beta} & \boldsymbol{\rho} & \boldsymbol{\alpha} & \boldsymbol{r}\end{bmatrix}^T. \tag{3.12}$$

It will be reduced by only keeping useful quantities. First, the initial position of the particle from the origin of the rotating frame, $\boldsymbol{r}$ doesn't change with time such that it can be disregarded. Then, since 3D Bernoulli-Euler beam elements are used node displacement, as seen from their structural frame is expressed only using a translation $\boldsymbol{\rho}$ but is obtained by translating the translation and rotations of the beam element through the shape-functions of the 3D beam elements. There is, therefore no reasons to keep the $\boldsymbol{A\alpha}$ as it is redundant. $\boldsymbol{g}$ is thereby reduced to

$$\boldsymbol{g} = \begin{bmatrix}\boldsymbol{s} & \boldsymbol{\beta} & \boldsymbol{\rho}\end{bmatrix}^T, \tag{3.13}$$

This allows a corresponding reduction of the governing matrix $\boldsymbol{M}$ such that

$$\boldsymbol{M} = \begin{bmatrix}\boldsymbol{I} & \boldsymbol{B}_0 & \boldsymbol{H}\end{bmatrix}, \tag{3.14}$$

Finally, using the equation 3.11 gives the equation of motion of a rotating particle of mass m as described from a fixed frame of reference

$$\begin{gathered} m\begin{bmatrix}\mathbf{I} & \mathbf{B}_0 & \mathbf{H}\\ \mathbf{B}_0^T & \mathbf{B}_0^T\mathbf{B}_0 & \mathbf{B}_0^T\mathbf{H}\\ \mathbf{H}^T & \mathbf{H}^T\mathbf{B}_0 & \mathbf{I}\end{bmatrix}\begin{Bmatrix}\ddot{\boldsymbol{s}}\\ \ddot{\boldsymbol{\beta}}\\ \ddot{\boldsymbol{\rho}}\end{Bmatrix} + 2m\Omega\begin{bmatrix}0 & \bar{\mathbf{B}}_0 & \bar{\mathbf{H}}\\ 0 & \mathbf{B}_0^T\bar{\mathbf{B}}_0 & \mathbf{B}_0^T\bar{\mathbf{H}}\\ 0 & \mathbf{H}^T\bar{\mathbf{B}}_0 & \mathbf{H}^T\bar{\mathbf{H}}\end{bmatrix}\begin{Bmatrix}\dot{\boldsymbol{s}}\\ \dot{\boldsymbol{\beta}}\\ \dot{\boldsymbol{\rho}}\end{Bmatrix} \\ +m\Omega^2\begin{bmatrix}0 & \bar{\bar{\mathbf{B}}}_0 & \bar{\bar{\mathbf{H}}}\\ 0 & \mathbf{B}_0^T\bar{\bar{\mathbf{B}}}_0 & \mathbf{B}_0^T\bar{\bar{\mathbf{H}}}\\ 0 & \mathbf{H}^T\bar{\bar{\mathbf{B}}}_0 & \mathbf{H}^T\bar{\bar{\mathbf{H}}}\end{bmatrix}\begin{Bmatrix}\boldsymbol{s}\\ \boldsymbol{\beta}\\ \boldsymbol{\rho}\end{Bmatrix} = \boldsymbol{Q_E} = \Omega^2\begin{bmatrix}-m\bar{\bar{\mathbf{H}}}\boldsymbol{r}\\ -m\mathbf{B_0}^T\bar{\bar{\mathbf{H}}}\boldsymbol{r}\\ \mathbf{f}_{cp}\end{bmatrix}. \end{gathered} \tag{3.15}$$

These equations cannot be used directly as they are not in finite element formulation. They still however provide the links between translational and rotational degrees of freedom of the hub in the static frame respectively $\boldsymbol{s}, \boldsymbol{\beta}$ as well as their time derivatives and the node degrees of freedom in the rotating frame $\boldsymbol{\rho}$ and its time derivatives. Exterior loads $\boldsymbol{Q_E}$ applied to the particle are also taken into account in particular the centrifugal force $\boldsymbol{f}_{cp}$ applied in the rotating frame as well as the Coriolis force $-m\mathbf{B_0}^T\bar{\bar{\mathbf{H}}}\boldsymbol{r}$ and the unbalance force $-m\bar{\bar{\mathbf{H}}}\boldsymbol{r}$ in the static frame.

3.2.2 Determination of the coupling blocks

The previous equations of motion are only for a rotating particle. Using those will provide the foundation of the finite element formulation of the problem. In this section the governing matrix $\boldsymbol{M}$ will be renamed $\boldsymbol{M^*}$ to avoid confusion with the mass matrix $\boldsymbol{M}$.

Let first a recall of the kinetic energy of the rotating particle

$$\begin{aligned} T &= \frac{1}{2} m \dot{\bar{\boldsymbol{r}}}^T \dot{\bar{\boldsymbol{r}}}, \text{ with } \bar{\boldsymbol{r}} = \boldsymbol{M}^* \boldsymbol{g} \\ &= \frac{1}{2} m [\boldsymbol{g}^T \dot{\boldsymbol{M}}^{*T} \dot{\boldsymbol{M}}^* \boldsymbol{g} + 2 \boldsymbol{g}^T \dot{\boldsymbol{M}}^{*T} \boldsymbol{M}^* \dot{\boldsymbol{g}} + \dot{\boldsymbol{g}}^T \boldsymbol{M}^{*T} \boldsymbol{M}^* \dot{\boldsymbol{g}}], \end{aligned} \tag{3.16}$$

rewritten in the integral form

$$T = \int_V \rho [\boldsymbol{g}^T \dot{\boldsymbol{M}}^{*T} \dot{\boldsymbol{M}}^* \boldsymbol{g} + 2 \boldsymbol{g}^T \dot{\boldsymbol{M}}^{*T} \boldsymbol{M}^* \dot{\boldsymbol{g}} + \dot{\boldsymbol{g}}^T \boldsymbol{M}^{*T} \boldsymbol{M}^* \dot{\boldsymbol{g}}] dV. \tag{3.17}$$

Now consider a change of variable to express the displacement fields $\boldsymbol{s}$,$\boldsymbol{\beta}$,$\boldsymbol{\rho}$ contained in $\boldsymbol{g}$ from the degrees of freedom of Bernoulli 3D beam elements

$$\boldsymbol{g} = \tilde{\boldsymbol{N}} \tilde{\boldsymbol{q}} = \begin{bmatrix} \boldsymbol{N} & \boldsymbol{0} & \boldsymbol{0} \\ \boldsymbol{0} & \boldsymbol{N} & \boldsymbol{0} \\ \boldsymbol{0} & \boldsymbol{0} & \boldsymbol{N} \end{bmatrix} \begin{bmatrix} \boldsymbol{q_s} \\ \boldsymbol{q_\beta} \\ \boldsymbol{q_\rho} \end{bmatrix}, \tag{3.18}$$

where $\boldsymbol{N}$ are the shape functions of Bernoulli 3D beam elements. Inserting this change of variable into the integral form of the kinetic energy yields

$$\begin{aligned} T =& \frac{1}{2} \int_V \rho \tilde{\boldsymbol{q}}^T \tilde{\boldsymbol{N}}^T \dot{\boldsymbol{M}}^{*T} \dot{\boldsymbol{M}}^* \tilde{\boldsymbol{N}} \tilde{\boldsymbol{q}} \ dV + \\ & \frac{1}{2} \int_V 2 \rho \tilde{\boldsymbol{q}}^T \tilde{\boldsymbol{N}}^T \dot{\boldsymbol{M}}^{*T} \boldsymbol{M}^* \tilde{\boldsymbol{N}} \dot{\tilde{\boldsymbol{q}}} \ dV + \\ & \frac{1}{2} \int_V \rho \dot{\tilde{\boldsymbol{q}}}^T \tilde{\boldsymbol{N}}^T \boldsymbol{M}^{*T} \boldsymbol{M}^* \tilde{\boldsymbol{N}} \dot{\tilde{\boldsymbol{q}}} \ dV. \end{aligned} \tag{3.19}$$

The first term couples the centrifugal softening $\boldsymbol{K}_\Omega$, the second term couples the gyroscopic effects $\boldsymbol{G}$ and finally the third term couples the mass matrix $\boldsymbol{M}$. This shows that no coupling is made on $\boldsymbol{C}$ nor on $\boldsymbol{K}$ as only the kinematic of the rotating particle were considered.

Focusing on the mass matrix term yields

$$\frac{1}{2} \dot{\tilde{\boldsymbol{q}}}^T \left(\int_V \rho \tilde{\boldsymbol{N}}^T \boldsymbol{M}^{*T} \boldsymbol{M}^* \tilde{\boldsymbol{N}} dV \right) \dot{\tilde{\boldsymbol{q}}}, \tag{3.20}$$

with

$$\boldsymbol{M}_{coupling} = \int_V \rho \tilde{\boldsymbol{N}}^T \boldsymbol{M}^{*T} \boldsymbol{M}^* \tilde{\boldsymbol{N}} dV \tag{3.21}$$

defining the coupling matrix in terms of mass. This matrix is 36x36 as $\boldsymbol{g}$ is 9x1 and $\tilde{\boldsymbol{N}}$ is 9x36. Expressing $\tilde{\boldsymbol{N}}$ is at was defined in eq 3.18 yields

$$\boldsymbol{M}_{coupling} = \int_V \rho \begin{bmatrix} \boldsymbol{N}^T & \boldsymbol{0} & \boldsymbol{0} \\ \boldsymbol{0} & \boldsymbol{N}^T & \boldsymbol{0} \\ \boldsymbol{0} & \boldsymbol{0} & \boldsymbol{N}^T \end{bmatrix} \begin{bmatrix} \boldsymbol{I} & \boldsymbol{B_0} & \boldsymbol{H} \\ \boldsymbol{B_0^T} & \boldsymbol{B_0^T B_0} & \boldsymbol{B_0^T H} \\ \boldsymbol{H}^T & \boldsymbol{H}^T \boldsymbol{B_0} & \boldsymbol{I} \end{bmatrix} \begin{bmatrix} \boldsymbol{N} & \boldsymbol{0} & \boldsymbol{0} \\ \boldsymbol{0} & \boldsymbol{N} & \boldsymbol{0} \\ \boldsymbol{0} & \boldsymbol{0} & \boldsymbol{N} \end{bmatrix} dV. \tag{3.22}$$

Finally allowing the computation of the different 12x12 coupling blocks

$$\boldsymbol{M}_{coupling} = \int_V \rho \begin{bmatrix} \boldsymbol{N}^T \boldsymbol{I} \boldsymbol{N} & \boldsymbol{N}^T \boldsymbol{B_0} \boldsymbol{N} & \boldsymbol{N}^T \boldsymbol{H} \boldsymbol{N} \\ \boldsymbol{N}^T \boldsymbol{B_0^T} \boldsymbol{N} & \boldsymbol{N}^T \boldsymbol{B_0^T} \boldsymbol{B_0} \boldsymbol{N} & \boldsymbol{N}^T \boldsymbol{B_0^T} \boldsymbol{H} \boldsymbol{N} \\ \boldsymbol{N}^T \boldsymbol{H}^T \boldsymbol{N} & \boldsymbol{N}^T \boldsymbol{H}^T \boldsymbol{B_0} \boldsymbol{N} & \boldsymbol{N}^T \boldsymbol{I} \boldsymbol{N} \end{bmatrix} = \begin{bmatrix} \boldsymbol{M}_{\ddot{s},\ddot{s}} & \boldsymbol{M}_{\ddot{s},\ddot{\beta}} & \boldsymbol{M}_{\ddot{s},\ddot{\rho}} \\ \boldsymbol{M}_{\ddot{\beta},\ddot{s}} & \boldsymbol{M}_{\ddot{\beta},\ddot{\beta}} & \boldsymbol{M}_{\ddot{\beta},\ddot{\rho}} \\ \boldsymbol{M}_{\ddot{\rho},\ddot{s}} & \boldsymbol{M}_{\ddot{\rho},\ddot{\beta}} & \boldsymbol{M}_{\ddot{\rho},\ddot{\rho}} \end{bmatrix}. \tag{3.23}$$

Those coupling blocks assures that the degrees of freedom $\boldsymbol{q}_s$ $\boldsymbol{q}_\rho$, $\boldsymbol{q}_\beta$ are coupled together two by twos. Derivation of the coupling blocks of $\boldsymbol{G}_{coupling}$ and $\boldsymbol{K}_{\Omega,coupling}$ is done in the exact same fashion yielding

$$\boldsymbol{G}_{coupling} = \int_V \rho \Omega \begin{bmatrix} \boldsymbol{0} & \boldsymbol{N}^T \bar{\boldsymbol{B}}_{\boldsymbol{0}} \boldsymbol{N} & \boldsymbol{N}^T \bar{\boldsymbol{H}} \boldsymbol{N} \\ \boldsymbol{0} & \boldsymbol{N}^T \boldsymbol{B_0^T} \bar{\boldsymbol{B}}_{\boldsymbol{0}} \boldsymbol{N} & \boldsymbol{N}^T \boldsymbol{B_0^T} \bar{\boldsymbol{H}} \boldsymbol{N} \\ \boldsymbol{0} & \boldsymbol{N}^T \boldsymbol{H}^T \bar{\boldsymbol{B}}_{\boldsymbol{0}} \boldsymbol{N} & \boldsymbol{N}^T \boldsymbol{H}^T \bar{\boldsymbol{H}} \boldsymbol{N} \end{bmatrix} = \begin{bmatrix} \boldsymbol{G}_{\dot{s},\dot{s}} & \boldsymbol{G}_{\dot{s},\dot{\beta}} & \boldsymbol{G}_{\dot{s},\dot{\rho}} \\ \boldsymbol{G}_{\dot{\beta},\dot{s}} & \boldsymbol{G}_{\dot{\beta},\dot{\beta}} & \boldsymbol{G}_{\dot{\beta},\dot{\rho}} \\ \boldsymbol{G}_{\dot{\rho},\dot{s}} & \boldsymbol{G}_{\dot{\rho},\dot{\beta}} & \boldsymbol{G}_{\dot{\rho},\dot{\rho}} \end{bmatrix}. \tag{3.24}$$

$$\boldsymbol{K}_{\Omega,coupling} = \int_V \rho \Omega^2 \begin{bmatrix} \boldsymbol{0} & \boldsymbol{N}^T \bar{\bar{\boldsymbol{B}}}_{\boldsymbol{0}} \boldsymbol{N} & \boldsymbol{N}^T \bar{\bar{\boldsymbol{H}}} \boldsymbol{N} \\ \boldsymbol{0} & \boldsymbol{N}^T \boldsymbol{B_0^T} \bar{\bar{\boldsymbol{B}}}_{\boldsymbol{0}} \boldsymbol{N} & \boldsymbol{N}^T \boldsymbol{B_0^T} \bar{\bar{\boldsymbol{H}}} \boldsymbol{N} \\ \boldsymbol{0} & \boldsymbol{N}^T \boldsymbol{H}^T \bar{\bar{\boldsymbol{B}}}_{\boldsymbol{0}} \boldsymbol{N} & \boldsymbol{N}^T \boldsymbol{H}^T \bar{\bar{\boldsymbol{H}}} \boldsymbol{N} \end{bmatrix} = \begin{bmatrix} \boldsymbol{K}_{s,s} & \boldsymbol{K}_{s,\beta} & \boldsymbol{K}_{s,\rho} \\ \boldsymbol{K}_{\beta,s} & \boldsymbol{K}_{\beta,\beta} & \boldsymbol{K}_{\beta,\rho} \\ \boldsymbol{K}_{\rho,s} & \boldsymbol{K}_{\rho,\beta} & \boldsymbol{K}_{\rho,\rho} \end{bmatrix}. \tag{3.25}$$

3.2.3 Coupling procedure

In this thesis propeller-wing configurations are considered for whirl-flutter. This means that the only part of the structure that is at the same time part of the rotating and fixed structure is the hub. This is thereby the only nodes where a coupling is required and will construct the link between the rotating and fixed parts. In other words the change of variable between the fixed and rotating frame, applied by the coupling blocks derived previously shall only be done at the hub level (with possibly multiple hubs).

For the sake of simplicity only one hub will be considered in the following figures to display how coupling is done in practice. The *Python* implementation is nevertheless able to handle multiple hubs and the following procedure is easily extendable to multi-propeller applications. The coupling procedure will be detailed for the mass matrix $\boldsymbol{M}$ but remains the exact same with $\boldsymbol{K}_\Omega$ and $\boldsymbol{G}$ only with different coupling blocks.

With only one hub any matrix of the equations of motion of the overall structure take the form given in Fig 3.2.

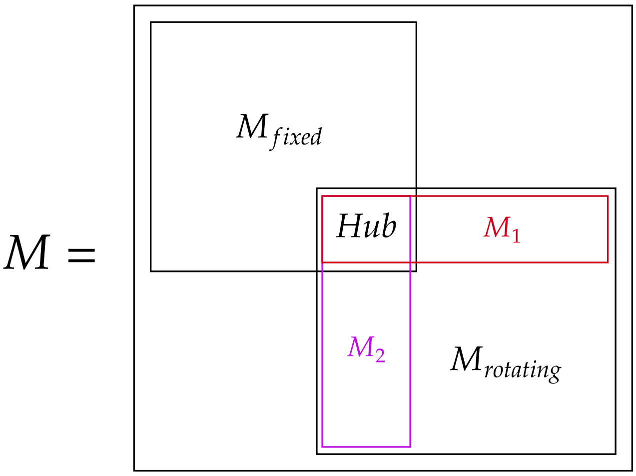

Figure 3.2: Structural matrix of the overall structure $\boldsymbol{M}$ with coupling. $\boldsymbol{M}_{fixed}$ and $\boldsymbol{M}_\Omega$ depict the structural matrices of the stator and rotor parts respectively. Inspired by C. Jacquet (2024,[18]).

A static part given by $\boldsymbol{M}_{fixed}$ and a rotating part depicted by $\boldsymbol{M}_{rotating}$ coexist inside the overall structural matrix $\boldsymbol{M}$. These 2 matrices shall be coupled as otherwise quantities originating from 2 different frames will coexist in the same matrix yielding to inconsistent results. To avoid this coupling matrices, at the hub level, are considered namely $\boldsymbol{M}_1$ and $\boldsymbol{M}_2$. $\boldsymbol{M}_1$ link the quantities of the stator to those of the rotor while $\boldsymbol{M}_2$ link the quantities of the rotor to the stator.

Let that the rotating part of the structure contain n elements, since the hub is a node of an Euler-Bernoulli 3D beam element then $\boldsymbol{M}_1$ is 6 x n while $\boldsymbol{M}_2$ is n x 6 as a translation shall be done for each degree of freedom of the rotating frame. Since the hub is the only common node between the static and rotating part no further translation is necessary.

The 3 first lines of $\boldsymbol{M}_1$ couple the translational degrees of freedom from the hub to the rotating structure; in other words the translational degrees of freedom of $\boldsymbol{q}_s$ to $\boldsymbol{q}_\rho$. The 3 last lines of $\boldsymbol{M}_1$ couple the rotational degrees of freedom from the hub to the translational ones of the rotating structure; in other words the rotational degrees of freedom of $\boldsymbol{q}_\beta$ to $\boldsymbol{q}_\rho$. A representation of $\boldsymbol{M}_1$ is given in Fig 3.3 for the mass matrix $\boldsymbol{M}$

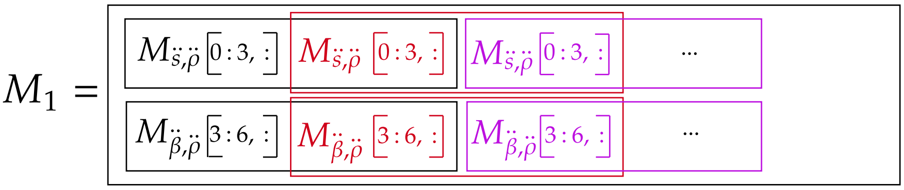

Figure 3.3: Schematic representation of $\boldsymbol{M}_1$ linking the hub degrees of freedom $\boldsymbol{q}_s$ or $\boldsymbol{q}_\beta$ to the rotating degrees of freedom $\boldsymbol{q}_\rho$. Each color represents a given element

As for the computation of $\boldsymbol{M}_2$ it is done in the same fashion with its first 3 columns and 3 last columns respectively linking the degrees of freedom from the rotating structure to the translational or rotational ones of the hub. A representation of $\boldsymbol{M}_2$ is given in Fig 3.2 for the mass matrix M

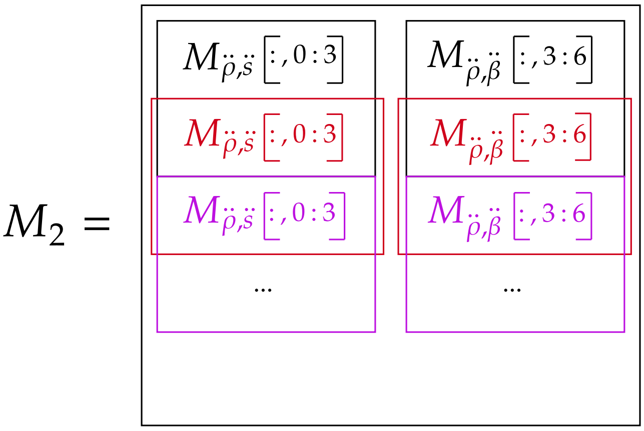

Figure 3.4: Schematic representation of $\boldsymbol{M}_2$ linking the rotating degrees of freedom $\boldsymbol{q}_\rho$ to the hub translational and rotational degrees of freedom. Each color represents a given element.

Naturally, the coupling blocks are computed at the element level and shall be put back at the structural level before assembly.

3.2.4 Coupled equations of motion

As shown in Section 3.2.2 the coupling matrices have an explicit time dependence through the time dependent matrices $\boldsymbol{H}$ and $\boldsymbol{B}_0$. Since coupling is only done on $\boldsymbol{M}$, $\boldsymbol{G}$ and $\boldsymbol{K}_{\boldsymbol{\Omega}}$ the coupled equations of motion are of the form

$$\boldsymbol{M}(t)\ddot{\boldsymbol{q}} + (\boldsymbol{C} + \boldsymbol{G}(t))\dot{\boldsymbol{q}} + (\boldsymbol{K} + \boldsymbol{K}_\Omega(t) + \boldsymbol{K}_g)\boldsymbol{q} = \boldsymbol{F}_\Omega \tag{3.26}$$

Chapter 4

Stability analysis

The 2 previous chapter described how one could obtain and couple the equations of motion for the rotor and the stator. The goal of this chapter will now to investigate the stability of the problem. At this aim, this chapter will first describe how to stability of time periodic system can be assessed using Floquet analysis. Then, an academic simple wing-propeller setup with different tweak-able parameters will be presented. After, the numerical implications of integrating the academic wing-propeller setup will be discussed leading to the choice of the appropriate numerical integration scheme. Finally, the stability of the problem will be assessed and discussed as a function of the different parameters such that the rotation speed, pylon stiffness and wing flexibility.

4.1 Stability of linear-time-variant systems (Floquet analysis)

4.1.1 State-transition matrix

Let a time-dependent space-state representation of a linear system

$$\dot{\boldsymbol{x}}(t) = \boldsymbol{A}(t)\boldsymbol{x}(t) + \boldsymbol{B}(t)\boldsymbol{u}(t). \tag{4.1}$$

Assessing the stability of such systems isn't as straightforward as computing the eigenvalues of $\boldsymbol{A}$ as they are time dependent. Another approach will therefore be investigated.

In the context of control theory it is common to define a *state-transition matrix*(W. Rugh, 1996[25]) $\boldsymbol{\Phi}(t,\tau)$ describing how an initial condition or an input, or in other words a perturbation, propagates to the system state at a given time $\boldsymbol{x}(t)$. Formally written such as

$$\boldsymbol{x}(t) = \boldsymbol{\Phi}(t,\tau)\boldsymbol{x}(\tau) + \int_{\tau}^{t} \boldsymbol{\Phi}(t,\tau)\boldsymbol{B}(t)\boldsymbol{u}(t)d\tau, \tag{4.2}$$

since only the stability is of interest $\boldsymbol{B}(t)$ may conveniently be put to $\mathbf{0}$ reading

$$\boldsymbol{x}(t) = \boldsymbol{\Phi}(t,\tau)\boldsymbol{x}(\tau). \tag{4.3}$$

Let's assume that the system whose stability is assessed is periodic such that

$$\boldsymbol{A}(t+T) = \boldsymbol{A}(t), \tag{4.4}$$

in that case the fundamental matrix solution can be evaluated from the initial conditions to a period T reading $\boldsymbol{\Phi}(0,T)$ and will be renamed the *monodromy matrix*. Physically the monodromy matrix represents how an initial perturbation $\boldsymbol{x}(0)$ propagates to the system state after one period $\boldsymbol{x}(T)$ and will therefore be crucial for the stability assessment of the system.

4.1.2 Floquet representation

Floquet's theorem states that for a fundamental matrix solution $\phi(t)$ of the periodic system $\dot{\boldsymbol{x}}(t) = \boldsymbol{A}(t)\boldsymbol{x}(t)$ of period T, there must exist a periodic of period T and invertible matrix $\boldsymbol{P}(t)$ such that

$$\phi(t) = \boldsymbol{P}(t)e^{\boldsymbol{R}t}, \tag{4.5}$$

depicting its *Floquet representation*(G. Floquet, 1883[16], with $\boldsymbol{R}$ being a complex constant matrix. $\boldsymbol{P}(t)$ is finally used to produce a mapping known as the *Lyapunov transformation*(A. Lyapunov, 1907[11]) reading

$$\boldsymbol{x}(t) = \boldsymbol{P}(t)\boldsymbol{y}(t). \tag{4.6}$$

It can be shown that such a transformation allows to rewrite the system $\dot{\boldsymbol{x}}(t) = \boldsymbol{A}(t)\boldsymbol{x}(t)$ as

$$\dot{\boldsymbol{y}}(t) = \boldsymbol{R}\boldsymbol{y}(t), \tag{4.7}$$

meaning that the stability of $\boldsymbol{y}(t)$ can be assessed through the eigenvalues of the matrices $\boldsymbol{R}$ which is time-invariant. Finally, since $\boldsymbol{P}(t)$ is continuous and periodic it must remain bounded meaning that if $\boldsymbol{y}(t)$ is bounded then $\boldsymbol{x}(t)$ also is. The *monodromy matrix* $\boldsymbol{\Phi}(0, T)$ can be retrieved from the fundamental matrix solution from

$$\begin{aligned}\boldsymbol{\Phi}(\tau, t) =& \phi(\tau)^{-1}\phi(t)\\ \boldsymbol{\Phi}(0, T) =& \phi(0)^{-1}\phi(T)\\ =& \boldsymbol{P}^{-1}(0)\boldsymbol{P}(T)e^{\boldsymbol{R}T}\\ =& e^{\boldsymbol{R}T},\end{aligned} \tag{4.8}$$

recalling the physical interpretation of the monodromy matrix stated above, it further shows that the eigenvalues of $\boldsymbol{R}$ are crucial for stability assessment. Diagonalizing $\boldsymbol{R}$ using its complex eigenvalues α_i allows directly diagonalize $e^{\boldsymbol{R}T}$ to simply express the monodromy matrix as

$$\boldsymbol{\Phi}(0, T) = Diag(e^{\alpha_0 T}, e^{\alpha_1 T}, ..., e^{\alpha_l T}), \tag{4.9}$$

meaning that if there exist any complex eigenvalue α_k of R whose real part is strictly positive then the system is unstable as the initial perturbation has been amplified after one period T. The eigenvalues of the monodromy matrix, $e^{\alpha_i T}$ are called the *Floquet multipliers* or *Characteristic multipliers* while the eigenvalues of $\boldsymbol{R}$, α_i are called the *Floquet exponents*

4.1.3 Computation of the state-transition matrix

The state-transition matrix is constructed by evaluating how any element of the complete basis of the problem evolve over time through $\dot{\boldsymbol{x}}(t) = \boldsymbol{A}(t)\boldsymbol{x}(t)$. In other words,

$$\boldsymbol{\Phi}(0, t) = \begin{bmatrix}\boldsymbol{X}_1(t) & \cdots & \boldsymbol{X}_n(t)\end{bmatrix} \tag{4.10}$$

where $\boldsymbol{X}_i(t)$ is the state of the system at time t with $\boldsymbol{X}_i(0) = \boldsymbol{e_i} = \begin{bmatrix}0 & \cdots & 1 & \cdots & 0\end{bmatrix}^T$ as an initial condition. Such a procedure is easily applied to the monodromy matrix simply with $t = T$ yielding to the computation of $\boldsymbol{\Phi}(0, T)$ whose eigenvalues, the *Floquet multipliers*, γ_i directly give the *Floquet exponents* through

$$\alpha_i = \frac{\ln(\gamma_i)}{T}. \tag{4.11}$$

There exist some analytical formulation of the state-transition matrix in the form of the *Peano-Baker* series, which can be seen as a *Magnus-expansion* of the problem $\dot{\boldsymbol{x}}(t) = \boldsymbol{A}(t)\boldsymbol{x}(t)$:

$$\begin{aligned}\Phi(t, 0) &= \mathbf{I} + \int_0^t \mathbf{A}(\sigma_1)\, d\sigma_1\\ &+ \int_0^t \mathbf{A}(\sigma_1) \int_0^{\sigma_1} \mathbf{A}(\sigma_2)\, d\sigma_2\, d\sigma_1\\ &+ \int_0^t \mathbf{A}(\sigma_1) \int_0^{\sigma_1} \mathbf{A}(\sigma_2) \int_0^{\sigma_2} \mathbf{A}(\sigma_3)\, d\sigma_3\, d\sigma_2\, d\sigma_1\\ &+ \cdots\\ &= \mathcal{T}\left(e^{\int_0^t \mathbf{A}(\sigma)\, d\sigma}\right),\end{aligned} \tag{4.12}$$

where $\mathcal{T}$ is the time-ordering operator that ensures than the nested integrals are done in the right order since A(t) a priori isn't commuting at all times. Evaluation of such integrals remains a useful analytical tool but won't be used to compute the monodromy matrix in practice due to their high computational costs.

4.1.4 Time coupling periodicity of the problem

4.1.4.1 State-space formulation

Due to the time-dependent nature of the coupling coefficients the equations of motion of the coupled system are of the form

$$\boldsymbol{M}(t)\ddot{\boldsymbol{q}} + (\boldsymbol{C} + \boldsymbol{G}(t))\dot{\boldsymbol{q}} + (\boldsymbol{K} + \boldsymbol{K}_\Omega(t) + \boldsymbol{K}_g)\boldsymbol{q} = \boldsymbol{F}_\Omega, \tag{4.13}$$

easily rewritten as an autonomous state-space formulation by letting a state-space vector $\boldsymbol{x} = \begin{bmatrix}\boldsymbol{q}\\ \dot{\boldsymbol{q}}\end{bmatrix}$ such that

$$\begin{aligned}\dot{\boldsymbol{x}}(t) &= \begin{bmatrix}\dot{\boldsymbol{q}}\\ \ddot{\boldsymbol{q}}\end{bmatrix} = \begin{bmatrix}\boldsymbol{0} & \boldsymbol{I}\\ -\boldsymbol{M}^{-1}(t)(\boldsymbol{K}+\boldsymbol{K}_\Omega(t)) & -\boldsymbol{M}^{-1}(t)(\boldsymbol{C}+\boldsymbol{G}(t))\end{bmatrix}\begin{bmatrix}\boldsymbol{q}\\ \dot{\boldsymbol{q}}\end{bmatrix}\\ &= \boldsymbol{A}(t)\boldsymbol{x}(t).\end{aligned} \tag{4.14}$$

4.1.4.2 Properties of periodic functions

In the following results the term *time-periodic matrices* will be used to avoid confusion with the term *periodic matrices.*

Theorem 1 *Let $\boldsymbol{F}(t)$ and $\boldsymbol{G}(t)$ time-periodic matrix of period T such that $\boldsymbol{F}(t+T) = \boldsymbol{F}(t)$ and $\boldsymbol{G}(t+T) = \boldsymbol{G}(t)$, then their product $\boldsymbol{K}(t) = \boldsymbol{F}(t)\boldsymbol{G}(t)$ is also of period T.*

Indeed

$$\boldsymbol{K}(t+T) = \boldsymbol{F}(t+T)\boldsymbol{G}(t+T) = \boldsymbol{F}(t)\boldsymbol{G}(t) = \boldsymbol{K}(t) \tag{4.15}$$

Theorem 2 *Let an invertible time-periodic matrix $\boldsymbol{M}(t)$ of period T such that $\boldsymbol{M}(t+T) = \boldsymbol{M}(t)$ then its inverse $\boldsymbol{M}^{-1}(t)$ is also of period T.*

Indeed by definition

$$\begin{cases}\boldsymbol{M}(t)\boldsymbol{M}^{-1}(t) = \mathbb{I}\\ \boldsymbol{M}(t+T)\boldsymbol{M}^{-1}(t+T) = \mathbb{I}\end{cases} \tag{4.16}$$

or $\boldsymbol{M}(t+T) = \boldsymbol{M}(t)$ meaning that, by identification, $\boldsymbol{M}^{-1}(t+T) = \boldsymbol{M}^{-1}(t)$ such that $\boldsymbol{M}^{-1}$ is time-periodic of period T.

4.1.4.3 Coupling periodicity

The temporal parts of the matrices of the equations of motion only consist in the coupling blocks as they were defined in 3.2.2. One can observe that their only time dependence comes from the $\boldsymbol{H}$ and $\boldsymbol{B_0}$ or their transpose or derivatives which doesn't change the nature of their periodicity. These matrices are made up of $\cos(\Omega t)$ and $\sin(\Omega t)$ meaning that they admit a period of $T = \frac{2\pi}{\Omega}$ such that

$$\boldsymbol{H}(t+T) = \boldsymbol{H}(t) \text{ and } \boldsymbol{B_0}(t+T) = \boldsymbol{B_0}(t) \text{ with } T = \frac{2\pi}{\Omega}. \tag{4.17}$$

Now, the computation of the coupling blocks implies the usage of terms such as $\boldsymbol{H}$ or $\boldsymbol{B_0}$ or their transposes or derivatives which all remain of periodicity $T = \frac{2\pi}{\Omega}$. In the cases where the coupling blocks require the product of $\boldsymbol{H}$ or $\boldsymbol{B_0}$ or their transposes or derivatives theorem 1 assures that it remains of period T. This means that all the structural matrices $\boldsymbol{M}$, $\boldsymbol{G}$, $\boldsymbol{K}_\Omega$ are of periodicity T.

Finally, the state-space matrix $\boldsymbol{A}(t)$ contains either no time dependence or the product of the inverse of a time-periodic matrix with another. According to theorem 2 and 1 used together the product remains with a time-periodicity of T such that

$$\boldsymbol{A}(t+T) = \boldsymbol{A}(t) \text{ with } T = \frac{2\pi}{\Omega}, \tag{4.18}$$

Since the state-space formulation of the problem proved to be periodic the Floquet stability analysis may be used to assess its stability.

4.1.4.4 Sampling of the state-space

For best numerical efficiency during the integration the signal $\boldsymbol{A}(t)$ shall be computed in advance on the whole time domain of integration. This can be done extremely efficiently using tensor in *Python* to compute all of the required coupling blocks in one go instead of redoing it for each single time step of the numerical solver.

However, to do such accurately the sampling frequency of the state-space signal shall be small enough as to capture all of the information. This is done simply by respecting the sampling theorem (Shannon, 1949[32]). In other words the sampling frequency f_s of $\boldsymbol{A}(t)$ shall be such that

$$f_s > \frac{2.6}{T_{A(t)}} = \frac{2.6\Omega}{2\pi}. \tag{4.19}$$

This won't be an issue at all for monodromy as only integration from $t = 0$ to $t = T$ is of interest meaning that as long as 3 or more points are considered in the time vector used for interpolation the sampling theorem is satisfied.

4.2 Test models

4.2.1 4-bladed propeller

In the following sections and until stated otherwise the following configuration will be investigated. It is a simple 4-bladed clamped propeller, depicted in Fig 4.1, the shaft is mounted on a wing that will be either rigid or flexible depending on what parameters are studied. All of the default parameters are given in Table 4.1 and will be the one used unless explicitly stated otherwise in the later sections. Whatever the value of the parameters the shaft and the wing are expressed in the fixed frame and coupled with the propeller blades in the rotating frame according to the procedure extensively described in 3.2.3.

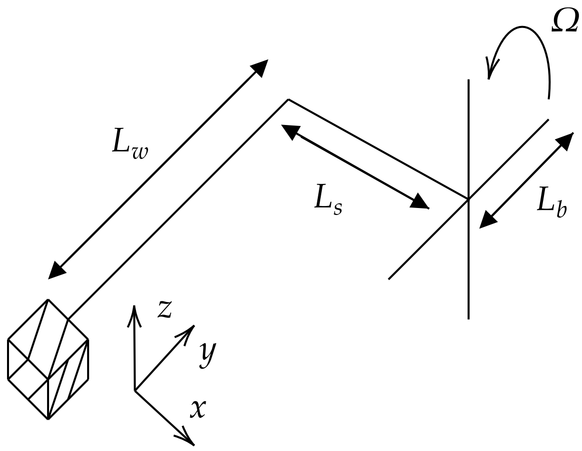

Figure 4.1: 4 bladed propeller schematic

Parameters	Value
Material	
E	210 GPa
ν	0.3 [−]
Geometry and sections	
L_w	3 m
L_s	1 m
L_b	0.8 m
b_w, h_w	0.25, 0.20 m
b_s, h_s	0.035, 0.045 m
b_b, h_b	0.03, 0.04 m
Operating conditions	
Ω	50 rad/s
Modal damping	
ζ	0.05 [-]

Table 4.1: 4 bladed propeller parameters

4.2.2 Multi-propeller

4.3 Stiff nature of the problem

This section condenses most of the numerical aspects of the computation of the monodromy matrix. In particular the stiff nature of the system will be investigated. Then, the choice of the numerical scheme to be used will be discussed. Finally, the computation time as a function of different parameters of the problem will be reviewed.

4.3.1 Computation of the monodromy matrix

According to what was stated in section 4.1 the Floquet analysis assesses the stability of the periodic system using the eigenvalues of the monodromy matrix of the said system.

According to section 4.1.3 the most straightforward way to evaluate the state-transition matrix is to integrate, from $t = 0$ to $t = T$ each element of the basis. Another solution would have been to use analytical relations to compute the monodromy matrix for example using the *Peano-Baker series*. Yet, such an approach requires the computation of nested integral at each time step and therefore was quickly dismissed. This is consistent with the remarks made in literature (Wilson, 1996 [25]) stating that the state-transition matrices are often computed by time integration of the basis elements.

Since each element of the basis shall be integrated from 0 to T the choice of the right numerical integration scheme is critical for the computation of the state-transition matrix and by extension of the monodromy matrix. The problem can be rewritten, as its autonomous state-space formulation as

$$\frac{d\boldsymbol{x}}{dt} = \boldsymbol{f}(\boldsymbol{x}, t) = \boldsymbol{A}(t)\boldsymbol{x}(t). \tag{4.20}$$

Resolution of such a problem will be greatly influenced how stiff it turns out it be.

4.3.2 Stiff problems (Inspired by Shampine, 1979[30])

Literature gives a clear definition of stiff problems. Those are problems that cannot be handled by classical integration methods unless allowing an extremely large amount of time and computational power to render the round-off error small enough.

Let us consider a Taylor series expansion of equation 4.20 around a particular solution $\boldsymbol{g}(t)$

$$\frac{d\boldsymbol{x}(t)}{dt} = \boldsymbol{J}(t, \boldsymbol{g}(t))(\boldsymbol{x} - \boldsymbol{g}(t)) + \frac{d\boldsymbol{g}(t)}{dt} \tag{4.21}$$

with $\boldsymbol{J}$ being the Jacobian matrix of the system. Assuming that $\boldsymbol{J}(t, \boldsymbol{g}(t))$ slowly changes overtime allows to approximate it locally by a constant matrix $\boldsymbol{A}$ which is diagonal and made of the eigenvalues of $\boldsymbol{J}$. This yields to a set of uncoupled equations that can be written for the equation i as

$$\frac{dx_i(t)}{dt} = \lambda_i(x_i - g_i(t) + \frac{dg_i(t)}{dt} \tag{4.22}$$

with $\lambda_i = A_{i,i}$ being the i-th eigenvalue of J. Such an equation admits an analytical solution such as

$$x_i(t) = (x_i(0) - g_i(0))e^{\lambda_i t} + g_i(t). \tag{4.23}$$

3 different cases appear. If $Re(\lambda_i)$ is large and positive then the solution $x_i(t)$ spread over a large area for different values of initial conditions $x_i(0)$, such problems are said to be *unstable*. If $Re(\lambda_i)$ is positive or negative but not too large then the problem is said to be *neutrally stable* which is the ideal case for conventional integration schemes. Finally, if $Re(\lambda_i)$ is large and negative then the solution quickly converges to $g_i(t)$ whatever the initial condition is. In the latter configuration problem is said to be *super-stable*, this configuration is ideal for the propagation and amplification of error in the numerical scheme from one step to the next, defining *stiff* problems.

Indeed, let us consider a simple Euler integration scheme from the n-th to the n + 1-th step of integration

$$x_i^{(n+1)} = x_i^{(n)} + h_n x_i'^{(n)} + \epsilon, \tag{4.24}$$

where the truncation error ϵ is approximated by

$$\epsilon = |\frac{h_n^2 x_i''^{(n)}}{2}|, \tag{4.25}$$

such that the step size reads

$$h_n = \left(\frac{2\epsilon}{|x_i''^{(n)}|}\right)^{1/2}. \tag{4.26}$$

Re-injecting $|x_i''^{(n)}|$ from equation 4.24 into the step size allows to write h_n asymptotically for 2 different cases reading

$$h_n = \begin{cases} \left(\frac{2\epsilon}{|[x_i(0)-g_i(0))]\lambda_i^2}\right)^{1/2} \text{ when } t \text{ is small.} \\ \left(\frac{2\epsilon}{|g_i''(t_n)|}\right)^{1/2} \text{ when } t \text{ is large.} \end{cases} \tag{4.27}$$

As we placed ourselves at the case where λ_i is large and negative this means that the required step-size h_n is extremely small when t is small and extremely large when t is large (as $g_i''(t_n)$ is small because $g_i(t_n)$ is assumed to be slowly varying). In practice this implies that the step size shall be extremely small at the beginning of the time domain and extremely large afterwards in terms of the truncation error.

It is also crucial to look at the stability to make sure that the error committed at step size n isn't amplified at step size $n+1$ rendering the scheme unstable. Do to such let us define the error committed at each time step as the difference between the approximated solution and the real solution

$$\delta_n = x_i^{(n)} - x_i(t_n). \tag{4.28}$$

Then the error committed at next time step can be written as

$$\delta_{n+1} = (1 + h_n Re(\lambda_i))\delta_n + \epsilon_{n+1}, \tag{4.29}$$

which requires

$$-2 \leq h_n Re(\lambda_i) \leq 0 \iff 0 \leq h_n \leq \frac{-2}{Re(\lambda_i)}, \tag{4.30}$$

such as to not amplify the error committed at previous time step. This isn't an issue in the transient region as h_n is already required to be very small when t small as discussed above. However, outside of the transient region, the stability requirement remain very strict toward h_n since the real part of λ_i is large and negative even tough the truncation error requirements are fairly lose since $g_i(t_n)$ is slowly varying. This leads to an extremely inefficient situation for classical integration scheme where the step-size h_n must be kept extremely low as otherwise the solver would diverge even tough the truncation error committed as each step is extremely small. Non-stiff solvers are able to handle such configurations by reducing the step size as much as needed but requiring lots of resources for the computation of a solution that has almost reached equilibrium anyways which is extremely inefficient.

In other words, if no eigenvalues of $\boldsymbol{J}(t, \boldsymbol{g}(t))$ are of positive real parts, with at least one of them having a large negative real part $Re(\lambda_k)$ associated to slowly varying solution $g_k(t)$ then the problem can be considered as *stiff* whenever the transient $(x_k(0) - g_k(0))e^{\lambda_k t}$ as died out. Meaning that the problem that is initially not stiff becomes stiff at some point on the time domain.

Physically, the *stiffness* of a problem can be understood by a gap between the eigenvalues of the Jacobian and the physics of the problem. For example a phenomena that slowly converges to an equilibrium that admits one eigenvalue of $\boldsymbol{J}$ whose real part is large and negative and vice-versa. "The essence of stiffness is that one has a slowly varying solution which is such that some perturbations to it are rapidly damped" (Shampine, 1979, p.5[30]). Applied to our whirl-flutter problem it means that if it's found out that some eigenvalues of the Jacobian matrix are of large and negative real parts then the introduction of damping will be critical as to make the solution $\boldsymbol{g}(t)$ vary more quickly effectively reducing the gap with the highly damped phenomenons associated to the eigenvalues of large and negative real parts and the physics of a lightly damped solution.

4.3.3 Stiffness detection

Allow a reformulation of the equations of motion onto a state-space formulation

$$\dot{\boldsymbol{x}}(t) = \boldsymbol{A}(t)\boldsymbol{x}(t) + \boldsymbol{B}(t)\boldsymbol{u}(t) = \boldsymbol{F}(t), \tag{4.31}$$

the Jacobian matrix $\boldsymbol{J}(t)$ of such a system can be computed directly from

$$\boldsymbol{J}(t) = \frac{\partial \boldsymbol{F}(t)}{\partial \boldsymbol{x}(t)} = \boldsymbol{A}(t). \tag{4.32}$$

This means that the stiff behavior of our system can be studied directly be investigating the eigenvalues of the state-space matrix of the system $\boldsymbol{A}(t)$ over time. Results are displayed in Fig 4.2 and draw to multiple conclusions.

First, Fig 4.2b shows a periodic pattern of periodicity $T = \frac{2\pi}{\Omega} \approx 0.031$s (for $\Omega = 200$ Rad/s) further assessing the periodic nature of the state-space.

Then, Fig 4.2a reveals that there always exist at least one eigenvalues whose real part is fairly large and negative especially as larger beam sections b, h are considered. Fig 4.2b also reveals for small beam sections there exist some regions in the time domain where at least one of the eigenvalues as a positive real part making the system non-stiff meaning that the system periodically switches between a stiff and non-stiff behavior. For larger beam sections there can not exist any eigenvalue whose real part is positive making the system stiff along the whole time domain of integration.

Finally, as said above for larger beams sections it may be that no real parts of eigenvalues above 0 appear. This means that the numerical integration of the system is stiff but it also means that no time integration is necessary to assess its stability. Indeed, since no real parts of any eigenvalues crosses 0 the signal is never amplified anywhere therefore ensuring of the stability of the system without any need of integration.

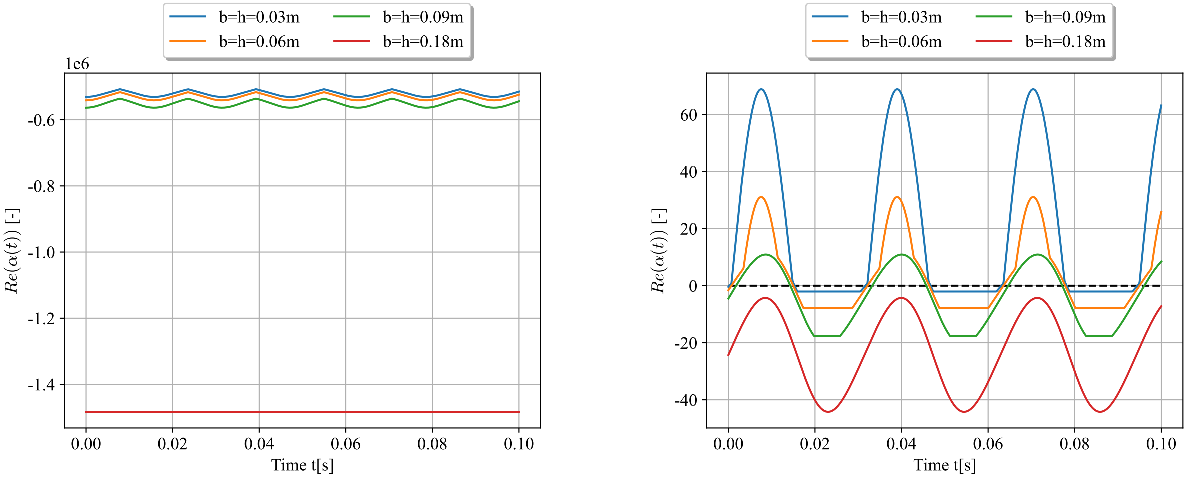

(a) Minimum eigenvalue of A over time.

(b) Largest eigenvalue of A over time.

Figure 4.2: Real part of eigenvalues $\alpha_k(t)$ of the state-space matrix A(t) over time. Standard 4 bladed propeller from section 4.2.1 was used with different beams sections $(b_b, h_b) = (b_s, h_s) = (b, h)$ and assuming a rigid wing

The latter argument is perhaps better illustrated using Fig 4.3 that displays the maximum and minimum values of the signal $Re(\alpha_k(t))$ with α_k the eigenvalue of largest real part at each time step. It shows that for all beam sections there will always be some parts of the time domain where the real part of the largest eigenvalue is below 0 making the system stiff in those parts of the domain. This shows that stiffness is impossible to avoid whatever the chosen geometry. Also, Fig 4.3 reveals that for large enough beam sections the largest eigenvalue found $Re(\alpha_k)(t)$ defines a time signal whose maximum is below 0 making the system stiff over the whole time domain but also ensuring that the system is stable.

Careful inspection of Fig 4.3 also shows some incoherent values at extremely small beam sections. Such values cannot be considered as for extremely small beam sections phenomena such as local buckling will occur and not be taken into account by the model.

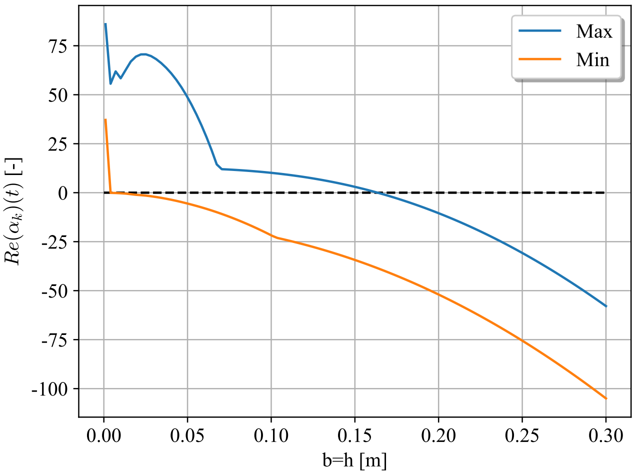

Figure 4.3: Maximum and minimum of the time signal $Re(\alpha_k)(t)$ defining its envelope for different beam sections, α_k being the eigenvalue of A(t) with the largest real part at each time step. Standard 4 bladed propeller from section 4.2.1 was used with different beams sections $(b_b, h_b) = (b_s, h_s) = (b, h)$ and assuming a rigid wing

4.3.4 Stiffness of the problem with rotation speed

Following the stiffness detection procedure stated in section 4.3.3 one can construct an analog to Fig 4.3 but with different rotations speed considered yielding to Fig 4.4.

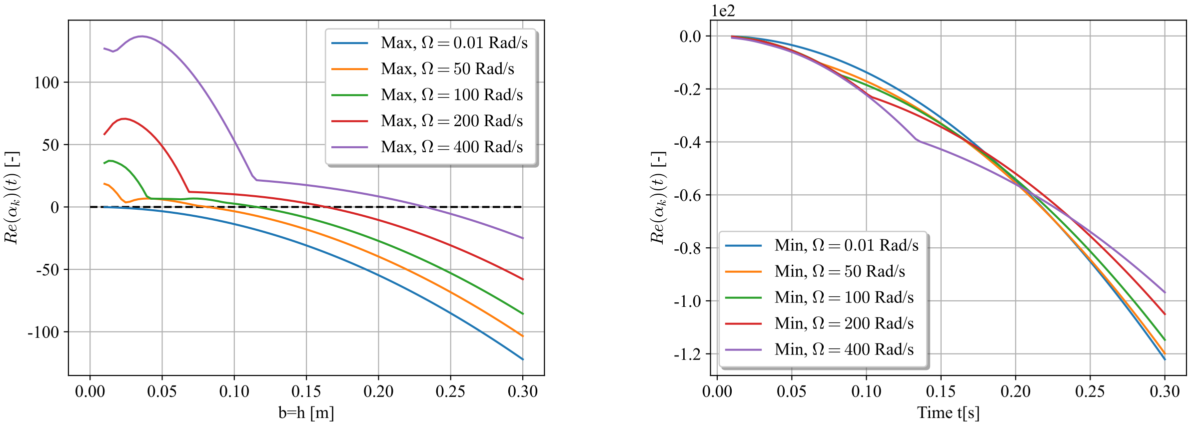

(a) Maximum of time signal $Re(\alpha_k)(t)$

(b) Minimum of time signal $Re(\alpha_k)(t)$

Figure 4.4: Maximum and minimum of the time signal $Re(\alpha_k)(t)$ for different beam sections, α_k being the eigenvalue of A(t) with the largest real part at each time step. Standard 4 bladed propeller from section 4.2.1 was used with different beams sections, different rotation speeds and assuming a rigid wing

Fig 4.4b shows that the greater the rotation speed Ω the larger the maximum of the time signal $Re(\lambda_k)(t)$ is. If Ω is almost 0 then no positive real parts are ever achieved which is consistent with system being always stable when no rotation speeds are considered. If Ω is large then larger and larger beam sections must be considered to reach the point where the time signal $Re(\lambda_k)(t)$ admits no positive value over the time domain satisfying a sufficient but not necessary condition for stability without requiring computation of the monodromy matrix.

Finally, Fig 4.4a reveals that the minimum of the time signal $Re(\lambda_k)(t)$ is more or less independent of the rotation speed and always smaller than 0.

4.3.5 Small Conclusion

Section 4.3.3 showed that an eigenvalue of really large and negative real part was always found in the system no matter if it is coupled or not. It was also found that, for some parts of the time domain, there exist at least one eigenvalue with a positive real part while, for some other parts of the time domain, this isn't the case. The coupled problem was therefore proved to oscillate between a stiff and non-stiff behavior along the time domain. Finally, section 4.3.4 showed that as larger rotation speeds were considered the proportion of the time domain where the system is stiff tends to reduce which is expected to reduce the time of integration. This effect will be combined with the fact that time integration for the monodromy matrix shall be done from 0 to $T = \frac{2\pi}{\Omega}$ which reduces with the rotation speed.

4.4 Numerical scheme selection

4.4.1 Available numerical schemes

Due to the stiff nature of the problem the selection of the right numerical scheme is critical. Let us investigate the different integration algorithms implemented in the *Scipy.solve-ivp* module namely *LSODA, Radau, BDF* and *RK45*. The first 3 schemes are implicit and well suited for stiff systems while the last one is explicit and therefore should ill-suited for stiff systems. It's performances will only be reviewed here to illustrate how much more efficient stiff algorithms are. Table 4.2 gives an introductory insight on the performances of the different algorithms.

Scheme	**Number of elements per beam**					
	1	**2**	**3**	**4**	**5**	**6**
RK45	132.9s	>999s	>999s	>999s	>999s	>999s
LSODA	18.24s	103.42s	391.36s	1461.2s	>999s	>999s
BDF	3.25s	9.89s	34.35s	533.4s	>999s	>999s
Radau	2.86s	16.87s	67.33s	>999s	>999s	>999s

Table 4.2: Computation time of the monodromy matrix for different number of elements per beam and using different integration procedures. Reference system depicted in Fig 4.2.1 was used ($\Omega = 200$ Rad/s). All computation were done on the same computer using one single core of an Intel core i5-8600K @ 3.60 Ghz

First, the stiff nature of the problem that was discussed and assessed all throughout the previous section is also clearly visible with the large disparities in the performances of the different algorithms. *RK45* being an explicit algorithm performed the worst as expected and *LSODA* being an hybrid explicit/implicit algorithm also performed much worse then the full implicit algorithms *BDF* and *Radau*. This goes in the sense that even though the problem isn't stiff on the whole time domain (c.f section 4.3.3) the cost of checking stiffness at each time step overall makes the integration slower than directly using a stiff integration such as *BDF*.

Finally, inspecting how the computation time evolves with the number of elements per beam using *BDF* or *Radau* shows than the required integration time grows very quickly. This is further assessed by Fig 4.5 which shows that, as more elements are considered, the number of LU decompositions to do for the computation of monodromy quickly grows, which was to be expected as the size of the size grows and thus the number of elements of the basis to integrate. This naturally greatly increases the required computation time, especially at low rotation speeds with computation for 3 elements where computations in a reasonable time simply weren't possible if the rotation speed was too low. Fig 4.5a displays the computation time as it as a much more intuitive and practical measure but since it's measure is susceptible to discrepancies due to external factors, for example if the bus of the super-computer is overloaded, the number of LU decomposition is given as well in Fig 4.5b as a more rigorous measure of the required computational power.

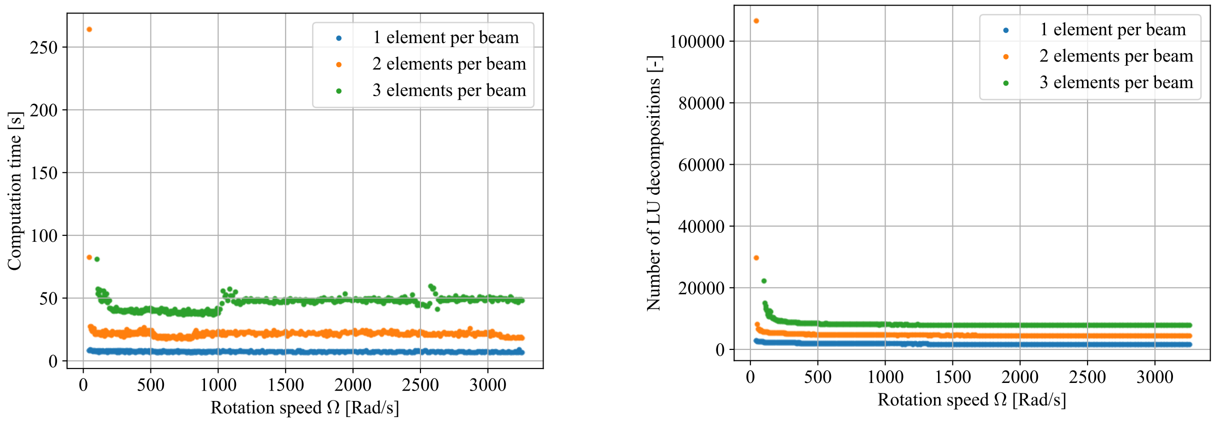

(a) Computation time

(b) Number of LU decompositions

Figure 4.5: Computation time and number of LU decompositions as a function of the rotation speed for different number of elements per beam. Computation started at $\Omega = 40$ Rad/s for 1 and 2 elements per beam and $\Omega = 100$ Rad/s for 3 and 4 elements per beam. Computation where done using the standard model 4.2.1 and conducted with *NIC5* from *CÉCI*.

No estimation of the time complexity of the problem will be provided as complex and adaptive algorithms whose time complexity are highly dependent of the problem are used. This is especially the case with *BDF* that uses different orders of backward differentiation formulas conjointly (Shampine, 1997[31]). However, the effect of different problem parameters on the required computational power will be discussed further in the follow subsections.

All of these results show that parallelization is highly necessary to conduct the numerous computations of the following sections. Luckily the problem is embarrassingly parallel as the different integrations can very easily be done independently. Parallelization will be conducted using the super-computer of *University of Liège* namely, *NIC5* allowing to run the computer on multiple powerful cores at the same time, usually using 8 or 12 cores.

Also, the integration procedure could be optimized by integrating a matrix of the elements of the basis as initial conditions, being the identity, instead of integrating each element of the basis one by one. *Scipy.solve-ivp* doesn't support such integrations by default and therefore requires to flatten and reshape the arrays at each time-step which breaks the implementation of the implicit algorithms *Radau, BDF, LSODA* as the system to solve becomes absurdly large, rendering those methods unusable in that configuration. That being said, the explicit algorithms remained usable and the computation using *RK45* was greatly sped up almost, but not quite, matching the speed of the implicit algorithms. This clearly shows the opportunity to develop a stiff integration algorithm that can handle a matrix of initial values, which couldn't be done in that thesis due to time constraints.

4.4.2 Computation time and rotation speed

As discussed in section 4.1.3 evaluation of the monodromy matrix requires to integrate each element of the basis as initial conditions until one period $T = \frac{2\pi}{\Omega}$. Moreover, section 4.3.4 showed that the percentage of the time domain where the integration is stiff reduces with the rotation speed. Increasing the rotation speed is therefore expected to quickly reduce the required computation time for a given structure. *RK*45 and *LSODA* will be excluded by default of the computations as it was shown in section how ill-suited they are for this problem.

Fig 4.6 displays that results and confirms that the required time to compute the monodromy matrix greatly decreases with an increase of the rotation speed until reaching saturation. This saturation could be explained by the fact that the period of the system is $T \sim \frac{1}{\Omega}$. Moreover, since integration was conducted with *scipy.solve-ivp* the *Python* interpreter has to be called at each time step, this is likely the cause of the lower bound to the computation time even for very large rotation speeds. In other words, there exist an hard limit on how low the computation time can get even if the rotation speed Ω were to be infinite.

The only way to reduce the lower bound would be to directly use the wrapper of an integrator written in an efficient compiled language such as *Fortran* or *C/C++* which is able to take a pointer to the right-hand-side function of the state-space such that all the computations are done outside of the Python environment without intermediary calls to the Python interpreter. This could be done for example using the *numbaLSODA* package but wasn't implemented in this thesis due to time constraints as it would require to modify large portions of the code.

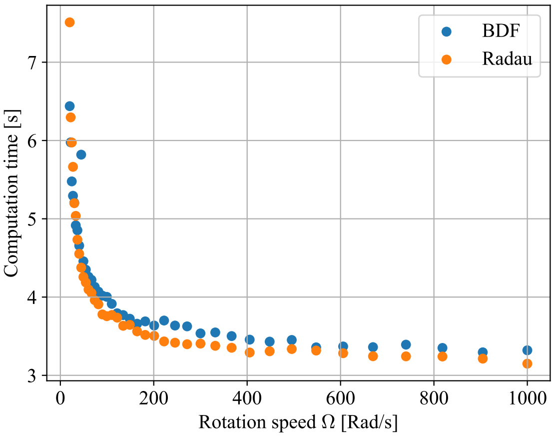

Figure 4.6: Computation time as a function of the rotation speed for different numerical schemes with 1 element per beam. Computation where done using the standard model 4.2.1 and conducted with one core of *NIC5* from *CÉCI*

4.4.3 Computation time and damping

As discussed in section 4.3.2 introduction of structural damping will be critical as it will tend to reconcile the discrepancy between the eigenvalues of large and negative real parts of the Jacobian, usually associated to highly damped phenomenons, and how quick the solution converges. It is therefore expected than introduction of damping will greatly fasten the computations. Different amounts of structural damping are introduced into the system using the procedure described in 2.2.2.1 but with different amounts of imposed modal damping ζ on the first 2 modes.

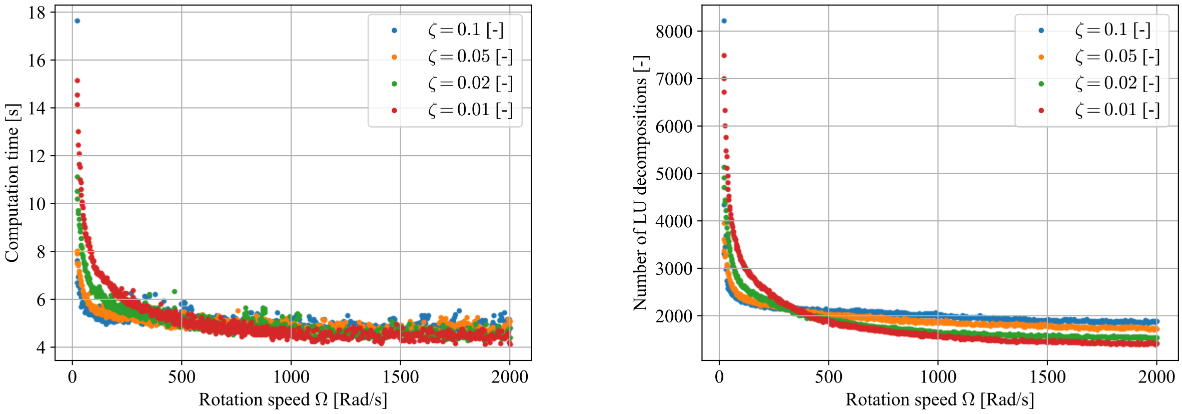

(a) Computation time

(b) Number of LU decompositions

Figure 4.7: Computation time and number of LU decompositions as a function of the rotation speed for different amounts of modal damping with 1 element per beam. Computation where done using the standard model 4.2.1 and conducted with one core of *NIC5* from *CÉCI*.

Results are displayed in Fig 4.7. They reveal that first, as expected as larger modal damping values are considered the physics of the problem tends to align more with the eigenvalues of the Jacobian of the system, fastening the computations. These results show that it is desirable, from a numerical point of view, to admit a damping as large as possible as long as it wouldn't compromise the quality of the results. Effect of introduction of damping is also seen in the number of LU decomposition but depends on the rotation speed. For low rotation speeds more damping yields to a lower number of LU decomposition to perform meaning that less time steps are required for integration. For large rotation speeds the opposite is observed.

As a conclusion, introduction of damping is a critical parameter, at least at low rotation speeds Ω, of the computation speed.

4.4.4 Small Conclusion

Section 4.4.2 showed that an implicit algorithm adapted for stiff integrations has to be used. *BDF* has proved to be the best performing algorithm for this problem along with *Radau* having very comparable results. *BDF* will finally be chosen as the integration algorithm to use in this thesis, which is consistent with the literature often citing *BDF* techniques as very robust and reliable for stiff integrations (Curtiss, Hirschfelder (1952[31]) and Shampine (1997[6])).

4.5 Link between the state-space and monodromy

4.5.1 Eigenvalues of the monodromy and the state-space

Let α_k(t) being the eigenvalue of largest real part of the state-space matrix A(t), defining a signal $Re(\alpha_k)(t)$ whose properties will be studied for different geometries. The largest real part found in the Floquet exponents, *i.e* found from the eigenvalues of $\ln[(\Phi(0,T)]/T$, will denoted β_k and is also computed for different geometries. All of it results in Figure 4.8.

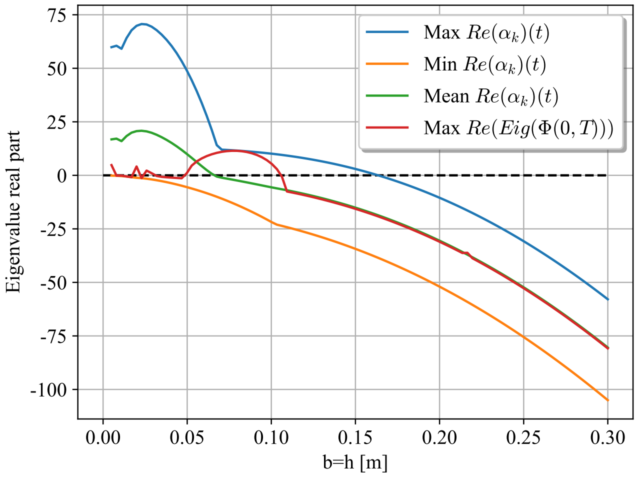

Figure 4.8: Maximum and minimum of the time signal $Re(\alpha_k)(t)$ defining its envelope for different beam sections, λ_k being the eigenvalue of A(t) with the largest real part at each time step. $\Omega = 200$ Rad/s.

Figure 4.8 reveals that for larger geometries the largest real part of the Floquet exponents can be very accurately approximated by the mean value of the signal $Re(\alpha_k)(t)$. This results might seem surprising but can actually be explained by considering the *Hill's method*. Hill's method is another possible way of assessing stability of linear time-variant periodic systems by doing a *harmonic balance method* to capture the frequency content of the state space matrix $\boldsymbol{A}$ and express it as a sum of harmonics instead of computing monodromy through means of time integration. Indeed, $\boldsymbol{A}$ expressed as a Fourier series would read

$$\boldsymbol{A}(t) = \boldsymbol{A}_0 + \sum_{n=1}^{N} a_n cos(nt) + b_n sin(nt) \tag{4.33}$$

such that if $\boldsymbol{A}(t)$ were to not change much with t then it could be approximated by it's static component $\boldsymbol{A}_0$. Moreover, let's consider the *Peano−Baker* series as defined in equation 4.12. In our case $\boldsymbol{A}(t) \approx \boldsymbol{A}_0$ commutes at all times such that

$$[\boldsymbol{A}(t), \boldsymbol{A}(s)] \approx 0 \ \forall s \in [0, T]. \tag{4.34}$$

This allows to get rid of the time-ordering operator $\mathcal{T}$ in the Peano-Baker formula for monodromy meaning that

$$\Phi(0,T) = e^{\int_0^T A(\sigma)d\sigma}. \tag{4.35}$$

Computing the eigenvalues of each side of the equation thus yields to

$$\gamma_k = e^{\int_0^T \alpha_k(\sigma)d\sigma}. \tag{4.36}$$

Finally, computing the largest real parts of the Floquet exponent gives

$$Re(\beta_k) = \frac{\ln[Re(\gamma_k)]}{T} = \frac{1}{T}\int_0^T Re(\alpha_k)(\sigma)d\sigma, \tag{4.37}$$

which explains that taking the average of the signal $Re(\alpha_k(t))$ can, as long as $\boldsymbol{A}(t)$ doesn't change too much with t, be a good approximation of the eigenvalue of largest real part of monodromy β_k. Under this assumption the stability of the system could be assessed directly without requiring computation of the monodromy. Physically, it can be explained by the fact that if the mean value of the signal $Re(\alpha_k(t))$ is negative then it means that even for the eigenvalue of largest real part the amplitude of the initial condition is more often reduced than it is amplified resulting in a overall stable result. Assuming that $\boldsymbol{A}(t) \approx \boldsymbol{A}_0$ actually being an application of the *Hill's method* with an harmonic balance method of order 0.

4.6 Ground-resonance & partial coupling verification

While the main purpose of this thesis is to study the *whirl-flutter* the *Python* framework developed is a priori suitable to study many other types of instabilities encountered in rotating machinery. One of them, the *ground-resonance* effect often encountered in helicopters is of particular interest as it is a purely mechanical phenomena linked to the flexibility of the blades (H.Reed, 1965) as discussed in section 1.5.1.3. This phenomenon is particularly well suited to validate the *Python* implementation of this thesis as it is a purely mechanical and self-excited mechanical instability due to leading or lagging motion of the blades displacing center of mass away from the center of rotation (Eckert (2007[7])). Since this thesis implements fully flexible rotating blades without aerodynamical effects ground-resonance is expected to be observed.

Ground-resonance has the advantage to be a very well documented phenomenon for which very simple analytical models exist. This thesis will use an adapted version of the Coleman model (Sanches (2011[27]) where the blades are only allowed lag/lead motion without flapping. It is hoped that this simple analytical model will provide a basis for validation of the code as well as provide insights on the properties and characteristics of the ground-resonance phenomenon. Moreover, the model used showed experimental relevance (Sanches et al. (2012)[29]).

4.6.1 Analytical model

The test model is displayed in Fig 4.9

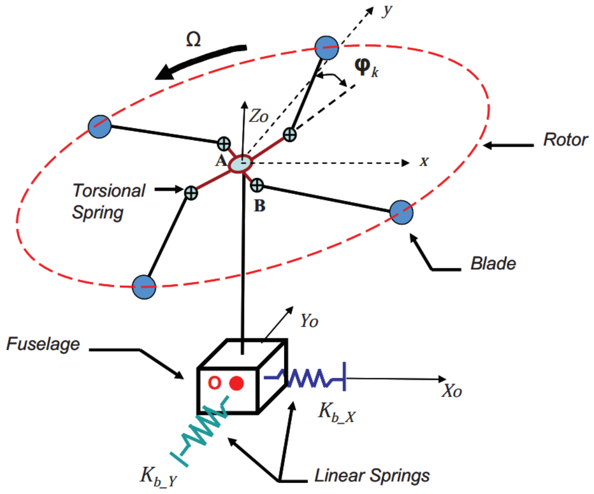

Figure 4.9: Schematic of the model. Taken from Sanches et al. (2011)[28].

Model given in Fig 4.9 assumes the fuselage to be a ponctual mass to which 2 spring are attached. This setup is then rigidly linked to the hub who admits 4 additional rigid links, acting as hinge offsets typically encountered in helicopters, finally linking to a torsional spring acting as an hinge followed by a last rigid link and a punctual mass making up the blade at its end. Numerical parameters of the analytical model are given in Tab 4.3

Parameter	**Value**
Fuselage mass, m_f	5000 kg
Longitudinal fuselage spring, K_b, Y	772723.4 N/m
Lateral fuselage spring, K_b, X	1888868.22 N/m
lag hinge offset, a	0 m
lag hinge frequency, ω_b	10 rad/s
Rotor radius, R	5.64 m
Blade mass, m_b	94.8 kg
Blade moment of inertia I_b	1084.7 kg.m^2

Table 4.3: Parameters of the analytical model.

4.6.2 Floquet analysis

Stability of such time dependent and periodic system is investigated either by doing a Coleman-transformation that aims at doing a time dependent change of variable to express the equation of motion in a time-invariable way or using Floquet analysis. The latter will be discussed here as this is also the approach used for the FE model in this master thesis.

Fig 4.10a summarizes the result and display 2 different instability zones in the Ω domain. According to theory these instabilities correspond to rotation speeds where a coalescence between fuselage and a lag/lead mode of the rotor blades occurs (Sanches (2011[27]), Lemmens *et al.* (2010[23])). This remains true even with Floquet modes as attested by Fig 4.11a where a clear coalescence of the imaginary part of 2 Floquet modes can be observed for the rotation speeds where an instability occurs.

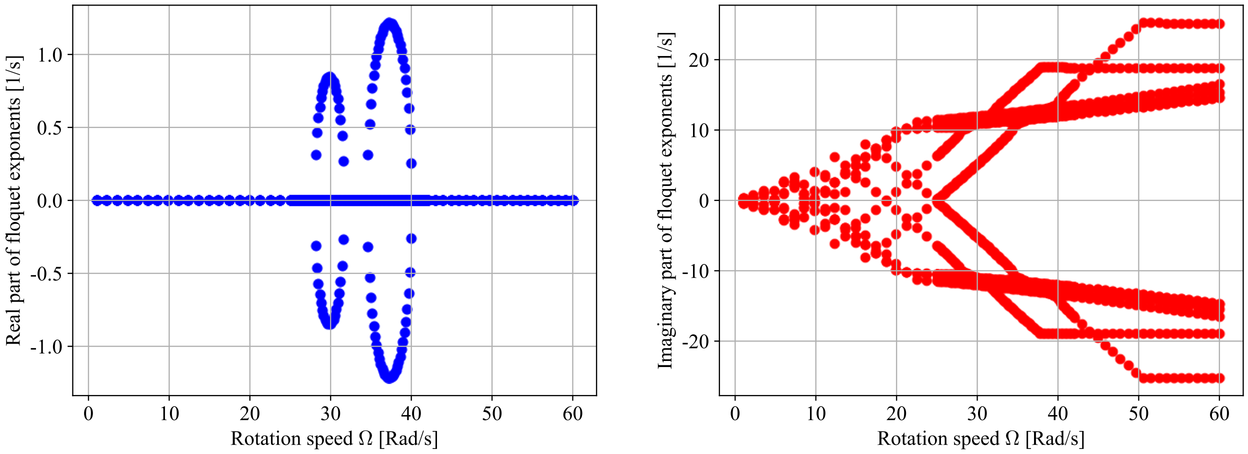

(a) Real part

(b) Imaginary part

Figure 4.10: Real and imaginary part of the *Floquet* multipliers of the analytical ground-resonance model of the isotropic rotor configuration (Model and parameters from Sanches (2011, p149[27])).

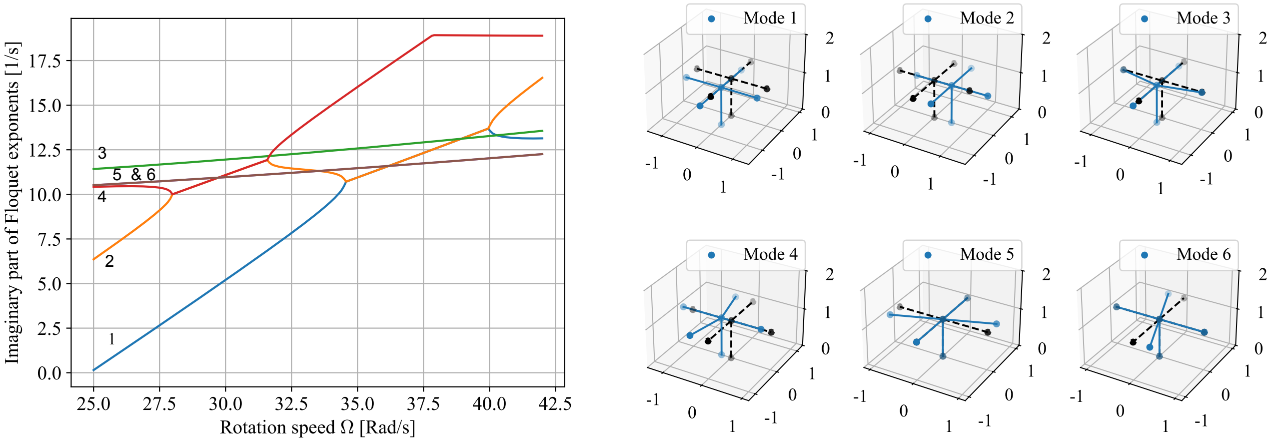

(a) Imaginary part of Floquet exponents.

(b) Floquet modes of the analytical model.

Figure 4.11: Coalescence of the Floquet modes

4.6.3 Partial coupling validation

The developed finite element framework will be adapted to reproduce the results of the analytical model. Figure 4.12 displays the finite element model used to mimic the analytical model.

First, the continuous beam blades from the finite element model were matched with the blades of the analytical model. The length of the beams is given by the rotor radius R (assuming no lag hinge offset a) and the section of the beam is given by matching it's mass with the punctual mass (and assuming a square section). As for the lag hinge frequency w_b it shall be the same as the first bending frequency of the blade beam in the finite element code.

Then, as the Python solver requires at least one node of the structure to be clamped as flexible link will be added *i.e* a beam with an extremely low young modulus E and of very large length. At its end the fuselage mass and longitudinal/lateral stiffnesses are placed. Finally, the fuselage and the propeller hub are linked together via a rigid link *i.e* a beam with an extremely large young modulus and of short length.

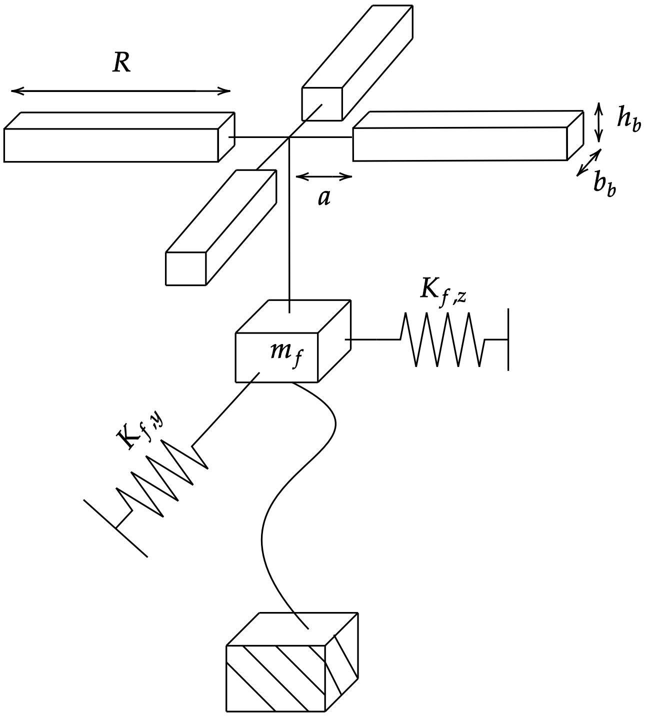

Figure 4.12: Finite element model equivalent

Results are given in Fig. 4.13 and show that the second instability is quite accurately predicated in terms of Ω bandwidth. The amplitude of the instability isn't the same but since it is model dependent this isn't an issue in this case. What's more of concern is that the second instability couldn't be predicted at all which means that the coupling is only partially validated. Integration of this system proved to be particularly difficult as exotic values of E and ρ were required for the link between the clamping and the fuselage mass and between the fuselage mass and the hub. These exotic values making integration not converge in many different cases. In order to still get results compromise had to made and unfortunately could be the reason why parts of the results show discrepancies compared to the analytical GR model. It appears thereby that this method of verification isn't the right one. Other methods, such as the *Coleman's transformation* couldn't be investigated in time.

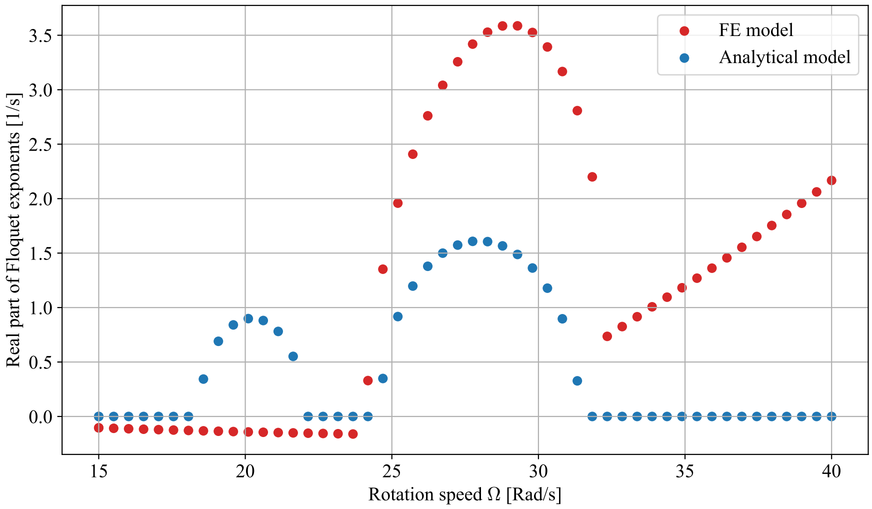

Figure 4.13: Real part of the Floquet multipliers of the finite-element ground-resonance model for an isotropic propeller configuration. Results are compared to those of the analytical model.

4.7 Stability and rotation speed

4.7.1 Convergence of the results

A first guess on the required number of elements per beam can be made by considering the results obtained for the verification of the FE model (Section 2.2.4) that used a structure which is quite similar to the 4-bladed rotor. It showed that for most modes 6 elements were enough such as to consider the model to be converged. That being said, as discussed in section 4.4.2 computational resources required for the problem quickly grow with the number of degrees of freedom. It is therefore in our best interest to keep the number of degrees of freedom to the lowest amount it's possible to get away with without compromising the quality of the results. This section will study how the quantity of interest, the largest real part of Floquet exponents, evolves on the rotation speed domain for different amount of nodes considered per beam. Results are shown in Fig 4.14.

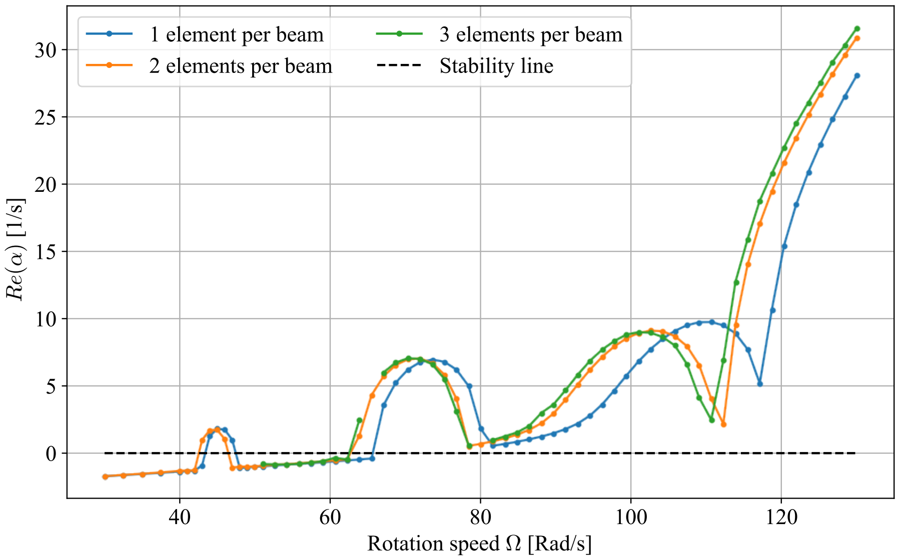

Figure 4.14: Largest real part of the Floquet exponents, α. Standard configuration of section 4.2.1 was considered with different rotations speeds and different number of elements per beam. For large number of nodes and low rotation speeds computations that couldn't converge weren't included. Computations were done in *NIC5* from *CÉCI*.

Figure 4.14 clearly shows 3 main Ω bandwidth where the system shows instabilities of particularly large amplitudes. These 3 regions are followed by a sudden change of regime, once a critical value of Ω has been reached, an ever-growing instability is found. The nature of each of these instabilities will be thoroughly discussed in the following sections.

That being said, it appears that the first instability remains relatively accurately predicted even with a fairly low number of elements per beam. This instability is therefore expected to imply a very low amount of blade vibration, *i.e* is expected to be a *disk instability* often encountered in turbo-machinery applications. For this instability using 1 element per beam is enough. This is not the case for the following instabilities and as such, they are expected to admit a richer dynamics of the structure with non-negligible blade vibrations and/or of more complex pylon motions. These instabilities, especially the third one, require more elements per beam to be considered converged such that at least 2 elements per beam are necessary.

When 3 elements per beam are considered it appears that at low rotation speeds the computations sometimes wouldn't converge with the numerical integration overflowing. This could be explained by the stiff nature of the system that perhaps sometimes requires a precision which is below the machine epsilon, those cases weren't included in the Figure.

As a conclusion, purely from a convergence of the results point of view it would be advisable to use 3 elements per beam. That being said, since computations with such a number of degrees of freedom sometimes lead to overflow at the numerical integrator level and due to the large cost of carrying such computations, it appears that using 2 elements per beam is the best trade-off. This amount of nodes is for sure not enough to assure that the model has converged but it should be amount such as to give a satisfying idea of the behavior of the system as long as qualitative aspects remain the priority.

4.7.2 Nature of the instabilities

4.7.2.1 First instability

In this section the first instability will be investigated. First, Fig 4.15 reveals a clear case of a *forward whirl flutter instability* where the propeller hub enters an ever-growing precession motion. Naturally, the precession is elliptic as the pylon beam has a rectangular shape. Fig 4.16 reveals that this instability originates from the coalescence of 2 Floquet modes, resulting in one them seeing it's real part go above the stability threshold making the overall structure unstable.

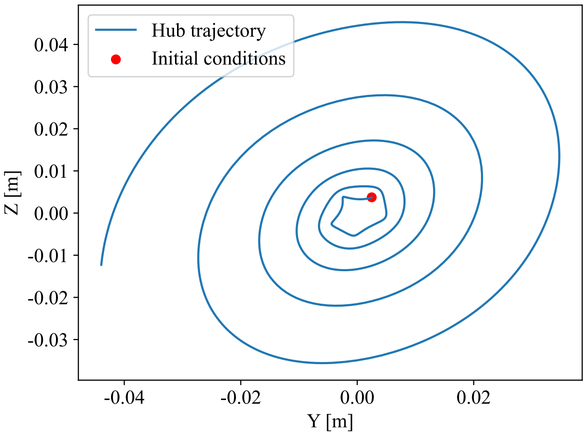

Figure 4.15: Hub trajectory within the first instability for $\Omega = 45$ Rad/s

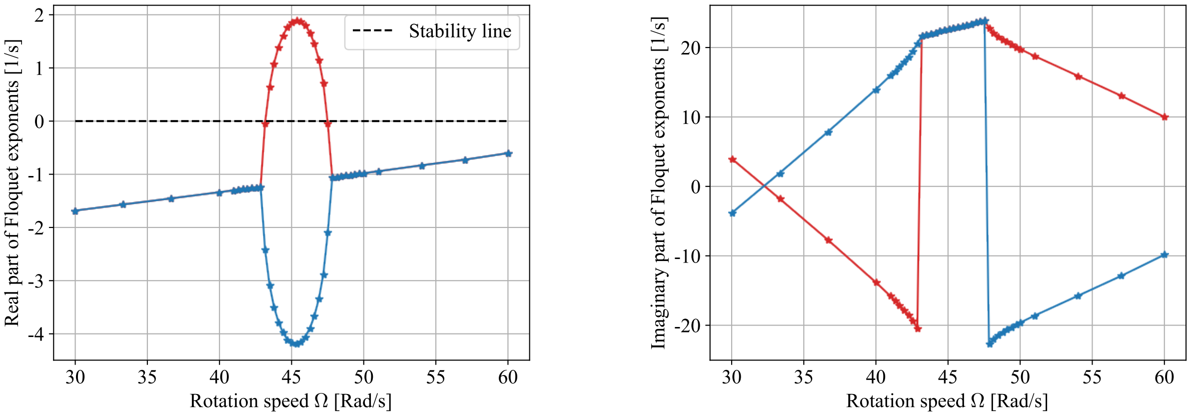

(a) Real part

(b) Imaginary part

Figure 4.16: Real and imaginary parts of the Floquet multipliers for the 2 modes of interest. Only modes of interest were included on the Figure. 2 elements per beam were considered. Computation where conducted on *NIC5* from *CÉCI*

Additional information about the propeller motion can be obtained by investigating the flapping and lagging/leading motion at the tip of each blade. Since all measures obtained from the FE model are in a fixed frame of reference additional precautions had to be taken to translate properly the *absolute* blade tip motion wether it is in terms of lagging/leading or flapping. Indeed for flapping in the fixed frame, displacements of the blade tip can have 2 different origins, wether it comes from a change in inclination of the propeller plane due to pylon bending, these will be named *nominal* displacements, or due to the bending of the blade itself, namely the *relative* displacements. Interest lies especially in the latter. As for lagging/leading the same can be said but the *nominal* displacements are due to translation and torsion of the pylon. Therefore, for each blade are plotted the absolute and relative lagging/leading motion as well as the flapping motion.

Results for the first instability are given in Fig 4.17 and show that very little self displacements of the blades are to be accounted for. This means that the blades are essentially acting as if they were rigid, this is consistent with the theory emitted in section 4.7.1 that this instability is indeed a disk instability. Naturally some vibrations are still happening on the blades as the system gains energy at hub level and tries to dissipate it. Moreover, the fact that the absolute blade flapping values are of opposite phase for opposite blades and with half a period phase lag between 2 sets of opposite blades correlates with the hub motion being almost a clean precession of the hub.

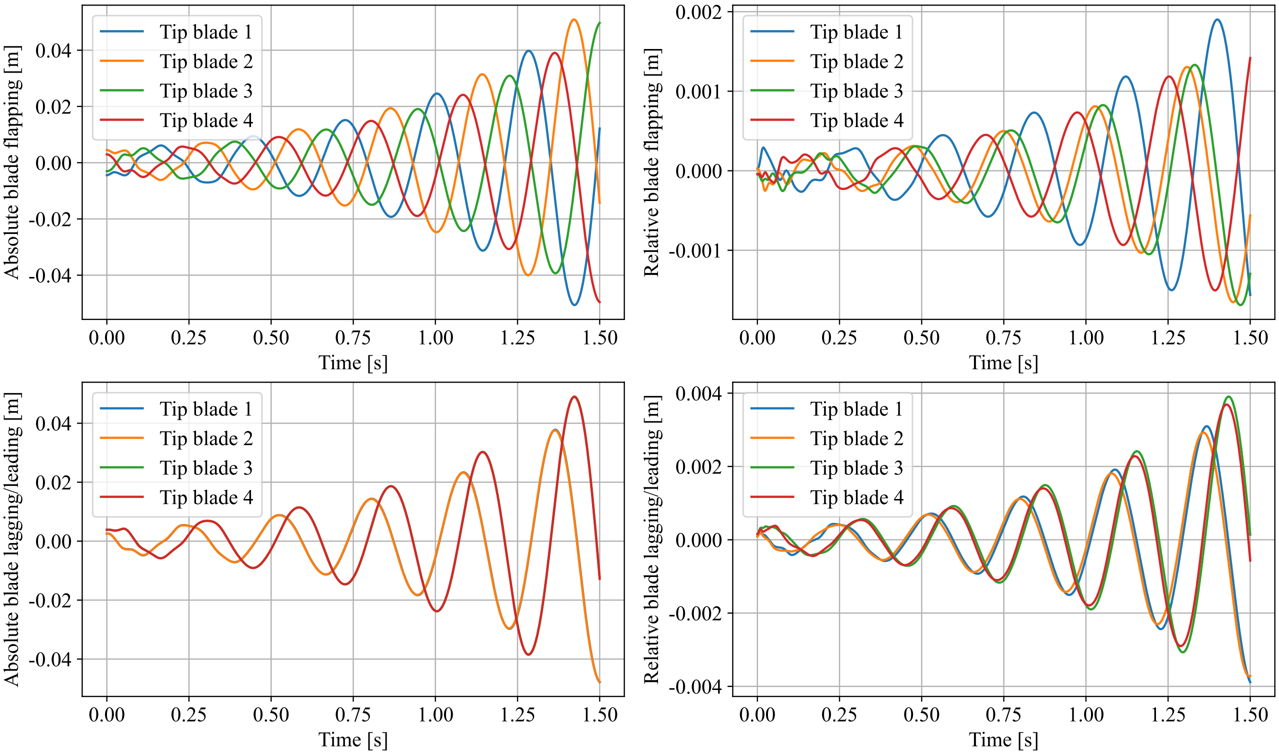

Figure 4.17: Absolute and relative lagging/leading and flapping motion of the blade for the $\Omega = 45$ Rad/s instability

4.7.2.2 Second instability

In this section the second instability will be investigated. Hub trajectory within this second instability, given in Fig 4.18 reveals that the hub indeed enters an ever growing precession motion but this time it is associated to a divergence of the pylon as well. This would typically be the behavior of a structure undergoing *divergence* where a mode with large bending displacements of the pylon becomes unstable which, due to gyroscopic coupling, creates an associated whirl motion as well. This theory is directly verified by inspection of Fig 4.19 where it's observed that the coalescence frequency is 0 Rad/s proving that this instability is indeed case of static divergence of the gyroscopic system. Finally, Fig 4.20 shows that almost all blade motion is done in the rotation plane without essentially no self vibrations of the blades. This indicates that the rotor part of the structure behaves like a rigid disk.

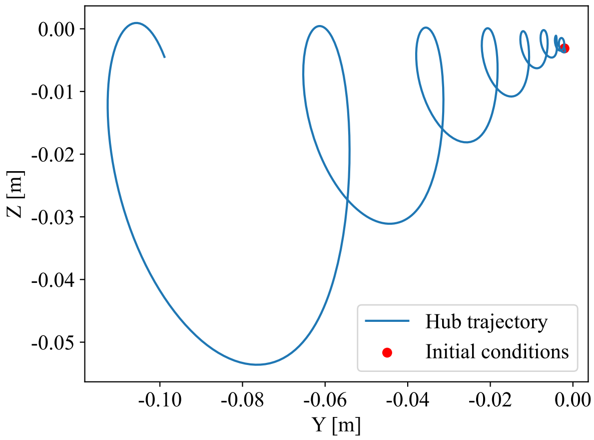

Figure 4.18: Hub trajectory within the second instability for $\Omega = 75$ Rad/s

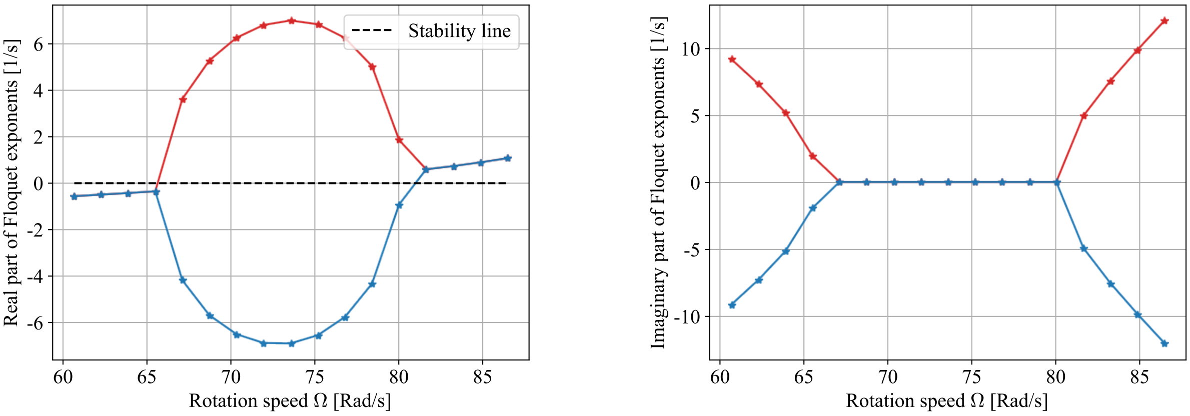

(a) Real part

(b) Imaginary part

Figure 4.19: Absolute and imaginary value of the Floquet multipliers. Only modes of interest were included on the Figure. 2 elements per beam were considered. Computation where conducted on *NIC5* from *CÉCI*

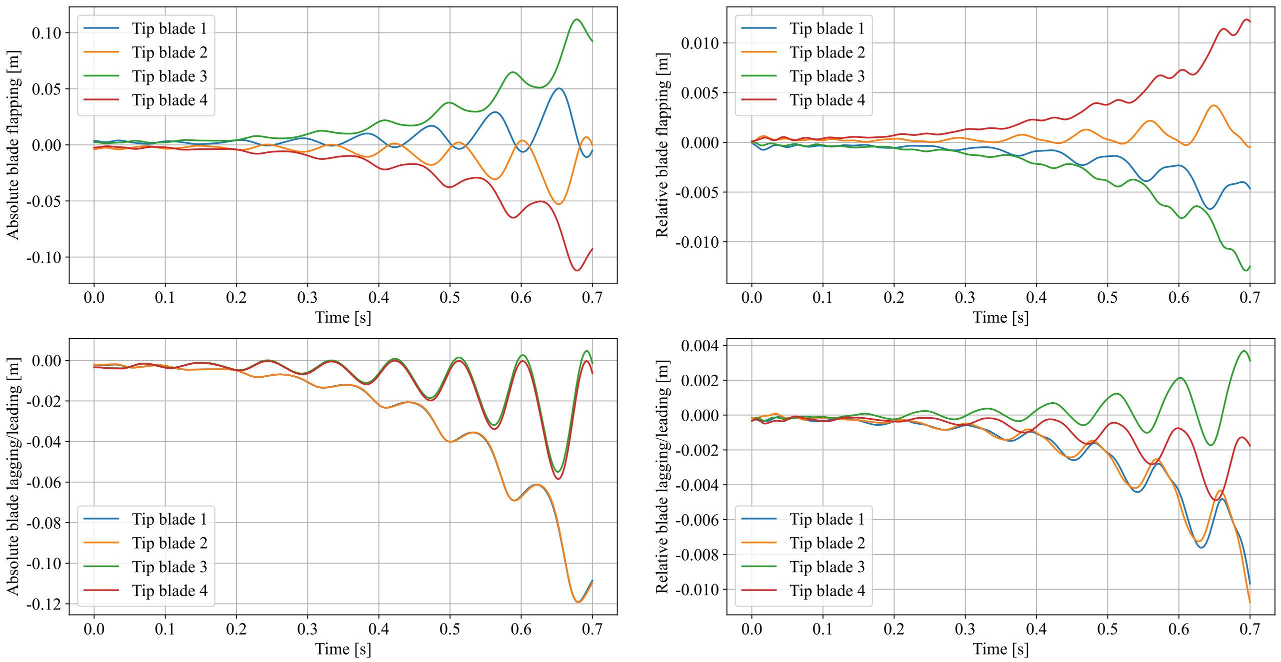

Figure 4.20: Absolute and relative lagging/leading and flapping motion of the blade for the $\Omega = 75$ Rad/s instability. 2 elements per beam were considered.

4.7.2.3 Third instability

The third instability, as depicted by the hub trajectory given in Fig 4.21 seems to be off different nature than the 2 previous ones. First, for the first time is it a *backward whirl* instability that is observed. Moreover, as expected in section 4.7.1, a richer motion is observed as it clearly appear that the mode that became unstable combines a whirl motion of the rotor along with a bending motion of the pylon. Also, as shown in Fig 4.22 this instability isn't associated to a coalescence of modes, which further sets is apart from the those previously encountered. Finally, Fig 4.23 shows that the rotor admit some non-neglegible self vibrations.

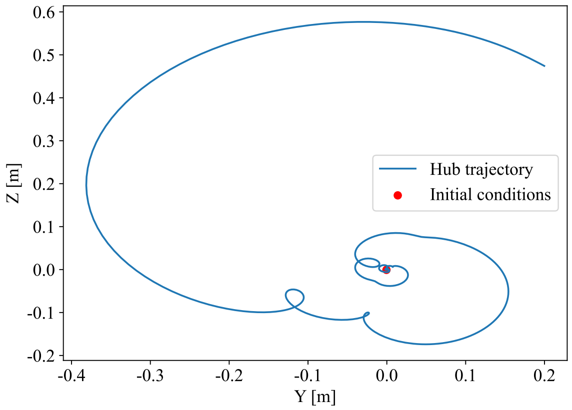

Figure 4.21: Hub trajectory within the third instability for $\Omega = 100$ Rad/s

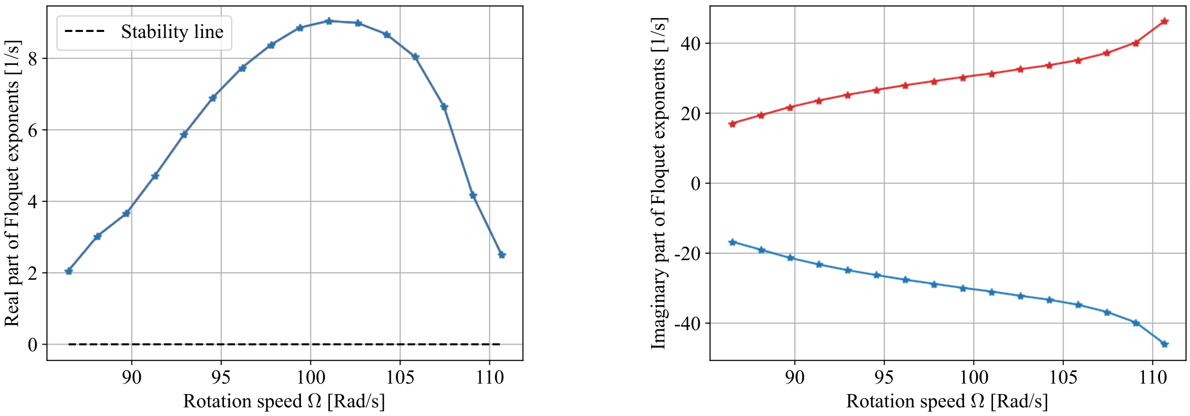

(a) Real part

(b) Imaginary part

Figure 4.22: Absolute and imaginary value of the Floquet multipliers. Only modes of interest were included on the Figure. 2 elements per beam were considered. Computation where conducted on *NIC5* from *CÉCI*

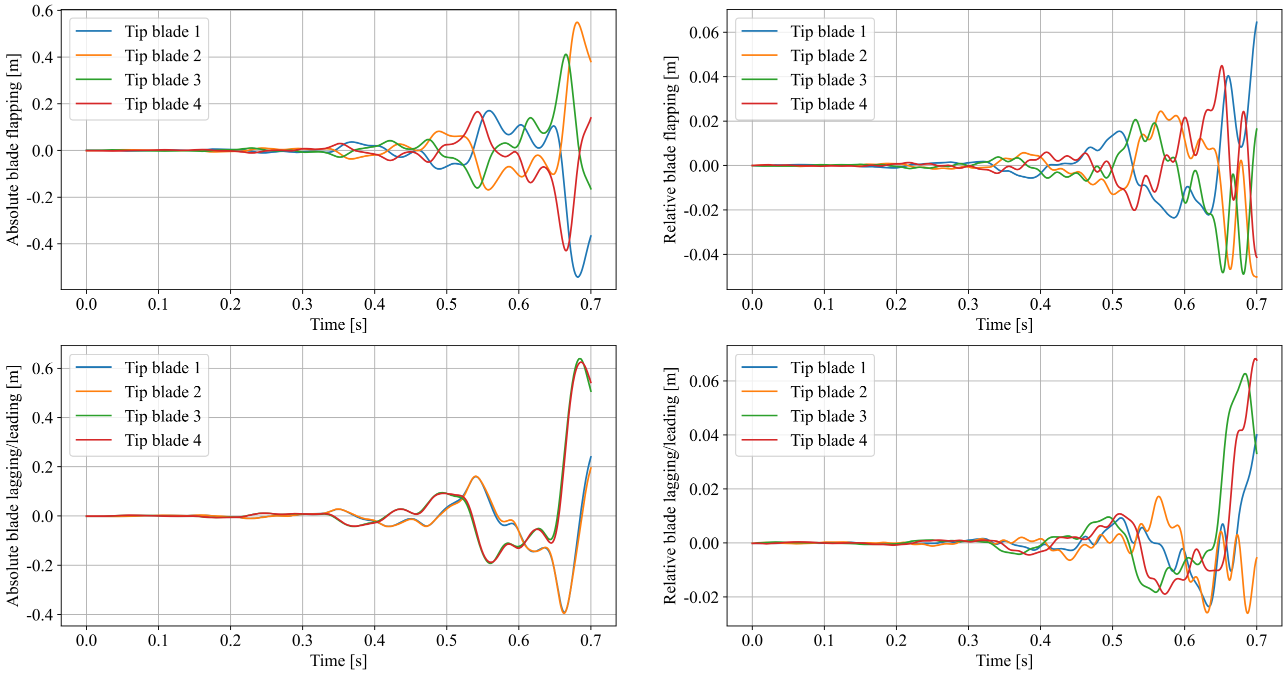

Figure 4.23: Absolute and relative lagging/leading and flapping motion of the blade for the $\Omega = 100$ Rad/s instability. 2 elements per beam were considered

4.7.2.4 Fourth instability

The fourth and last instability of the propeller structure is a *backward whirl*, as depicted in Fig 4.24 where a very clear and rapidly growing precession motion of the propeller can be seen. Inspection of Fig 4.25 reveals that it results from the coalescence of 2 modes, hence the fact that it's nature fairly close to that of the first instability encountered. Also, 4.26 shows that the rotor admits some non-negligible vibrations of the blades with up to the 15% of blade flapping being due to the blade vibrations.

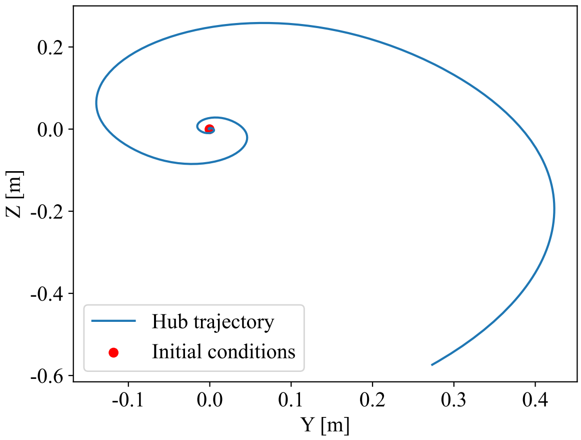

Figure 4.24: Hub trajectory within the third instability for $\Omega = 120$ Rad/s

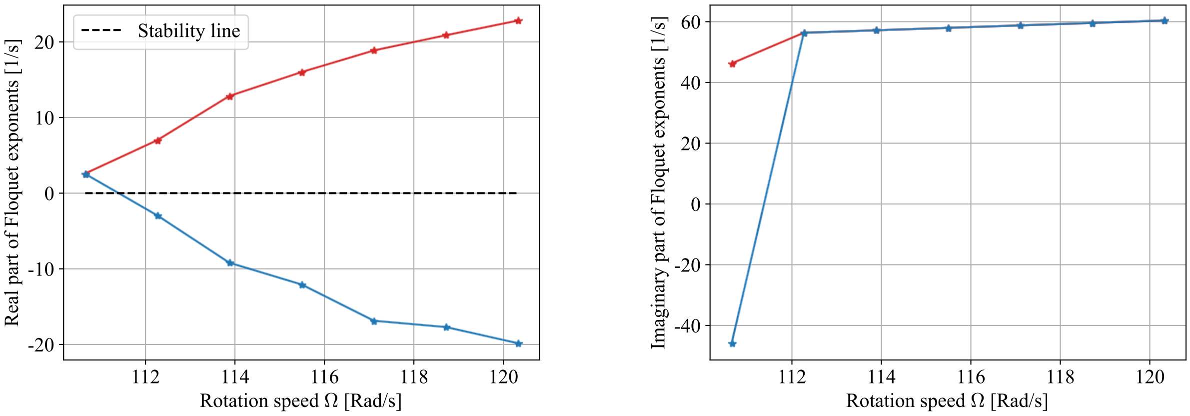

(a) Real part

(b) Imaginary part

Figure 4.25: Absolute and imaginary value of the Floquet multipliers. Only modes of interest were included on the Figure. 2 elements per beam were considered. Computation were conducted on *NIC5* from *CÉCI*

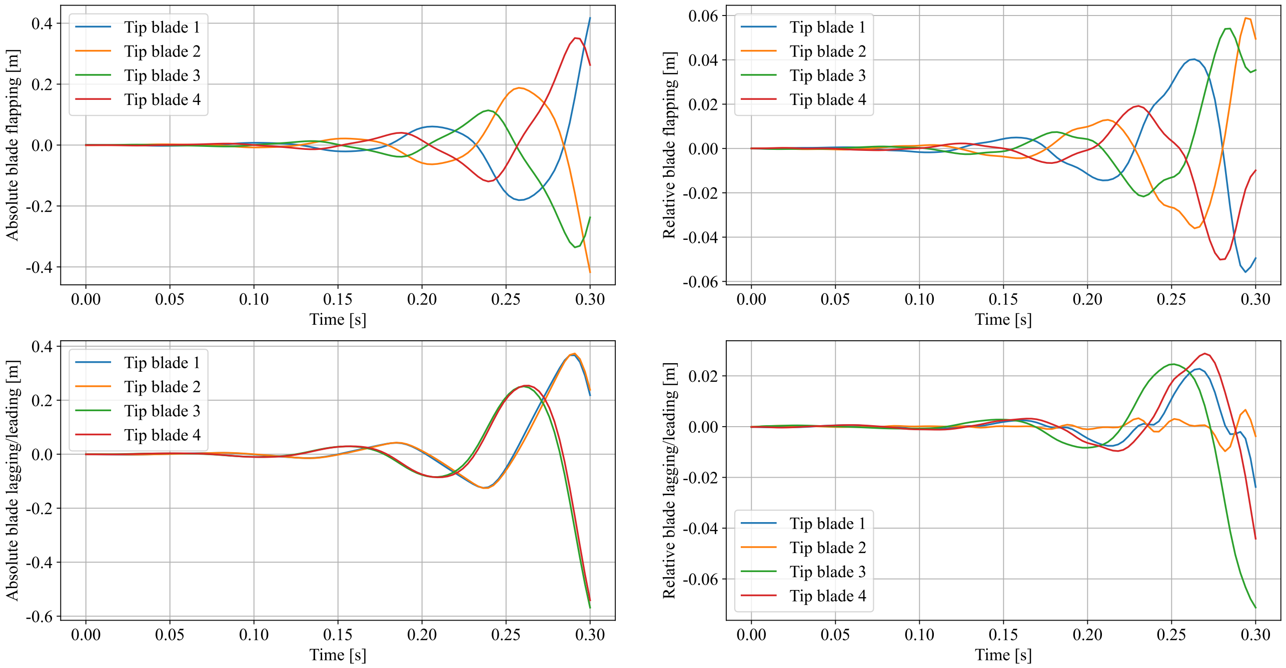

Figure 4.26: Absolute and relative lagging/leading and flapping motion of the blade for the $\Omega = 120$ Rad/s instability. 2 elements per beam were considered

4.7.2.5 Small conclusion

Review of all of the 4 instabilities of the structure revealed many interesting aspects.

First, some instabilities are clear *whirl flutter* instabilities and are, in this case, characterized by a coalescence of 2 Floquet modes. This is the case for the first and fourth instabilities. Then, it appears that some instabilities can be caused by a coalescence of 2 Floquet modes but at a zero frequency, resulting in a *divergence*. This is the case for the second instability. Also, the third instability proved to be of a different nature than the others since it doesn't not seem to rely on the coalescence of modes.

Finally, for the 2 first instabilities including the blade dynamics showed irrelevant as the rotor essentially acts as a rigid disk. For the third and fourth instabilities however, taking into account blade vibrations showed to be relevant, especially for flapping, as up to 15% of blade motion was related to them vibrating.

4.8 Stability with flexible wing

As discussed in the introductory sections of this thesis, wing flexibility as a large impact on the stability of the overall wing-propeller configuration, as simple model such as the 4 degree of freedom model where only the bending and torsion of the wing were taken into account already illustrates it (Section 1.5.1.4).

Moreover, previous work where the wing was modeled a finite element structure and the propeller was a simple 2 degree of freedom (Bohnisch, Nils *et al.* (2022 [5])) showed that even though most instabilities occur due to either a forward or backward whirl mode becoming instable there also exist configurations where a wing mode becomes unstable. Such observations, and perhaps others as the model developed in this thesis is richer with a fully finite element modeled propeller and wing, are to be expected.

At this end a flexible wing will be introduced in the model, as depicted in the reference model of the 4-bladed propeller from section 4.2.1. It is expected that the mass as well as the stiffness of the wing will play a great role in this analysis. Wing flexibility can essentially be investigated using it's bending stiffness EI. This means that the young modulus E of the wing material and/or the wing inertia can be modified. However, changing the wing inertia will also change it's mass making results difficult to interpret. To counter this the first parameter to be tweaked will be E as it enables to play on wing flexibility without changing it's mass and will therefore simplify discussions as a first step. After, the blade section will be tweaked as well.

Finally, in this section all of the computations will be done with 2 elements per beam, based on the results that were obtained previously.

4.8.1 Influence of wing stiffness

In this section different values of wing young modulus E_w will be reviewed without changing geometry of the wing from the reference configuration any other parameters of the problem. Results are given in Fig 4.27.

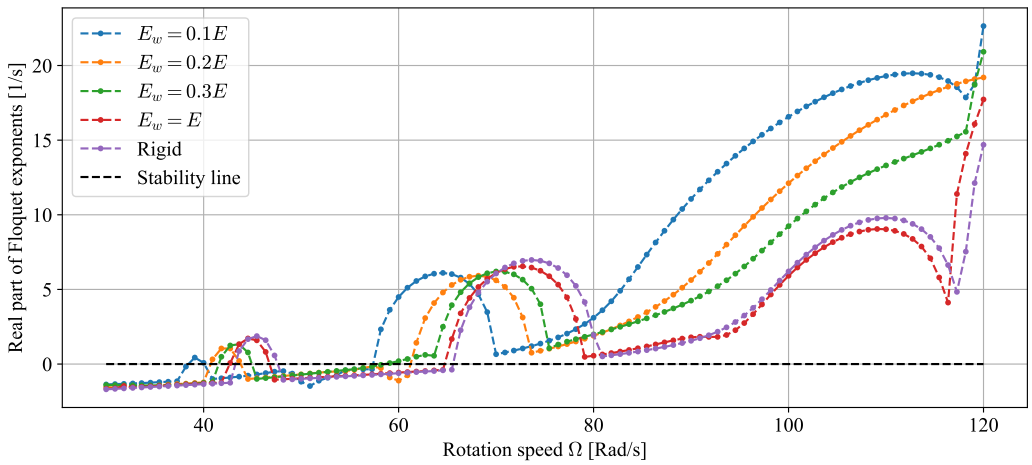

Figure 4.27: Largest real part of the Floquet exponents for different rotation speeds. Two element per beam were considered. Used configuration is the one depicted in section 4.2.1 but with different amount of wing young modulus values E_w with E being the modulus of steel. Computations were done in *NIC5* from *CÉCI*.

First, as expected, the stability behavior converges to the rigid wing configuration as the wing stiffness becomes larger.

Then, it's observed that, as the wing is made more and more flexible instabilities tends to be shifted at lower rotation speeds. This effect is barely noticeable for quite sturdy wing configurations (in this case all of the cases where $E_w \geq 0.5E$) where including the wing in the system dynamics has a very small impact on it's stability. For more flexible configurations this effect grows very fast in intensity rapidly pushing the instability regions towards lower Ω values. This effect is especially visible for the second and third instability.

Also, the amplitude of the instabilities tends to not change much when the wing with a few exceptions. The first one would be that for sturdy wing configurations ($E_w \geq 0.5E$ in this case), a slight amplitude reduction is noted. The second finally would be the third instability whose amplitude greatly changes when more flexible wing configurations are considered.

These observations seems to indicate that if the wing is quite sturdy then it tends to have a very small but positive impact on the stability. This effect can be explained by the wing providing an extra amount of structural damping. In that case considering a rigid wing provides a *conservative* solution of the stability prediction. That being said, if more flexible wings are considered then the stability can be extremely negatively impacted with the Ω range of operation of the structure being severely limited. This effect is expected to come from the flexible wing that provides an extra arm lever to the system, thereby amplifying hub displacements and allowing instability to occur earlier. In other words, if the wing becomes more flexible it's as if the pylon had become more flexible since it's displacements are added to those provided at the tip of the wing. In such a configuration if one were to use a rigid wing model it would yield to an *over-optimistic* stability prediction.

Additional information can be acquired from Fig 4.28. It's seen that depending on the instability the energy can be essentially concentrated in the rotor or be exchanged with the wing or in other words the wing can or not be an important part of the dynamics. For the first instability, even for a very flexible wing, barely any energy exchange is seen, explaining why this instability doesn't change a lot with E_w. As for the second instability more exchanges can be observed, translating richer structure dynamic where the wing plays a role, thereby making this instability susceptible to changes of E_w. Finally, the last instability at $\Omega = 110$ Rad/s very large amounts of energy are exchanged, allowing the wing to undergo large displacement and thereby providing an arm lever and thus extra motion to the propeller causing the amplitude of the instability to grow a lot when E_w decreases.

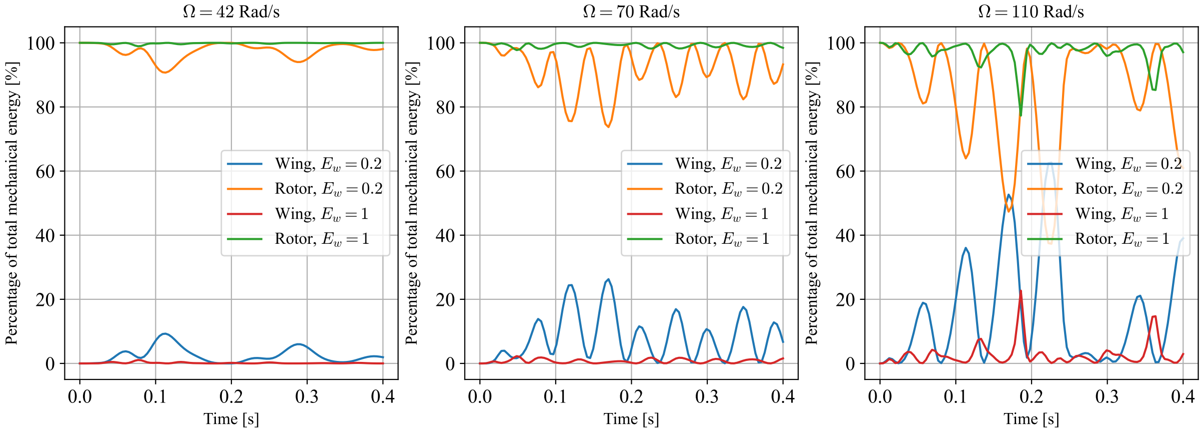

Figure 4.28: Repartition of the total mechanical energy between the rotor and the wing for 3 different instabilities. Different wing modulus E_w were considered with E being that of steel. Only energy from deformations was taken into account ($i.e$ for the rotor rotation energy due Ω wasn't accounted for).

4.9 Stability diagrams

Now that the different types of instabilities as well as the influence of a flexible wing have been investigated it is of interest to study how the stability of the problem is influenced by the geometry of the pylon. At this aim the *stability diagrams* of the 4-bladed propeller will be considered. Such diagrams have already been displayed for the 2 degrees of freedom analytical whirl flutter model in section 1.5.1.1 where the stability of the model was assessed as a function of the shaft stiffness in yaw and pitch directions. This approach is translated in the context of finite elements by considering the first bending frequency of the shaft in pitch and yaw directions.

4.9.1 Influence of pylon stiffness

To understand the stability diagrams of the following sections is it before necessary to investigate what the effect of changing the size of the rectangular pylon beam has on the system. This is done in Fig. 4.29 where one dimension of the pylon beam is modified while the other is fixed, effectively decreasing it's stiffness in a favored direction.

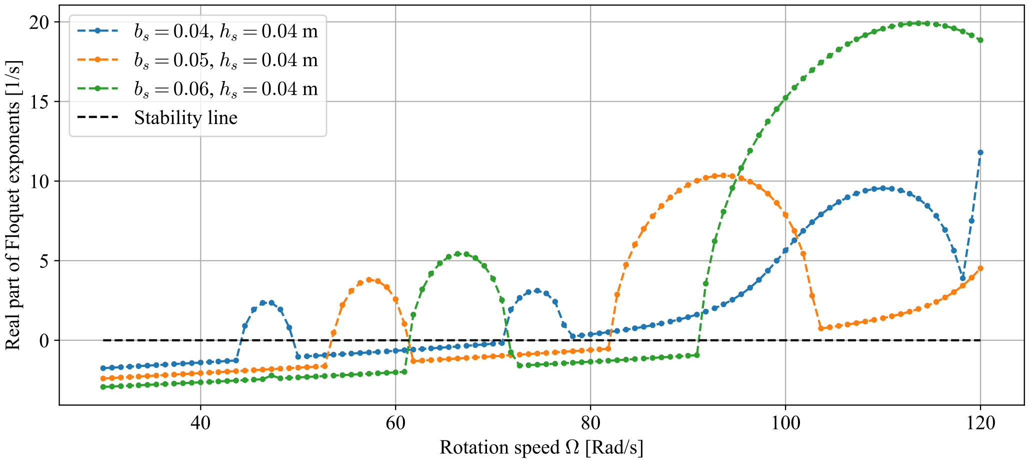

Figure 4.29: Largest real part of the Floquet exponents for different rotation speeds. Two element per beam were considered. Used configuration is the one depicted in section 4.2.1 but with different pylon beam sections b_s, h_s were considered. Computations were done in *NIC5* from *CÉCI*.

Figure 4.29 shows that, as the pylon stiffness decreases, a very comparable pattern of instabilities is observed but shifted towards lower rotation speeds. This is explained physically by the fact that a less rigid pylon tends to amplify the structure displacements more, enabling it to reach instability at lower rotation speeds.

These results show that the exact same instability pattern is always observed in this case being:

stable - first instability (whirl flutter) - stable - second instability (divergence) - unstable.

This pattern is simply shifted towards lower rotation speeds when the pylon stiffness is reduced. This makes it such that, at least from a qualitative point of view, increasing the pylon stiffness has a comparable effect to a decrease of the rotation speed. This means that for a fixed rotation speed and a growing stiffness of the pylon the same stability pattern should be observed. This effect is more easily illustrated with a numerical example based on Fig. 4.29. Let $\Omega = 70$ Rad/s initially with b_s starting from 0.04 m all the way to 0.06 m ($h_s = 0.04$ m is fixed). The system would initially be barely stable (as a stable configuration is found at $\Omega = 60$ Rad/s and $b_s = 0.04$ m). However, when stiffness is increased by considering $b_s = 0.05$ m then the system is unstable. Finally, for $b_s = 0.06$ m stability is retrieved.

When doing a stability diagram, the stability of the system is assessed for different values of ω_y and ω_z are the first bending frequencies of the equivalent clamped-free pylon beam. Doing such is equivalent of redoing Fig 4.29 but with different values of h_s. It means that one should not be surprised to find the same stability pattern as the one depicted in Fig 4.29 (but reversed since an increase in b_s is qualitatively equivalent to a reduction in Ω). Fig 4.30 confirms these expectations and clearly show the same stability pattern as described previously. Few interesting aspects can be discussed from 4.30.

First, it appears that the structure can only operate in 2 different stable regions. Recalling the knowledge acquired in section 4.7.2, where the nature of the instabilities was investigated, it can be said that the structure can only be operated either *before* the first whirl instability (upper left of the figure) or *between* the first whirl instability and the following divergence (middle of the figure). Typically it would be best to only consider the largest stable area as it's possible to take a larger security margin from the whirl instability. That being said, it would be theoretically possible, if one would want to reduce the stiffness of the pylon as much as possible, to operate between the 2 instable regions. This would however require extra precautions to make sure that there no significant exterior factor that could change the system dynamics such as wear of the materials or activation of an unsuspected non-linearity that would harden or soften the system and push it into whirl flutter or divergence respectively. Operating in this region would then be reserved for extreme applications where constraints on the pylon stiffness (due to it's weight for example) are an absolute priority, this would for example by the case of ultra-light urban air vehicles which is the causa finalis of this thesis.

Finally, the attentive reader would notice that the stability diagram is slightly asymmetric. This has no physical meaning as there is a priori no reasons to favor one direction rather than another. This effect is likely a numerical artifact due to the fact that the structural matrices $\boldsymbol{M}$ and $\boldsymbol{K}$ are developed using the formulas from Géradin (1994, [9]) where the section is assumed to be circular thereby with no precautions to be taken in regards to symmetry, while rectangular sections were used in this thesis. Despite this, this effect is rather small only seem to affect the width of the instability due to first whirl flutter instability for larger values of ω_z and would therefore not change the results by much.

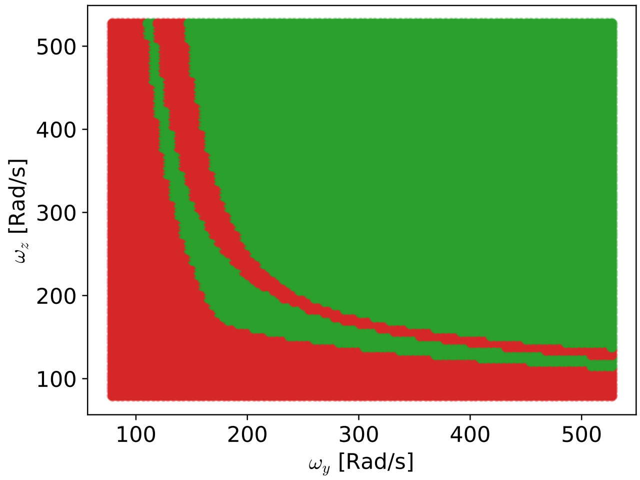

Figure 4.30: Stability diagram giving the stable and unstable configurations for the 4-bladed propeller from section 4.2.1 with a rigid wing and different pylon beam sections. ω_y and ω_z are the first bending frequencies of the equivalent clamped-free pylon beam. Computations were done with 1 elements per beam and took ≈ 8 hours for 10000 points.

4.9.2 Influence of a flexible wing

A wing will now be considered into the 4-bladed propeller model. The flexible wing is expected to introduces asymmetry due to the very nature of the geometry of the structure. Indeed, the pylon bends in the XY and ZX plane but the wing essentially only bends in the ZY plane thereby amplifying the XZ motion of the propeller and not the XY one. In other words, the system should be more prone to instability in the XZ plane corresponding to the ω_z frequency when a wing is included. Stability diagrams of multiple wing configurations are given for comparison in Fig 4.31.

First, addition of a wing tends to sustain the lower left unstable region to stiffer pylon configurations. These results can be understood from the previous discussions. In section 4.8.1 it was observed that when considering a more flexible wing, all the instabilities tended to be shifted to lower rotation speeds. In section 4.9.1 it was assessed that, qualitatively, an increase of pylon stiffness has a comparable effect as a decrease in rotation speed. In other words, the decrease in the unstable rotation speeds must be compensated by an increase in pylon stiffness to get an equivalent stiffness configuration as with the rigid wing thereby shifting the unstable regions of the stability diagrams to stiffer pylon setups.

Then, when the wing becomes more and more flexible it appears that the second unstable region, associated to the first whirl flutter instability, is essentially shifted to stiffer pylon configuration just like the first unstable region. This remains true until an extremely flexible wing ($E_w = 0.1E$) is considered. In this exotic case the second unstable region greatly reduces in size and doesn't split the 2 stable regions anymore. These results are once again explained using section 4.8.1 where it was observed that, as E_w decreases, the first instability is shifted towards lower Ω values, hence the unstable region shifted to stiffer configurations, but also that it's amplitude decreases until for the $E_w = 0.1E$ configuration the instability barely exists anymore. Improvements on the stability are noticeably better along the ω_y as the effect of the wing is asymmetric and favors instability for the ω_z axis as discussed at the beginning of this section.

Finally, a very small stable region is found for $E_w = 0.2E$ on the lower left of the diagram. This instability is likely due to the fact that right after the second instability peak, the system remain unstable but barely such that there could exist pylon configurations were a small stable bandwidth of Ω right after the second instability could exist.

As a conclusion, not applying a coupling disregards parts of the system dynamics and neglect a possible region of instability.

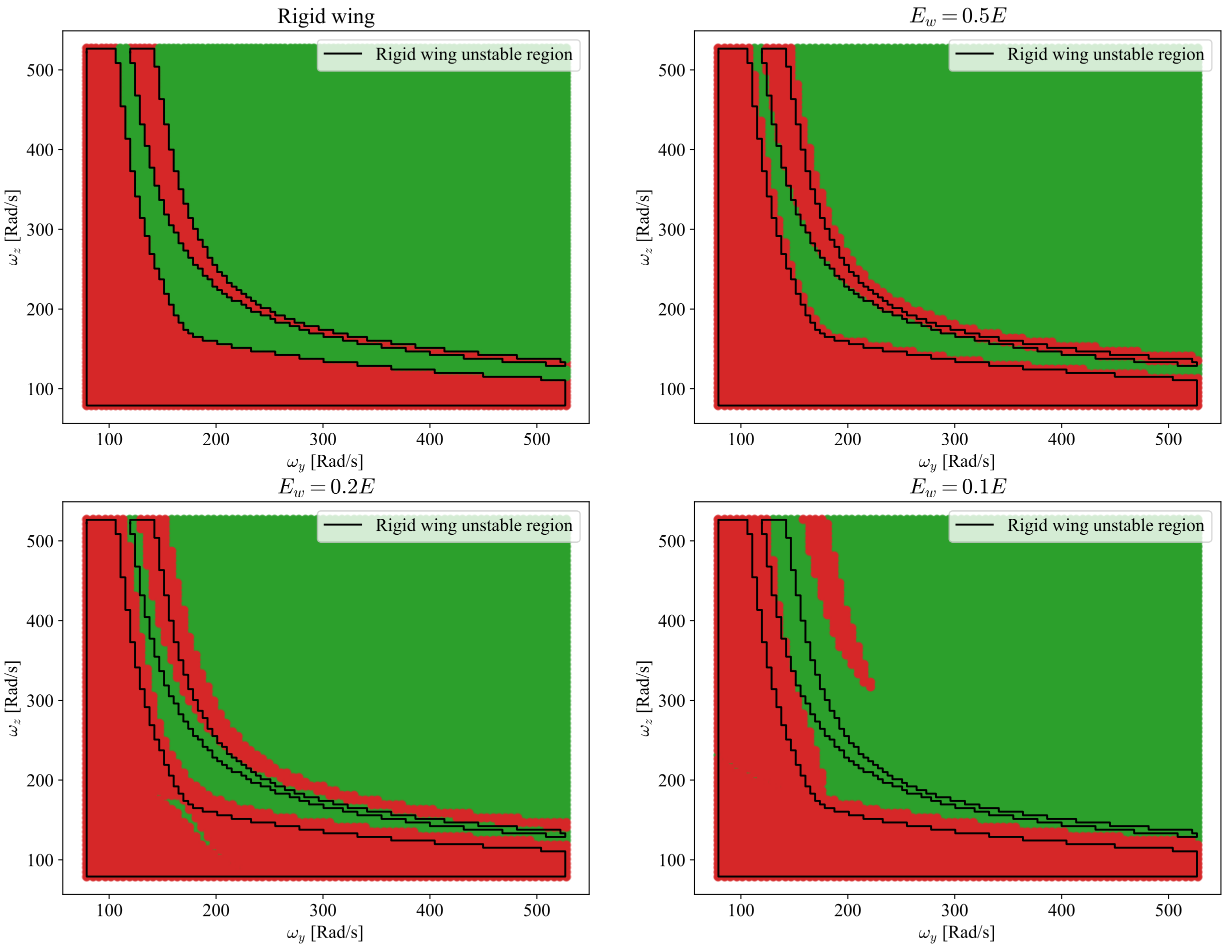

Figure 4.31: Stability diagram of the 4-bladed propeller configuration including a wing of different young modulus values E_w, E being the modulus of the steel. The results for the rigid wing configuration are recalled and compared with those with a flexible one. Stable and unstable configurations are given for different pylon sections. ω_y and ω_z are the first bending frequencies of the equivalent clamped-free pylon beam.

4.9.3 Influence of coupling

To finish this chapter it is of interest to compare the stability diagrams of the structure with or without applying the coupling procedure. Results are shown in Fig. 4.32.

First, it appears that coupling the stator and rotor parts of the structure tends to change a bit the instability due to static divergence (on the lower left of each diagram). In the case of a rigid wing this causes the computations to *under-estimate* the extend of this instability and in the case of a very flexible it *over-estimates* it. This effect remains however small.

Then, the most important difference lies in the second unstable region that simply does not exist without coupling. It means that the first whirl flutter instability, predicted when applying the coupling procedure, isn't modeled with no coupling. Since it is not advised to operate the structure between the 2 unstable regions it means that in practice the stiffness requirements on the pylon as much structure in this case.

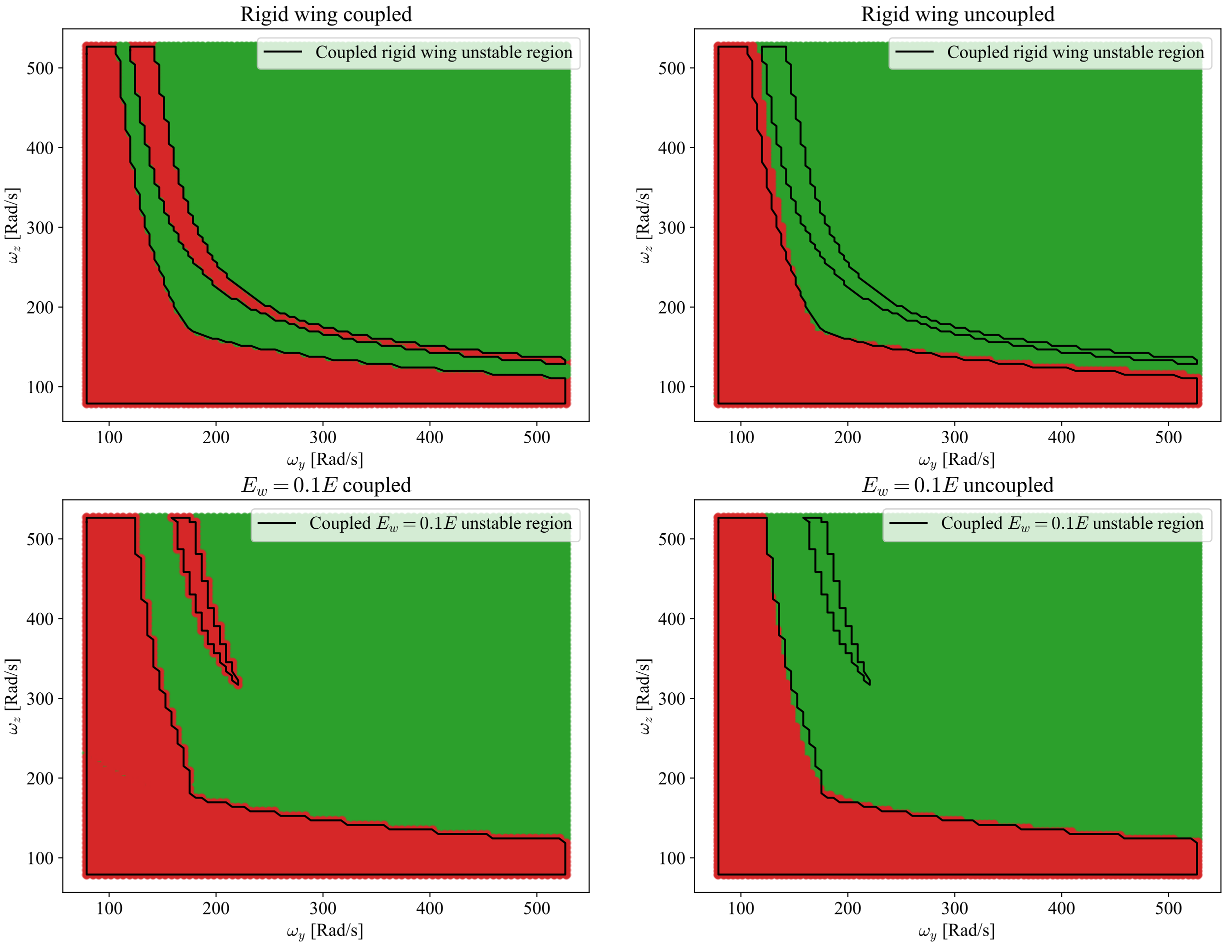

Figure 4.32: Stability diagram of the 4-bladed propeller configuration including a wing of different young modulus values E_w, E being the modulus of the steel. For each line, the black polygons are the unstable region of the figure on the left. Stable and unstable configurations are given for different pylon sections. ω_y and ω_z are the first bending frequencies of the equivalent clamped-free pylon beam.

Chapter 5

Final words

5.1 Conclusions

In this thesis the *FerBeam* python framework has been developed and proved it's capabilities to handle user-inputted beam structures with rotor and stator parts coupled together.

The rotor and stator parts of the problem were successfully modeled using Euler-Bernoulli 3D beam elements in their respective frames. Results where verified successfully using a the commercial software *Siemens NX* with the *Samcef* module for the stator part and the Campbell diagram of the *Rotordynamic* module for the rotor part.

The coupling procedure that had already been partially developed in previous works was rigorously and formally rewritten using a matrix coupling blocks formulation making it easier to replicate and understand for future works. Coupling could however only admit a partial validation with the results only corresponding qualitatively.

Stability was studied using the Floquet stability analysis for periodic systems and due to its very nature required the optimization of the time integration procedures to be tackled. Numerical stiffness resulting from the coupling procedure was demonstrated and led to the choice of the *BDF* integration schemes. Computation time was also reduced by considering a pre-computed tensorial form of the coupled equations of motion such that only interpolations were required at each time step. Finally, the problem was parallelized and executed on a super-computer greatly allowing to reduce computation time.

Those optimizations allowed to assess stability of a simple academic example of a 4-bladed wing-propeller configuration for a large number of parameter values. In particular the stability as a function of the rotation speed showed that the structure first undergoes *whirl-flutter*, briefly retrieves stability and then encounters *divergence* after which stability cannot be retrieved. This first whirl flutter instability as been proved to only appear when coupling is applied and thereby shows the necessity of coupling. While the first instability only makes the rotor acts like a rigid disk, for the following instabilities at higher rotation speeds up to 15% of motion came from flapping vibrations of the blades showing the necessity to take blade dynamics into account. Stability when including a flexible wing was also considered and showed that, while the wing can have a slightly positive impact on stability for sturdy configurations by providing additional structural damping, it often tends to deteriorate stability for flexible configurations, especially for instabilities where large amounts of energy exchanges between the rotor and the wing were observed. These results were also discussed using the stability diagrams that confirmed these observations through the presence of 2 unstable region, the first corresponding to whirl-flutter and the last to divergence.

5.2 Limitations

While convergence of the model as been studied, it proved to be extremely difficult to consider more than 3 beam elements per beam as otherwise computing would not converge resulting in overflow of the integrator. Therefore, some of the results cannot be considered to be totally converged.

Then, this thesis only considers 1D elements meaning that some torsion or higher order modes cannot be taken into account. Choice of a 2D or even 3D mesh would of course be desirable but would lead to a large increase in the number of degrees of freedom and thereby in unmanageable computation times. These issues could, perhaps, be solved with an in-house implementation in a compiled and efficient language of a stiff integration procedure that can handle a matrix of initial condition in an efficient manner. This couldn't be done in this thesis due to time constraints.

Also, comparison between the result in this thesis have proved to be very difficult to conduct. Reasons are first that not many analytical or commercial FE software's could be used to output results comparable to the coupling done in this thesis. The coupling procedure thereby could only be qualitatively and not quantitatively verified using the an analytical model of ground-resonance. Reasons are that linking the analytical and FE model required exotic values of material parameters that made it impossible for the solver to converge. A better approach to verify the coupling would likely be to use the *Coleman transformation* from *Rotordynamics* module but this couldn't be done in time.

This thesis doesn't take into account aerodynamical effects which are expected to have a non-negligible effect on the stability, likely with a stabilizing effect such that the only instabilities that could occur were due to gyroscopic effects (whirl flutter) or due to centrifugal stiffness softening (divergence). An important part of the dynamics was thereby disregarded.

Multi-propeller configurations that are the main preoccupation of urban air travel and that should be the causa finalis of the thesis couldn't be tackled in time. Their implementation into the framework have nevertheless be done.

Formulas of the structural matrices $\boldsymbol{M}$ and $\boldsymbol{K}$ used in this thesis come from Géradin expects circular beams while rectangular beams were used. This made the choice of a third point to construct the basis of the element frame ambiguous and the results showed a slight dependence to this choice. This effect was attributed responsibility for the slightly asymmetric shape of the stability diagrams that couldn't be explained otherwise.

Validation of the rotor parts of the equations of motion was conducted using a Campbell diagram and it appeared that while an almost perfect fit was found for almost all the modes between Python and *Rotordynamics* from *NX* there remained one mode from *NX* that the Python framework couldn't capture at all. Reasons of the discrepancy are still unknown especially as the missed mode from *NX* had nothing particular in shape of form.

Finally, the 4-bladed wing-propeller is extremely simplistic and doesn't represent reality accurately. In particular it lacks additional engine mountings and dampers that typically isolate the rotor and stator parts from each other and should therefore greatly improve stability. This is especially the case of the first instability encountered by the model which is a whirl flutter, this instability isn't of a large amplitude and would likely disappear completely if engine dampers were to be considered only leaving the system with one unstable region in the stability diagrams instead of two.

5.3 Further work

During this thesis multiple ideas were suggested but couldn't be implemented due to time constraints. Here are a non-exhaustive lists of what could be done to improve the model.

First, as discussed above, an in-house implementation of a stiff time numerical scheme that can efficiently handled a matrix of initial conditions would likely greatly improve the computation time. This algorithm would probably have to be written from scratch as, in my knowledge, no such libraries exist. Moreover, it has been observed that, in some cases, the computation time is I/O bounded due to having to call the python interpreter at each time-step. This could be avoided by either using a compiled language such as C++, Fortran or even Julia. If one still want to profit from the convenience of using Python it would still be possible to just implement the integration algorithm in these efficient languages and use a wrapper to call it directly from Python.

Then, using the reduction method suited for dynamic systems such as *Craig-Bampton* could allow to reduce the hub and blades as just on super element that captures must of the physics and could potentially greatly sped up the computations as well. This is very probably a necessary step to be able to module the structure using 2D or even 3D elements while keeping the computation time acceptable.

Also, implementation of the aerodynamical effects needs to be done. These effects could be added via an implementation of the blade-element theory using a mesh that is separate from the mechanical mesh as the convergence requirement are vastly different. Moreover, due to the extremely dynamic nature of the problem the unsteadiness shall be taken into account for example using Theodorsen's theory.

Furthermore, it would be of interest of developing adimensional numbers that could capture the physics of the problem. Doing such as would allow first, to be able to compare the performance of different design together with a much greater level of abstraction and also to be able to develop reduced models for wind tunnel testing. One last benefit from adimensional number would be to work on an equivalent rotating machine but whose instabilities of interest are at a larger rotation speed allowing to do the computations faster.

In addition, *FerBeam* should theoretically be able to handle mistuning of the blades by simply considering an anisotropic rotor. The resulting unbalance force should directly percolate from the computations of the centrifugal force and could yield to very interesting results with very few modifications to do in the code.

Moreover, the uncoupled part of the framework was developed in all generalities, meaning that it should be able to handle different beam structures than propellers. One interesting configuration would for example to consider a simplified drone or helicopter structure. As for the coupled part of the framework it unfortunately assumes that the rotation speed vector is of the form $\mathbf{\Omega} = [0, 0, \Omega]$ due to the very way the coupling equations were developed in the reference book. It would be possible and likely very interesting to adapt the formulation of the book to make it more general and extend the application of *FerBeam* to other types of rotating structures.

Finally, as discussed in the limitations section a complete verification of the coupling procedure is necessary to continue development of the subject. One way to do it could be to use the *Coleman's transformation* from *Rotordynamics* and compare the results to the FE model from *FerBeam*.

5.4 Statement on AI use

AI was used with parsimony and only to complete mundane and unimportant tasks, such as filling a latex table with given values or translate hand-written equations into latex, and in no way replaced critical thinking.

Appendix A

3D *Euler-Bernouilli* beam elements

Element Stiffness Matrix

$$\mathbf{K}_{eL} = \begin{bmatrix} \frac{EA}{\ell} & & & & & & & & & & & \\ 0 & \frac{12EI_z}{\ell^3} & & & & & & & & & & \\ 0 & 0 & \frac{12EI_y}{\ell^3} & & & & & & & & & \\ 0 & 0 & 0 & \frac{GJ_x}{\ell} & & & & & \text{Sym.} & & & \\ 0 & 0 & -\frac{6EI_y}{\ell^2} & 0 & \frac{4EI_y}{\ell} & & & & & & & \\ 0 & \frac{6EI_z}{\ell^2} & 0 & 0 & 0 & \frac{4EI_z}{\ell} & & & & & & \\ -\frac{EA}{\ell} & 0 & 0 & 0 & 0 & 0 & \frac{EA}{\ell} & & & & & \\ 0 & -\frac{12EI_z}{\ell^3} & 0 & 0 & 0 & -\frac{6EI_z}{\ell^2} & 0 & \frac{12EI_z}{\ell^3} & & & & \\ 0 & 0 & -\frac{12EI_y}{\ell^3} & 0 & \frac{6EI_y}{\ell^2} & 0 & 0 & 0 & \frac{12EI_y}{\ell^3} & & & \\ 0 & 0 & 0 & -\frac{GJ_x}{\ell} & 0 & 0 & 0 & 0 & 0 & \frac{GJ_x}{\ell} & & \\ 0 & 0 & -\frac{6EI_y}{\ell^2} & 0 & \frac{2EI_y}{\ell} & 0 & 0 & 0 & \frac{6EI_y}{\ell^2} & 0 & \frac{4EI_y}{\ell} & \\ 0 & \frac{6EI_z}{\ell^2} & 0 & 0 & 0 & \frac{2EI_z}{\ell} & 0 & -\frac{6EI_z}{\ell^2} & 0 & 0 & 0 & \frac{4EI_z}{\ell} \end{bmatrix} \tag{A.1}$$

Element Mass Matrix

$$\mathbf{M}_{eL} = m\ell \cdot \begin{bmatrix} \frac{1}{3} & & & & & & & & & & & \\ 0 & \frac{13}{35} & & & & & & & & & & \\ 0 & 0 & \frac{13}{35} & & & & & & & & & \\ 0 & 0 & 0 & \frac{r^2}{3} & & & & & \text{Sym.} & & & \\ 0 & 0 & -\frac{11\ell}{210} & 0 & \frac{\ell^2}{105} & & & & & & & \\ 0 & \frac{11\ell}{210} & 0 & 0 & 0 & \frac{\ell^2}{105} & & & & & & \\ \frac{1}{6} & 0 & 0 & 0 & 0 & 0 & \frac{1}{3} & & & & & \\ 0 & \frac{9}{70} & 0 & 0 & 0 & -\frac{13\ell}{420} & 0 & \frac{13}{35} & & & & \\ 0 & 0 & \frac{9}{70} & 0 & \frac{13\ell}{420} & 0 & 0 & 0 & \frac{13}{35} & & & \\ 0 & 0 & 0 & \frac{r^2}{6} & 0 & 0 & 0 & 0 & 0 & \frac{r^2}{3} & & \\ 0 & 0 & \frac{13\ell}{420} & 0 & -\frac{\ell^2}{140} & 0 & 0 & 0 & -\frac{11\ell}{210} & 0 & \frac{\ell^2}{105} & \\ 0 & -\frac{13\ell}{420} & 0 & 0 & 0 & -\frac{\ell^2}{140} & 0 & \frac{11\ell}{210} & 0 & 0 & 0 & \frac{\ell^2}{105} \end{bmatrix} \tag{A.2}$$

Interpolation matrix

Let the iso-parametric coordinates ξ, η, ζ on the beam element given by the following change of variable

$$\begin{aligned} \xi &= \frac{x}{l}, \\ \eta &= \frac{y}{l}, \\ \zeta &= \frac{z}{l}, \end{aligned} \tag{A.3}$$

l being the element length. Doing such allows to express the shape functions of the element defining the interpolation matrix

$$\boldsymbol{N} = \begin{bmatrix} 1-\xi & 0 & 0 \\ 6(\xi-\xi^2)\eta & 1-3\xi^2+2\xi^3 & 0 \\ 6(\xi-\xi^2)\zeta & 0 & 1-3\xi^2+2\xi^3 \\ 0 & -(1-\xi)l\zeta-(1-\xi)l\eta & \\ (1-4\xi+3\xi^2)l\zeta & 0 & (-\xi+2\xi^2-\xi^3)l \\ (1-4\xi+3\xi^2)l\eta & (\xi-2\xi^2+\xi^3)l & 0 \\ \xi & 0 & 0 \\ 6(-\xi+\xi^2)\eta & 3\xi^2-2\xi^3 & 0 \\ 6(-\xi+\xi^2)\zeta & 0 & 3\xi^2-2\xi^3 \\ 0 & -l\xi\zeta & -l\xi\eta \\ (-2\xi+3\xi^2)l\zeta & 0 & (\xi^2-\xi^3)l \\ (2\xi-3\xi^2)l\eta & (-\xi^2+\xi^3)l & 0 \end{bmatrix}^T . \tag{A.4}$$

Bibliography

[1] Cowper, g. r., 1966, the shear coefficient in timoshenko's beam theory, j. appl. mech., vol. 33, no.2, pp. 335–340.

[2] AAM International. Archer's midnight evtol to be displayed at global aerospace summit, 2023. Image used from this article, accessed June 5, 2025.

[3] Nils Böhnisch, Carsten Braun, Vincenzo Muscarello, and Pier Marzocca. About the wing and whirl flutter of a slender wing–propeller system. Journal of Aircraft, 61(4):1117–1130, 2024.

[4] John Boyd. Computing zeros on a real interval through chebyshev expansion and polynomial rootfinding. SIAM J. Numerical Analysis, 40:1666–1682, 12 2002.

[5] Nils Böhnisch, Carsten Braun, Stephan Koschel, and Pier Marzocca. Whirl flutter for distributed propulsion systems on a flexible wing. 01 2022.

[6] C. F. Curtiss and J. O. Hirschfelder. Integration of stiff equations*. Proceedings of the National Academy of Sciences, 38(3):235–243, 1952.

[7] B. Eckert. Analytical and a numerical ground resonance analysis of a conventionally articulated main rotor helicopter. Phd thesis, Stellenbosch University, 2007.

[8] Guido Fubini. Sugli integrali multipli. Rendiconti della Reale Accademia dei Lincei, Serie 5, 16(1):608–614, 1907. Reprinted in *Opere scelte*, vol. 2, Cremonese, 1958, pp. 243–249. See also JFM 38.0343.02.

[9] Michel Géradin and Daniel Jean Rixen. Mechanical vibrations: Theory and application to structural dynamics. 1994.

[10] Christopher Koch and Benedikt Koert. Influence of blade elasticity on propeller whirl flutter stability. 2023.

[11] A. Liapounoff. Problème général de la stabilité du mouvement. Annales de la Faculté des sciences de Toulouse : Mathématiques, 9:203–474, 1907.

[12] Vincent Masse. French army aviation eurocopter tiger, 2019. Consulted online the 23/05/23.

[13] Military Photo Report. 3ème rhc - régiment d'hélicoptères de combat, 2016. Consulted online the 23/05/2023.

[14] Donham, R. E., and Osterholt, D. J.,Utilizing Test Results to Show Adding Flexibility of Propeller Blades Is More Representative than the Classical Rigid Blade Propeller Whirl Flutter Analysis. 2007.

[15] EDF, Manuel de validitation de code Aster: Sslv104-poutre en rotation, 12/2011.

[16] Floquet, g. sur les équations différentielles linéaires à coefficients périodiques. annales scientifiques de l'École normale supérieure, série 2, tome 12 (1883), pp. 47-88. doi : 10.24033/asens.220. https://www.numdam.org/articles/10.24033/asens.220/.

[17] J. S. Przemieniecki, Theory of Matrix Structural Analysis, vol. 1. McGraw-Hill Book Compagny, 1968.

[18] Jacquet, C. (2024). Master thesis and internship[BR]- Master's thesis : Computational method for whirl-flutter analysis of urban air mobility vehicles[BR]- Internship. (Unpublished master's thesis). Université de Liège, Belgique. Retrieved from https://matheo.uliege.be/handle/2268.2/20851.

[19] R.Bennett and S. Bland, EXPERIMENTAL AND ANALYTICAL INVESTIGATION OF PROPELLER WHIRL FLUTTER OF A POWER PLANT ON A FLEXIBLE WING, 1964 NASA Technical Note. NASA-TN-D2399.

[20] Richardson , J.R.and Naylor , H.F.W. : Whirl Flutter of Propellers With Hinged Blades, Report No. 24 , Engineering Research Associates , Toronto, Canada , March 1962 .

[21] Wilmer H. Reed III, 1981 NASA Technical Memorandum. NASA-TM-83210 19820004168.

[22] Wilmer H. Reed III, REVIEW OF PROPELLER-ROTOR WHIRL FLUTTER, 1965 NASA Technical Report. NASA-TR-R264.

[23] Alireza Rezaeian. Helicopter ground resonace analysis using multibody dynamics. In Proceedings "ERF 2010", 2010.

[24] Ted Rose and Bill Rodden. Propeller.nacelle whirl flutter addition to msc/nastran. 03 1989.

[25] Wilson J. Rugh. Linear system theory (2nd ed.). Prentice-Hall, Inc., USA, 1996.

[26] Loïc Salles. Etude de l'usure par fretting sous chargements dynamiques dans les interfaces frottantes : application aux pieds d'aubes de turbomachines. Theses, Ecole Centrale de Lyon ; Université Technique d'Etat Bauman de Moscou, December 2010.

[27] L. Sanches. Résonance sol des hélicoptères : modélisation dynamique, analyse paramétrique de la robustesse et validation expérimentale. Phd thesis, Institut Supérieur de l'Aéronautique et de l'Espace, 2011.

[28] Leonardo Sanches, Guilhem Michon, Alain Berlioz, and Daniel Alazard. Instability zones for isotropic and anisotropic multibladed rotor configurations. Mechanism and Machine Theory, 46(8):1054–1065, 2011.

[29] Leonardo Sanches, Guilhem Michon, Alain Berlioz, and Daniel Alazard. stability analysis of ground resonance phenomenon in helicopters: experimental investigations. VII Congresso Nacional de Engenharia Mecânica, 2012.

[30] Lawrence F. Shampine and Charles William Gear. A user's view of solving stiff ordinary differential equations. Siam Review, 21:1–17, 1979.

[31] Lawrence F. Shampine and Mark W. Reichelt. The matlab ode suite. SIAM Journal on Scientific Computing, 18(1):1–22, 1997.

[32] C.E. Shannon. Communication in the presence of noise. Proceedings of the IRE, 37(1):10–21, jan 1949.

[33] E. S. TAYLOR and K. A. BROWNE. Vibration isolation of aircraft power plants. Journal of the Aeronautical Sciences, 6(2):43–49, 1938.

[34] Arne Vollan and Louis Komzsik. Computational Techniques of Rotor Dynamics with the Finite Element Method. 03 2012.

[35] Jiří Čečrdle. In Whirl Flutter of Turboprop Aircraft Structures. Woodhead Publishing, Oxford, 2015.